

DEVELOPING AND APPLYING METHODS TO SIMULATE
A CHARGE TRANSFER FROM A DYE TO A
SEMICONDUCTOR USING QUANTUM DYNAMICS

by

ALICE VAN HAEFTEN

A thesis submitted to
the University College London
for the examination of
DOCTOR OF PHILOSOPHY

Student Number: 17126852
Department of Chemistry
UCL
2021

I, Alice Van Haeften, confirm that the work presented in this thesis is my own. Where information has been derived from other sources, I confirm that this has been indicated in the thesis and a reference given.

December 20, 2021

Abstract

The main focus of this thesis was to use quantum dynamics techniques to probe the process of a charge transfer in a dye-semiconductor complex. The use of photovoltaic cells in solar electricity relies strongly on these types of charge transfer systems, and therefore an increased knowledge on this process can help to increase efficiency of these cells, and lead to better design of photovoltaic cells.

In order to achieve this goal, firstly, the charge transfer along the radically cationic state of allene was investigated, as a precursor to the more complicated dye-semiconductor system. The populations of the charge donor and acceptor states were analysed, and the photoelectron spectrum was calculated and compared to experimental data to verify the results. These computations were calculated using a vibronic coupling Hamiltonian coupled with the multi-configuration time-dependent Hartree (MCTDH) method, as well as with multilayer form (ML-MCTDH).

Following on from allene, a dye-semiconductor system was investigated, using a Coumarin-343-TiO₂ complex. The model used for this process was akin to a donor-acceptor system, comprising of the S₁ state of the dye molecule as the donor state, and the conduction band of the semiconductor as a continuum of acceptor states. In order to represent the conduction band of the semiconductor, the band was discretised and coupled to the donor state. The couplings between the donor and acceptor states were approached from two different angles, with varying results of success. Again, employing a vibronic Hamiltonian, the main vibrational modes of the dye were included in the dynamics. Using the multilayer multi-configurational time-dependent Hartree (ML-MCTDH) method, the wavepacket dynamics were analysed and the population of the donor state was investigated.

Whilst the calculations performed so far has been done at 0 Kelvin, this is not an accurate model of the charge transfer that occurs inside a solar cell. Solar

cells often have normal working temperatures of over 300 K. Therefore, the next step was to see if a new model can be employed which can study this quantum behaviour at temperatures >0 K. Using the molecule Salicylaldehyde as a smaller test model, a ground state proton transfer was probed at various temperatures. This was done using density matrices. Using the ML-MCTDH formalism of a density matrix is a previously unexplored method, the results of which are presented in this thesis. This new approach to studying the quantum behaviour of larger systems at temperatures above 0 K offers a promising avenue to investigating the dye-semiconductor system further.

Impact Statement

Quantum effects play an important role in many biological and technological systems. One area that this thesis focused on is their role in photovoltaic cells, specifically dye-sensitised solar cells. A key step in the conversion of solar energy to electrical energy in these type of cells is an electron transfer process occurring from a dye molecule into the conduction band of the semiconductor it is adsorbed to. Understanding the quantum dynamics of this process allows the development and production of more efficient and more commercially viable solar cells.

The current most commercially viable solar cells are silicon based, and have efficiencies of around 25%. However, they are expensive to manufacture, thus creating a block in the commercial process. These dye-sensitised solar cells offer a photovoltaic which is cheaper to manufacture, but the currently available dye-sensitised solar cells only reach around 12% efficiency. Theoretical studies have shown that the maximum efficiency is over 20%. Only by fully understanding the key process in the production of electricity of dye-sensitised solar cells can they be improved to reach their maximum efficiency, thus allowing them to become a more viable option.

This thesis looked at solving the time dependent Schrödinger equation to predict the quantum dynamics of this system. The method used was the Multi Layer Multi-Configuration Time Dependent Hartree method (ML-MCTDH). In order to accurately represent a dye attached to the surface of a semiconductor, multiple models were considered. Although the final model considered the system as a simple 1-dimensional chain, it is able to be easily extended to allow for both 2-dimensional slabs and a 3-dimensional bulk. This will allow a more realistic model representing a dye attached to a bulk semiconductor to be considered, including all the relevant coupling terms within the solid. The model can also be easily adapted to represent any dye molecule and any semiconductor, allowing this to be

a versatile method to study the quantum dynamics of many types of dye-sensitised solar cell systems.

In order to make the model a more realistic representation of a dye-sensitised solar cell, the ML-MCTDH method was also extended, to using density matrices combined with the MI-MCTDH. This novel approach allowed the prediction of quantum dynamic behaviour of systems which also include environmental effects. This could include solvent effects or temperature effects. Being able to predict quantum effects at temperatures above 0 Kelvin is not non-trivial, and this method allows a much more realistic solar cell environment to be simulated. Due to previous contrasting research into the effect on temperature on the efficiency of dye-sensitised solar cells, the ability to study the quantum behaviours of these systems at non-zero temperatures is essential.

The work presented in this thesis thus provides a foundation for future research into electron transfer processes at semi-conductor surfaces using realistic models combined with full quantum dynamics simulations.

Acknowledgements

As an opening statement, PhDs are not easy. The last few years have been filled with hard work, self-doubt and countless explanations to friends and family of what I'm trying to achieve, without fully understanding that myself! However, it has been one of the most rewarding experiences of my life. It has pushed me to the limits of my motivation, and of my resilience to continue pushing through when everything seems to be at a loss. It has given me the opportunity to open my mind to areas of research I had never considered before, and allowed me to visit some beautiful parts of the world I never would have otherwise visited, and with some fantastic people. In fact, without these fantastic people, I never would have achieved what I have achieved.

The Worth group have been a wall of support from start to finish, past and present members. Thank you to Marianna, Anegelo and Ceridwen, who helped me settle in the the PhD life at UCL, and helped get my computers set up and answered countless stupid questions with patience.

Thank you to all our Masters and summer students over the years - Ella, Karan, Antonios, Alex, Antonia, Kai and Esra.

A massive thank you to Georgia, Sandra and Thierry. Not only has your staggering intelligence helped me out in countless ways, but your friendship, support and dedication have been an incredible inspiration.

Thank you to the newer (although not so new now!) group members, that despite COVID-19's attempts to distance us, have still been incredibly helpful and a joy to get to know - Barry, Diptesh and Jaymee.

Of course, an absolutely massive thank you to Graham. I cannot imagine being able to accomplish any of what I have done without your complete dedication, guidance and support. Your willingness to go above and beyond to help me out

over the last few years has not gone unappreciated!

I would also like to thank my family and friends over the last few years - I know most of you only pretend to know what I do! - "*is it something with lasers?*" Nevertheless, this means your support and encouragement is even more appreciated. Especially to those of you who have had to sit through my practice presentations over the years, nodding along encouragingly! I'd also like to extend a special thank you to Quizteama - I hope you understand how important those Monday nights were to my sanity, if not my head the next day!

My final, and biggest, thanks is to Oliver. Without you, I wouldn't have even applied to do a PhD in the first place. Your absolute and unwavering faith in me, when I had none, pulled me through when I was struggling. You have shown me how resilient and strong I can be as a person, and how to take pride in myself and my achievements. These are lessons that I will keep with me and forever be thankful for.

Contents

List of Figures	i
List of Tables	x
Glossary	xiii
1 Introduction	1
2 Background and Theory	7
2.1 Introduction	7
2.2 The Schrödinger Equation	8
2.3 Density Matrices	10
2.4 The Born-Oppenheimer Approximation	12
2.5 Beyond the Born-Oppenheimer Approximation	16
2.6 Conical Intersections	19
2.6.1 Jahn-Teller Systems	21
2.7 Semiconductors and Solar Cells	23
2.7.1 Why are semiconductors important?	23
2.7.2 Solar Cells	24
2.7.3 How can the efficiency of solar cells be improved?	26
3 Methodology	28
3.1 Introduction	28

3.2	Electronic Structure	29
3.3	Molecular Orbital Theory	30
3.3.1	Hartree Fock Theory	31
3.3.2	Electron Propagator Theory	36
3.4	Density Functional Theory, DFT	37
3.5	Solving the time dependent Schrödinger equation for the nuclear wavefunction	40
3.5.1	Multi-configuration time dependent Hartree method	41
3.6	Density Matrices	47
3.6.1	Type I Density matrix, ρ -MCTDH(I)	48
3.6.2	Type II density matrix, ρ -MCTDH(II)	50
4	Allene	52
4.1	Introduction	52
4.2	Electronic Structure Calculations	56
4.2.1	Vibrational Mode Analysis	56
4.3	Calculating the Spectrum	63
4.3.1	The Theory	63
4.3.2	The Photoelectron Spectrum	66
4.3.3	The state populations	69
4.4	Summary	76
5	Coumarin-343 - TiO₂	77
5.1	Introduction	77
5.2	Electronic Structure	79
5.3	Geometry Optimisation	79
5.4	Normal Mode analysis	81
5.5	TiO ₂	84

5.6	Molecular Orbitals	86
5.7	Electron transfer	89
5.8	Dynamics I	89
5.8.1	The Hamiltonian	89
5.8.2	Initial Results	95
5.8.3	Further Investigations	99
5.9	Dynamics II	103
5.9.1	The Hamiltonian	103
5.9.2	Results	105
5.9.3	Adding vibronic coupling	108
5.9.4	The β' Parameter	112
5.9.5	Extending the Model	115
5.10	Summary	118
6	Salicylaldimine	120
6.1	Introduction	120
6.2	Salicylaldimine	121
6.3	Potential Surface	123
6.4	Proton transfer dynamics	127
6.5	2D salicylaldimine Results	130
6.6	4D salicylaldimine Results	134
6.7	8D and 13D salicylaldimine Results	138
6.8	Summary	142
7	Conclusions	143
A	Appendix	i
	Bibliography	iv

List of Figures

1.1	The doubly degenerate cationic ground state of Allene, showing a Jahn-Teller conical intersection at the Franck-Condon point.	3
1.2	(a) A Coumarin-343 dye molecule attached to the surface of TiO ₂ semiconductor and (b) the corresponding energy levels. V_g denotes the ground state of the dye molecule, V_{dd} the donor state, which corresponds to the excited state of the dye molecule, and V_{kk} denotes the acceptor states, which correspond to the discretised conduction band of the semiconductor. The process of the ground state wavepacket being excited into the donor state is also shown, which is the initial step of the electron transfer process [1].	5
1.3	Salicylaldehyde exhibits an intramolecular hydrogen transfer from the oxygen to the nitrogen.	6
2.1	An example of a conical intersection. This is a 'Mexican hat' potential surface showing the crossing point of the adiabatic doubly degenerate ground electronic state of the Allene cation along the ν_5 (torsion) and ν_{11} (C-C asymmetric stretch) modes	8
2.2	The same system shown in both the adiabatic picture (left) and the diabatic picture (right) These are the potential energy surfaces of the lowest three energy states of butatriene [20].	17
2.3	An example of several highlighted avoided crossings in a 4 adiabatic state system, adapted from reference [24].	20

2.4	An schematic of (a) a peaked conical intersection and (b) a sloped intersection [28].The excited wavepacket moves towards the conical intersection (red arrows) where in (a) the wavepacket passes through the intersection and continues on the lower energy level, and in (b) the momentum of the excited wavepacket causes the wavepacket to move to an area of energy higher than the intersection on the lower surface. This is the tunnelling, where the wavepacket moves to an area on the surface but does not have the energy to cross the energy barrier. The wavepacket then bifurcates in this example, as 2 possible pathways are available.	22
2.5	A schematic which shows the band structure of a metal, a semiconductor, and an insulator. One can see that with enough energy, the electrons in a semiconductor can be promoted into the conduction band and the material behaves as a metal.	24
2.6	The Shockley-Queisser limit for a solar cell at 298.15 K. The efficiencies for energy conversion of different types of semiconductor are shown. Homo- and hetero-junctions are shown as green circles and red squares respectively, with indirect and direct band gaps shown as unfilled and filled symbols respectively. The AM1.5G refers to the spectral irradiance, corresponding to sunlight on the earth's surface which has been scattered by the atmosphere. Taken from [40] . . .	25
2.7	A schematic showing the energy levels and charge transfer in a DSSC, with TiO ₂ as the semiconductor . Figure adapted from [45].	27
3.1	An example of a multi-layer tree structure	46

4.1	On the left: The PES of the diabatic ground state along normal mode 4. This curve was obtained from a Taylor expansion around the neutral ground state of allene, at $Q=0$. Mode 4 corresponds to the torsional mode of b_1 symmetry. This is the mode that drives the charge transfer along the molecule. On the right: The allene molecule showing the two most significant vibrational modes, ν_4 and ν_6 , of b_1 and b_2 symmetry. These correspond to the torsional mode and the asymmetric stretch, respectively.	53
4.2	The (3,4) active space of allene. It consists of the occupied degenerate HOMO π orbitals, and the unoccupied degenerate LUMO π^* orbitals.	57
4.3	A sketch of a PES along some normal mode, Q , to show how kappa values are calculated for each normal mode	59
4.4	The calculated adiabatic \tilde{X}^2E state along the dimensionless nuclear coordinate, Q , of (a) ν_1 , (b) ν_2 , (c) ν_3 , (d) ν_4 , (e) ν_5 , (f) ν_6 , and (g) ν_7 modes, calculated using EPT, and fitted using VCHam.	61
4.5	The calculated adiabatic \tilde{X}^2E state along the significant (a) ν_4 and (b) ν_6 modes, calculated using CASSCF, and fitted using VCHam.	62
4.6	The ML-tree used to construct the nuclear wavefunction for 15D allene. The first layer separates the vibrational degrees of freedom (DOF) from the electronic DOF. The number of SPFs used are shown, as well as showing the number of primitive basis sets used to represent the SPFs in the deepest layer, shown here in blue.	65
4.7	The \tilde{X}^2E band of the photoelectron spectrum of allene including 3 modes for a propagation run for 30 fs (red), 50 fs (green) and 100 fs (blue). The calculation was also run for 200 fs, but as it exactly overlays the 100 fs spectrum, it has not been included.	66

4.8	The autocorrelation function of the 3D propagation run for 100 fs) .	67
4.9	The \tilde{X}^2E band of the photoelectron spectrum of allene. The experimental spectrum [111] is plotted in black on each graph along with the results using (a) 3 modes (red plot). The vibrational frequencies of these modes are also shown in the inlay. (b) 7 modes (blue plot), and (c) the full 15 mode system (green plot). All calculated plots have been shifted to overlap the adiabatic peak to that in the experimental spectrum.	70
4.10	The \tilde{X}^2E band of the photoelectron spectrum of allene using the CASSCF parameters. The experimental spectrum [111] is plotted in black, with the calculated spectrum in red.	71
4.11	The diabatic \tilde{X}^2E state along ν_4	71
4.12	The diabatic state populations in the (a) 3D, (b) 7D, and (c) 15D system. The system begins the propagation in state 2.	73
4.13	The mode expectation values of (a) ν_6 , and (b) the ν_3 in state 2 of the 3D, 7D and 15D systems	74
4.14	The expectation value of the step function along the torsional ν_4 in the (a) 3D, (b) 7D, and (c) 15D system.	75
5.1	The top panel shows the optimised structure of Coumarin-343, in Geometry-1. Labelled below are the possible conformers of the -COOH group. For clarity, only the acid part of C-343 has been shown.	80
5.2	The optimised geometry of Coumarin-343 used in the following calculations. The molecule is effectively planar, except for the puckering around the nitrogen. Upon adsorption to the TiO ₂ surface, the hydrogen on the hydroxyl group detaches and bonds to a terminal oxygen in the semiconductor	81

5.3	The optimised geometry of deprotonated form of Coumarin-343. The molecule has not lost any planarity by losing a proton.	81
5.4	A schematic showing the reorganisation energy in a three state system along some normal mode, Q. In all three diagrams, the black state, ψ_g , represents the ground state, the blue state, ψ_d represents the donor state, and the red state, ψ_a , represents the acceptor state. (a) shows the donor reorganisation energy, λ_d . (b) shows the acceptor reorganisation energy, λ_a . (c) shows the reorganisation energy of the electron transfer process, λ_{ET}	83
5.5	A (101) surface of anatase TiO ₂	85
5.6	The optimised geometry of (a) (TiO ₂) ₈ (H ₂ O) ₁₄ cluster and (b) (TiO ₂) ₂ (H ₂ O) ₅ cluster with the deprotonated C-343 dye molecule attached	85
5.7	The optimised geometry of a (TiO ₂) ₈ (H ₂ O) ₁₄ cluster with the deprotonated C-343 dye molecule attached	86
5.8	(a) The HOMO of the isolated C-343 dye molecule (b) The LUMO of the isolated C-343 dye molecule	87
5.9	The donor orbital of the dye-semiconductor cluster	88
5.10	An illustration of the PES along some coordinate, Q, of the ground, donor and acceptor states, V_g , V_d and V_k respectively, adapted from [1].	90
5.11	A schematic showing how the 1D tight binding approach was applied to the dye-semiconductor system. Adapted from [136]. The on-site matrix elements alternate signs to depict either a titanium site ($+\epsilon$) or an oxygen site ($-\epsilon$).	92

5.12	The diabatic population of the donor state of the C343-TiO ₂ system, with increasing number of states in the acceptor continuum of (a) 101 states (b) 501 states (c) 1001 states (d) 1499 states. These dynamics were run using 5 SPFs for both ν_{83} and ν_{83} t in both the donor and acceptor state.	97
5.13	The diabatic population of the donor state of the C343-TiO ₂ system, including more vibrational modes into the dynamics of the calculation. (a) 2 modes, as repeated from figure 5.12, ν_{83} and ν_{85} (b) 6 modes, ν_7 , ν_{14} , ν_{21} , ν_{83} , ν_{85} and ν_{87} (c) 12 modes, as shown in table 5.4. This is comapred to the decay plot fom the literature [123]	98
5.14	The diabatic population of the donor state of the C343-TiO ₂ system, with (a) 1499 states and (b) 2499 states in the acceptor continuum. These dynamics were run using 8 SPFs for both ν_6 and ν_7 in both the donor and acceptor state.	100
5.15	The diabatic population of the donor state of the C343-TiO ₂ system, at various coupling strengths, with (a) $v_0 = 0.5$ eV (b) $v_0 = 0.3$ eV (c) $v_0 = 0.1$ eV and (d) $v_0 = 0.05$ eV. These dynamics were run using electronic dynamics only, with 500 states in the continuum. .	102
5.16	A schematic of the dye-semiconductor system, showing the parameters of the new dynamics method.	104
5.17	The diagonalised acceptor sub-matrix derives the eigenvalues. There are 100 states in the continuum included here.	105
5.18	A schematic showing how the model used can be easily expanded to an (a) 2D and (b) 3D model.	106
5.19	The diabatic population of the donor state of the C343-TiO ₂ system, testing the effect of changing the β' parameter, where $\beta' =$ (a) 1 eV, (b) 0.5 eV, (c) 0.2 eV, (d) 0.15 eV, (e) 0.1 eV and (f) 0.05 eV. .	107

5.20	The diabatic population of the donor state of the C343-TiO ₂ system, testing the effect of changing the number of states included in the acceptor continuum - showing 100, 500 and 1000.	109
5.21	The ML-Tree diagram for 4D system, with the node number shown in the circles. The number of basis functions is shown in black, and the number of DVR grid points per DOF is shown in blue.	110
5.22	The ML-Tree diagram for 9D system, with the node number shown in the circles. The number of SPF basis functions is shown in black, and the number of DVR grid points per DOF is shown in blue. . . .	110
5.23	The ML-Tree diagram for 17D system, with the node number shown in the circles. The number of basis functions is shown in black, and the number of DVR grid points per DOF is shown in blue.	111
5.24	The diabatic state population of the donor state showing the decay of the donor state with 2, 4, 9 and 17 modes. The inset shows the magnification of the plot from 0 - 70 fs for clarity	111
5.25	The diabatic state population of the donor state showing the decay of the donor state with a $\lambda = 0.1 \rightarrow 0.5$ eV, with a $\kappa^d = \kappa^a = \pm 0.1$ eV.	114
5.26	The diabatic state population of the donor state showing the effect on the decay of the donor state by altering the κ^d and κ^a parameters.	115
5.27	The diabatic state population of the donor state showing the effect off adding more vibronic coupling into the model, the 3D system consists of the 2 pseudo-modes of the anti-symmetric and symmetric stretches, and ν_6 . The 4D system has the additional ν_7 modes. . . .	116
5.28	The diabatic state population of the donor state showing the effect off adding more vibronic coupling into the model, comparing the 4D and 9D system.	117

6.1	The ground state double well potential of the reaction coordinate for the proton transfer in salicylaldimine . The more stable tautomer occurs with the hydrogen on the nitrogen.	122
6.2	The initial state in approximated to be in a harmonic potential which lies in the global minimum of the quartic double well	126
6.3	Using the thermalised-MCTDH method, the step function expectation value as a function of time for the 2D salicylaldimine system, including ν_1 and ν_{36} , for various temperatures ranging from 0 \rightarrow 3000 K.	130
6.4	Using the exact method, the step function as a function of time for the 2D salicylaldimine system, including ν_1 and ν_{36} , for various temperatures ranging from 0 \rightarrow 3000 K.	132
6.5	Using the ρ -MCTDH(II) method, the step function expectation value as a function of time for the 2D salicylaldimine system, including ν_1 and ν_{36} , for various temperatures ranging from 0 \rightarrow 3000 K.	134
6.6	Using the ρ -MCTDH(II) method, the step function expectation value as a function of time for the 4D salicylaldimine system, for various temperatures ranging from 0 \rightarrow 3000 K.	135
6.7	Using the ρ -ML-MCTDH(II) method, the step function expectation value as a function of time for the 4D salicylaldimine system, for various temperatures ranging from 0 \rightarrow 3000 K.	136
6.8	The ML-tree used to describe the nuclear wavefunction in the ρ -ML-MCTDH(II) method including 4 DOF. As an example, the number of SPFs in each layer is shown in black, with the number of primitive basis functions shown in blue were used in the 500 K propagation, but the number of SPFs required vary with temperature.	137

6.9	The ML-tree used to describe the nuclear wavefunction in both the ρ -ML-MCTDH(I) method including 8 DOF. As an example, the number of SPDOs in each layer is shown in black, with the number of primitive basis functions shown in blue were used in the 500 K propagation, but the number of SPDOs required vary with temperature.	139
6.10	The ML-tree used to describe the nuclear wavefunction in both the ρ -ML-MCTDH(I) method including all available 13 DOF. As an example, the number of SPDOs in each layer is shown in black, with the number of primitive basis functions shown in blue were used in the 500 K propagation, but the number of SPDOs required vary with temperature.	139
6.11	Using the ρ -ML-MCTDH(I) method, the step function as a function of time for the 8D salicylaldimine system for temperatures 0, 500, and 2000 K.	140
6.12	Using the ρ -ML-MCTDH(I) method, the step function as a function of time for the 13D salicylaldimine system for temperatures 0, 500, and 2000 K.	141

List of Tables

4.1	The irreducible representation product table for D_{2d} symmetry . . .	55
4.2	Vibrational frequencies of normal modes of ground state neutral allene taken with MP2/6-311++G(2d,2p) level of theory. All vibrations were calculated using Gaussian 09 program.	57
4.3	The ionisation potentials for allene calculated using EPT and CAS(3,4) compared to the experimental values	58
4.4	A table showing all the fitting parameters of the polynomials used to fit against the <i>ab initio</i> points calculated in VCHam using EPT.	60
4.5	The calculated coupling constants for the \tilde{X}^2E state of allene radical cation, where the off-diagonal λ value refers to the ν_4 mode. The identical frequency of modes ν_1 and ν_5 is purely coincidental.	60
4.6	A table showing the fitting parameters of the polynomials for the significant ν_4 and ν_6 modes used to fit against the <i>ab initio</i> points calculated in VCHam using CASSCF.	62
4.7	Number of SPFs and primitive basis functions for the modes involved in a 3d calculation for Allene	63
4.8	The number of SPFs used for the modes involved in a 7d calculation for Allene	64
4.9	The timings of the propagation of allene to calculate the photoelectron spectrum, using MCTDH and ML-MCTDH, comparing a system containing 3, 7 and 15 DOF.	67

5.1	The coupling strengths of the main vibrations in Coumarin-343. All values are mass-frequency scaled. It is clear from the table that mode 6 is by far the most significant mode for electron transfer, which is a rocking motion of the carboxyl group.	84
5.2	This table shows that the first excited state of C-343 arises from the promotion of an electron from the HOMO to the LUMO, as confirmed by both EOM-CCSD and TDDFT. This is compared to the experimental absorption λ_{max} of C ₃₄₃ obtained in methanol. . .	87
5.3	Parameters taken from the results reported by Kondov et al [123]. The κ values were reported in mass-scaled units, thus the κ parameters presented here are not directly comparable to the κ parameters calculated later on in this chapter.	95
5.4	All parameters are taken from the results reported by Kondov et al [123]. The κ values here were all reported in mass-scaled units, so have been converted to mass-frequency scaled units.	96
5.5	All parameters are taken from the results reported by Kondov et al [123]. The κ values were reported in mass-scaled units, so have been converted into mass-frequency scaled units.	99
5.6	The anti-symmetrical and symmetrical stretches of the C-343 - TiO ₂ complex.	113
6.1	The coupling parameters for the 13 most significant modes for proton transfer in salicylaldehyde	124
6.2	The table of fitting parameters for the quartic polynomial for ν_1 . .	124
6.3	The number of propagations needed for the thermalised-MCTDH method to converge. The different propagations within each temperature each begin with a different seed	132

6.4	The number of SPFs needed to converge the 4D salicylaldehyde ρ -MCTDH(II) calculations, along with the timings.	136
6.5	A comparison of the timings for the ρ -MCTDH(I) and ρ -ML-MCTDH(II) method for a 4D salicylaldehyde system at various temperatures. . .	137
6.6	A table showing the time taken to run the propagations for the 8D and 13D systems, at 0, 500, and 2000 K.	141
A.1	A table showing the calculated frequencies and κ values for Coumarin-343	i

Glossary

ab initio Methods which solve the Time Independent Schrödinger equation, without the use of experimental data. x, 28, 30, 39, 56, 58, 60, 62, 117, 122, 143

ansatz In physics and mathematics, an ansatz is an educated guess that is verified later by its results. 2

BOA Born-Oppenheimer approximation. 1, 8, 12, 28–30, 143

C₃₄₃ Coumarin-343. A dye molecule. 4

C-343 The dye molecule Coumarin-343. 77

CASSCF Complete Active Space Self Consistent Field method. 35, 57, 144

DFT Density Functional Theory. 37–39, 78

DOF Degree(s) of Freedom. 2, 15, 41, 69, 108, 145

DSSC Dye sensitised solar cell. 26, 118, 121, 143

DVR Discrete Variable Representation. 40, 63, 131, 133

EOM Equation(s) of motion. 42

EOM-CCSD Equation of motion coupled cluster there. 86

EPT Electron propagator theory. 36, 57, 144

FFT Fast Fourier Transform. 40

HF Hartree Fock method(s). 31

HOMO Highest occupied molecular orbital. 36, 52, 78, 86

LCAO Linear combination of atomic orbitals, sometimes extended to LCAO-MO
(see MO glossary entry below). 33

LDA Local density approximation. 39

LUMO Lowest unoccupied molecular orbital. 86

LVNE The Liouville-von Neumann equation. 10

MC-TDSCF Multi-configurational time-dependent self-consistent field. 43

MCTDH Multi-Configurational Time Dependent Hartree method of solving the
Time Dependant Schrödinger Equation. 2, 43, 63, 120, 143

ML-MCTDH Multi-Layer Multi-Configurational Time Dependent Hartree method.
2, 45, 52, 64, 108, 116, 120, 121, 143

ML-tree The tree structure which arises due the continued expansion of single
particle functions in the Multi-Layer Multi-Configurational Time Dependent
Hartree method. 45, 64, 108, 136

MO Molecular-Orbital. 88

MP2 Møller-Plesset second order perturbation theory. 56

PES Potential energy surface. 8, 28, 29, 54, 69, 78, 121

SPDO single-particle density operator(s). ix, 48, 129, 139

SPF Single particle function. viii, 2, 129, 131, 133, 137

TDDFT Time dependent Density Functional Theory. 86

TDH Time dependent Hartree method. 42

TDSCF Time dependent self consistent field method. 42

TDSE Time Dependent Schrödinger Equation. 1, 10, 143

TISE Time Independent Schrödinger Equation. 9, 12, 28, 29, 34

VCHam Vibronic Coupling Hamiltonian program to parameterise a vibronic-coupling Hamiltonian. 56, 122

ZPE Zero point energy. 131

Chapter 1

Introduction

Experimental data can be crucially important in determining the behaviour of chemical systems, and analysis of the data obtained through spectroscopy and reaction cross-sections is one key example of this. However, to be able to fully explain why and how a lot of the observed behaviours occur, the system must also be studied computationally. Although classical mechanics is often sufficient to explain the dynamics in simple ground state chemical systems, explaining observations such as the quantisation of nuclear motion observed in many experimental spectra, as well as tunnelling and various aspects of chemical bonding can only be explained by considering the quantum effects on the system. Gaining this insight into the quantum behaviour of chemical systems is imperative in understanding why these systems behave the way they do. In order to determine the quantum dynamics of a system, i.e. the time evolution of a set of quantum particles, one must solve the Time Dependent Schrödinger Equation (TDSE),

$$i\hbar\dot{\Psi}(R, r, t) = \hat{H}\Psi(R, r, t). \quad (1.1)$$

This equation shows how the system, Ψ , evolves over time according to the Hamiltonian operator, \hat{H} . $\dot{\Psi}$ represents the time derivative of Ψ , $\frac{\partial\Psi}{\partial t}$, i is the imaginary unit, where $i = \sqrt{-1}$, and \hbar is the reduced Planck's constant, where $\hbar = \frac{h}{2\pi}$. The Born-Oppenheimer approximation (BOA) stipulates that the full wavefunction, Ψ , can be separated into nuclear and electronic motion, and is the

first step in solving this TDSE. This results in a nuclear wavepacket moving in time over a stationary electronic energy surface. This derivation, along with what happens when this approximation breaks down in non-adiabatic systems, can be found in chapter 2.

However, the key problem, and what the whole field of dynamics is built on, is that the TDSE can only be solved exactly for very simple molecules. This is due to the computational effort required, which scales exponentially by N^f , where N is the number of grid points, and f is the number of degrees of freedom. It has therefore been necessary to develop methods which can best approximate the solution to the TDSE. There is a vast range of methods which have been developed for this purpose, which range from classical, to semi-classical and lastly to complete quantum methods. An overview of some of these methods are discussed in more detail in chapter 3. The focus of this thesis is primarily on using full quantum methods to solve the TDSE, namely the Multi-Configurational Time Dependent Hartree method (MCTDH). This method expands the nuclear wavefunction into a set of time dependent basis functions, called single particle functions, SPFs, and is widely regarded as the most robust method to solve the TDSE in a full quantum manner. This method, despite accurately simulating dynamics of small molecules, scales computationally to n^f , where n is the number of SPFs and f is the number of degrees of freedom, DOF. This exponential scaling means that this method, as with all quantum methods, is limited with regards to the size of the system.

An advancement on this method, which allows one to partially circumvent this issue, is the development of the Multi-Layer MCTDH method (ML-MCTDH). The basic principle of this method is that each SPF of the standard MCTDH ansatz can be itself expanded in the same way. This cascading approach allows very large systems to be treated in a quantum way. This method, and its limitations, is discussed further in chapter 3. In this thesis, the flexibility of the ML-MCTDH

approach will be shown, especially when coupled with a vibronic coupling Hamiltonian, which includes the non-adiabatic effect of the coupling between nuclear motion and the electronic energy surfaces, and just three examples of how this extremely powerful method can be implemented will be shown in chapters 4, 5 and 6.

Chapter 4 will show how quantum dynamics can be used to accurately predict spectra, specifically in this case, the photoelectron spectrum of Allene. The ground electronic state of cationic Allene is doubly degenerate, shown in figure 1.1. The molecule in this state undergoes a Jahn-Teller distortion so, despite its small size, it is not a simple molecule to model computationally. The ML-MCTDH approach

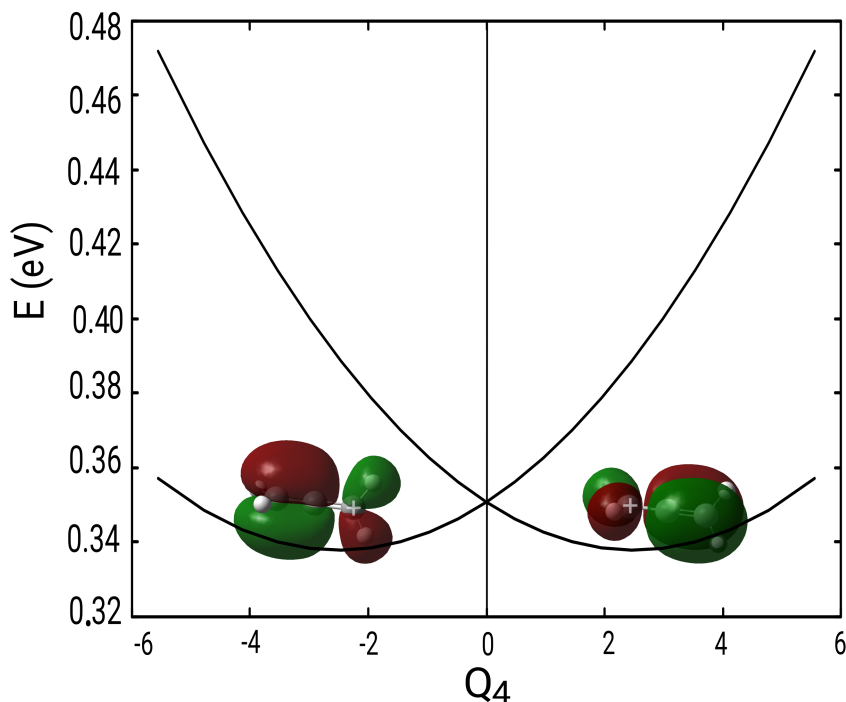


Figure 1.1: The doubly degenerate cationic ground state of Allene, showing a Jahn-Teller conical intersection at the Franck-Condon point.

allows all 15 DOF of Allene to be easily included in the calculations, which is at the limits of the standard MCTDH approach, as well as for other quantum methods. The ability to predict and explain the spectra of molecules this way has several obvious advantages. Computationally resolving spectrum means that any experi-

mental difficulty, be that equipment limitations, safety hazards or time concerns, are completely by-passed. Along with the ability to systematically rationalise the peaks in the spectra and the ability to study unstable molecules means that this is an essential tool in understanding molecular energetics.

Chapter 5 will show that the ML-MCTDH approach can not only be applied to small molecules like Allene, but is also robust enough to simulate dynamics in large systems, in this example, an electron transfer from the dye molecule, Coumarin-343, C_{343} , into a TiO_2 semiconductor.

Semiconductors are very important materials, and are used in a wide range of applications from household electronics to being essential in the development of sustainable energy sources. They are important as components in solar cells due to their unique electronic behaviour. By coupling the semiconductor to a suitable molecule, as seen in figure 1.2, an electron transfer between the donor molecule and the semiconductor can be observed. This system involves an electron being transferred from an excited donor state of the dye molecule into the conduction band of the semiconductor.

However, the pathway of this excitation, and especially the recombination mechanism is still not well understood. In order for more efficient solar cells to be developed, it is key that this process is better understood. The development of these more efficient solar cells will be discussed further in 2.7.2.

The final application of the ML-MCTDH method which will be demonstrated in this thesis in chapter 6 is the ability to propagate density matrices instead of wavefunctions in order to simulate quantum dynamics at temperatures greater than zero Kelvin. The system that this method is demonstrated on is a ground state intramolecular proton transfer in salicylaldehyde. This system has a double well potential energy surface along the reaction coordinate, with the height of the barrier equating to ~ 1500 Kelvin.

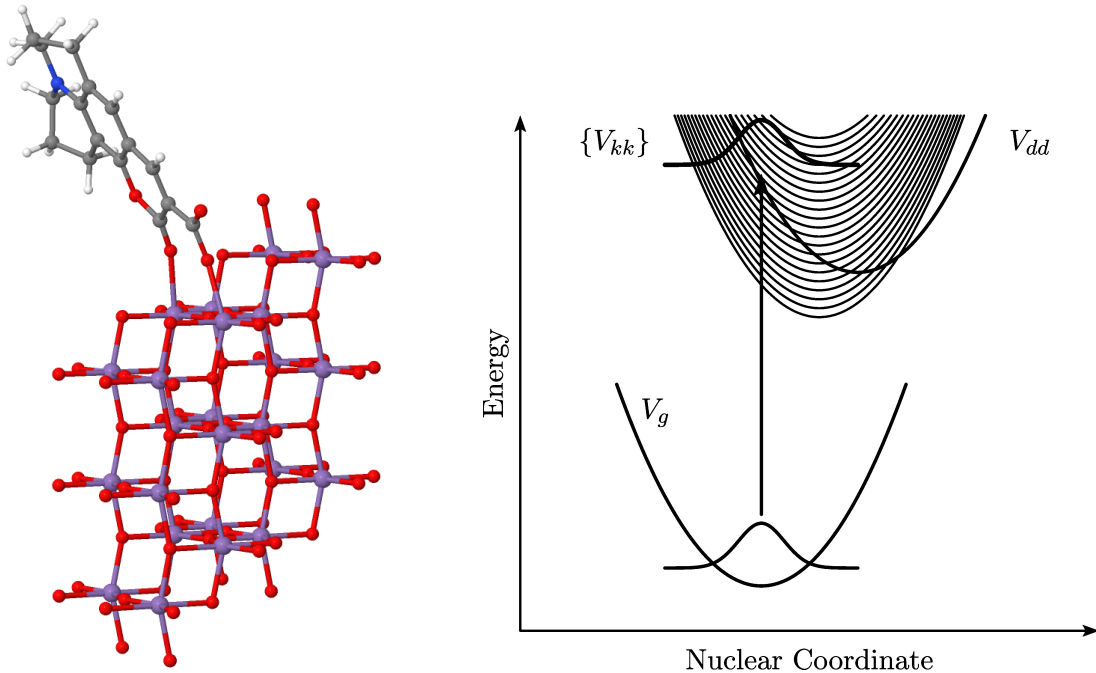


Figure 1.2: (a) A Coumarin-343 dye molecule attached to the surface of TiO_2 semiconductor and (b) the corresponding energy levels. V_g denotes the ground state of the dye molecule, V_{dd} the donor state, which corresponds to the excited state of the dye molecule, and V_{kk} denotes the acceptor states, which correspond to the discretised conduction band of the semiconductor. The process of the ground state wavepacket being excited into the donor state is also shown, which is the initial step of the electron transfer process [1].

Probing the dynamics of systems which use heat to overcome an activation barrier is something that cannot be easily done using the MCTDH approach alone, as these methods have been designed to be performed on closed systems, at zero Kelvin. There are adaptations to this method which account for temperature, but it still excludes some important coherence effects. Using density matrices allows one to not only probe systems at a finite temperature, but also allows open systems to be investigated in a quantum manner. This means that environmental effects, such as solvents, can also be included in this method. Previous implementations of this method have coupled the standard MCTDH approach with density matrices with a great degree of success. However, where the standard MCTDH approach represents the nuclear wavefunction as a vector, the density matrix method represents the

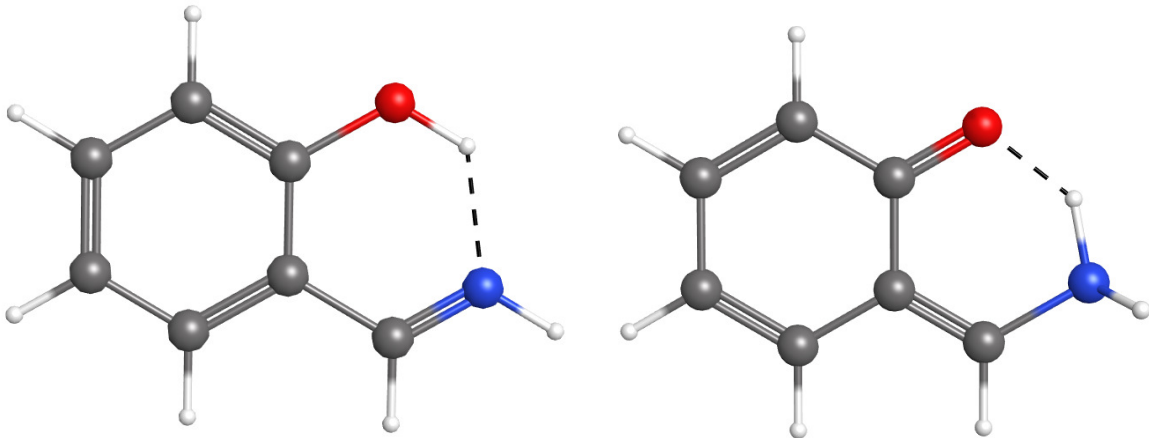


Figure 1.3: Salicylaldehyde exhibits an intramolecular hydrogen transfer from the oxygen to the nitrogen.

nuclear wavefunction as a matrix. Therefore, as the computational effort is that of MCTDH squared, this method quickly becomes, once again, size restrictive. This thesis explores the idea of coupling the ML-MCTDH approach with density matrices, in order to allow larger systems to be investigated. This novel approach has the potential to be an excellent tool in the investigation of several types of important biological and chemical systems, where temperature and environment play a significant role.

Chapter 2

Background and Theory

2.1 Introduction

The Born-Oppenheimer approximation [2] is the starting point for the determination of the dynamics of most chemical processes. Due to the nuclei being much heavier than the fast-moving, low mass electrons, the BOA assumes that the dynamics of a system are dominated by a single electronic energy surface [3], with the nuclei moving over the electronic potential energy surface. While this simplification of a chemical process is sufficient to explain a wide range of processes, such as in simple absorption and photoelectron spectroscopy [4], it often breaks down for more complicated processes and leads to some unpredictable outcomes. This break down of the BOA arises due to the coupling between the electronic motion and the nuclear motion (called vibronic coupling), and is most significant in systems where there are two or more electronic states which are close in energy. This will be discussed further in section 2.4. When the energy of these states become degenerate, the coupling becomes infinitely large, the BOA completely breaks down and a conical intersection is formed, an example of which can be seen in figure 2.1.

These conical intersections are essential phenomena in many photo-excited chemical processes and allow interstate crossing on femtosecond timescales [5, 6]. These intersections can be classed depending on their relative energies and how

they arise, and are discussed more in depth in section 2.6. These principles of quantum dynamics can be applied to electron transfer schemes, which are of importance in several chemical processes, including being a key step in the use of semiconductors as solar cells, which is discussed in depth in chapter 2.7.

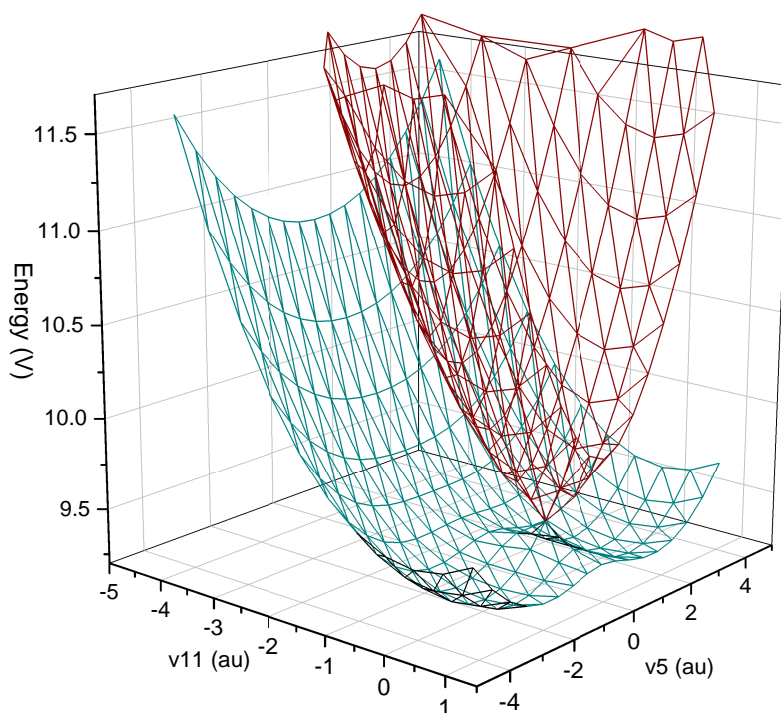


Figure 2.1: An example of a conical intersection. This is a 'Mexican hat' potential surface showing the crossing point of the adiabatic doubly degenerate ground electronic state of the Allene cation along the $\nu 5$ (torsion) and $\nu 11$ (C-C asymmetric stretch) modes

2.2 The Schrödinger Equation

To predict the dynamics of any system, one must start with the fundamentals of the BOA. The assumption that the BOA implements is that the nuclear and electronic motion can be separated [5], and the dynamics of the system can be described by a nuclear wavepacket evolving in time over an adiabatic, static PES. The evolution of the nuclear wavepacket is described by the solution to the TDSE,

$$i\hbar \frac{\partial}{\partial t} \Psi(R, r, t) = \hat{H} \Psi(R, r, t), \quad (2.1)$$

where \hat{H} is the molecular Hamiltonian operator, $i = \sqrt{-1}$, \hbar is the reduced Planck's constant where $\hbar = \frac{h}{2\pi}$, Ψ is the full wavefunction, and (R, r, t) are the nuclear, electronic and time coordinates respectively.

The static PES are determined by solving the time independent Schrödinger equation, TISE,

$$\hat{H} \Psi = E \Psi, \quad (2.2)$$

where the Hamiltonian operator, \hat{H} , acts upon wavefunction Ψ .

The molecular Hamiltonian operator has been derived from the classical Hamiltonian function,

$$H = T + V, \quad (2.3)$$

where T is the classical kinetic energy, $T = \frac{p^2}{2m}$ and V is the classical potential energy, $V = V(q)$. Here, p and m are the momentum and mass of the particle respectively, and q is the spatial coordinates. In quantum mechanics, the Hamiltonian becomes an operator, with the kinetic and potential terms becoming operators also, thus being written as,

$$\hat{H}(R, r) = \hat{T}_n(R) + \hat{H}_{el}(r, R), \quad (2.4)$$

where H_{el} is the electronic Hamiltonian and contains all the potential operator terms and \hat{T}_n is the nuclear kinetic operator.

$$\hat{T}_n(R) = - \sum_i \frac{\hbar^2}{2m_i} \nabla_i^2, \quad (2.5)$$

where m is the mass of nucleus i . The full equation can thus be expanded as,

$$\hat{H}(R, r) = - \sum_i \frac{\hbar^2}{2m_i} \nabla_i^2 + \hat{T}_{el}(r) + \hat{V}_{ee}(r) + \hat{V}_{ne}(r, R) + \hat{V}_{nn}(R). \quad (2.6)$$

\hat{H}_{el} is dependent on both nuclear and electronic coordinates. This is also known as the clamped-nucleus Hamiltonian as it is derived by setting the nuclear kinetic energy to zero,

$$\hat{H}_{el}(R, r) = \hat{T}_{el}(r) + \hat{V}(R, r), \quad (2.7)$$

where $\hat{V}(R, r)$ contains all the potential operators shown above in equation 2.6.

2.3 Density Matrices

Thus far, all the nuclear wavefunctions discussed in this chapter have been represented as vectors, and can be described as pure states, i.e. the initial state of the time evolution of the system is well-defined. When the initial state is no longer pure, but an incoherent mixture of states, using density matrices can move beyond this pure wavepacket picture. This statistical mixture can be written using the density operator, ρ [7],

$$\rho = \sum_n P_n |\Psi_n\rangle \langle \Psi_n|, \quad (2.8)$$

where $0 \leq P_n \leq 1$ is the probability of being in state $|\Psi_n\rangle$. The time evolution of a mixed state system can no longer be described using the TDSE, but instead is described using the Liouville-von Neumann equation, LVNE,

$$i\dot{\rho} = \mathcal{L}(\rho), \quad (2.9)$$

where \mathcal{L} is the Liouvillian superoperator. This can be shown to be the equivalent of the TDSE if the initial wavefunction is pure. The density matrix of a pure quantum state, $|\Psi\rangle$, can be written as,

$$\rho = |\Psi\rangle\langle\Psi|. \quad (2.10)$$

The time derivative of this equation, following the product rule, can be written as,

$$\frac{d}{dt}\rho = \frac{d}{dt}(|\Psi\rangle\langle\Psi|) = \left(\frac{d}{dt}|\Psi\rangle\right) \cdot \langle\Psi| + |\Psi\rangle \cdot \left(\frac{d}{dt}\langle\Psi|\right). \quad (2.11)$$

The TDSE equation, $i\hbar|\dot{\Psi}\rangle = \hat{H}|\Psi\rangle$, can be written as,

$$\frac{d}{dt}|\Psi\rangle = -\frac{i}{\hbar}\hat{H}|\Psi\rangle. \quad (2.12)$$

The complex conjugate of which is,

$$\frac{d}{dt}\langle\Psi| = +\frac{i}{\hbar}\langle\Psi|\hat{H}. \quad (2.13)$$

Substituting this into the time derivative of the density operator equation, equation 2.11, and setting \hbar to atomic units so that $\hbar = 1$, one can derive,

$$\frac{d}{dt}\rho = -i\hat{H}|\Psi\rangle\langle\Psi| + i|\Psi\rangle\langle\Psi|\hat{H}, \quad (2.14)$$

$$\frac{d}{dt}\rho = -i\hat{H}\rho + i\rho\hat{H}, \quad (2.15)$$

$$\frac{d}{dt}\rho = -i[\hat{H}, \rho]. \quad (2.16)$$

Therefore, for closed systems the LVNE can be simplified to that in equation 2.9, where

$$\mathcal{L}(\rho) = [\hat{H}, \rho] \quad (2.17)$$

For open systems, there are several approaches for defining \mathcal{L} , especially to account for environment effects. Three of the most prominent approaches include the Lindblad [8], the Redfield [9], and the Caldeira and Leggett [10, 11] approaches. Approaches as to how the density matrix can be developed within the MCTDH formalism will be discussed in chapter 3, and an example of how these methods can be used on thermalised systems will be shown in chapter 6.

2.4 The Born-Oppenheimer Approximation

The BOA asserts that as the mass of a nucleus is so much greater than that of an electron, that the electron's motion is instantaneous compared to that of the nucleus. This basic assumption means that effectively the nuclei move on a static energy surface, and that the full wavefunction can be separated into the electronic and nuclear components,

$$\Psi(R, r, t) = \sum_i \chi_i(R, t) \psi_i(r; R), \quad (2.18)$$

where i is the electronic state, $\chi_i(R, t)$ is the time dependent nuclear wavefunction in the i^{th} electronic state, acting as expansion coefficients in equation 2.18 and ψ is the electronic wavefunction. The electronic wavefunction is not time dependent and can be obtained independently by solving the electronic time independent Schrödinger equation, TISE, at various nuclear geometries to form the PES over which the nuclear wavefunction will move. Equation 2.18 is known as the Born-Huang representation [12], or Born representation, and is formally exact if an infinite number of electronic states are included. This linear combination of electronic wavefunctions representing the full molecular wavefunction allows non-adiabatic effects to be incorporated.

In atomic units, the TDSE can be written in the simplified form shown below,

$$i\dot{\Psi} = \hat{H}\Psi, \quad (2.19)$$

where $\dot{\Psi}$ is the partial derivative of Ψ with respect to time. Substituting in the full wavefunction expressed in equation 2.18, and knowing that the molecular Hamiltonian can be written as a combination of kinetic and potential operators, as shown in 2.4, one can obtain the following,

$$i \sum_i \dot{\chi}_i \psi_i = (\hat{T}_n + \hat{H}_{el}) \sum_i \chi_i \psi_i. \quad (2.20)$$

If we left multiply by a complex conjugate of one electronic wavefunction, $\psi_j(r; R)$, and integrate over the electronic coordinates, it results in a form in which all coupling terms are included. This process is shown below,

$$i \int \psi_j^* \sum_i \dot{\chi}_i \psi_i dr = \int \psi_j^* (\hat{T}_n + \hat{H}_{el}) \sum_i \chi_i \psi_i dr. \quad (2.21)$$

Due to the orthonormality of the electronic wavefunctions, all $\langle \psi_j | \psi_i \rangle$ terms disappear, except when $j = i$, resulting in equation,

$$i \dot{\chi}_j = \underbrace{\sum_i \int \psi_j^* \hat{T}_n \chi_i \psi_i dr}_1 + \underbrace{\sum_i \int \psi_j^* \hat{H}_{el} \psi_i \chi_i dr}_2. \quad (2.22)$$

Part 2 of equation 2.22 can be easily simplified, as shown in the following,

$$\begin{aligned} \sum_i \int \psi_j^* \hat{H}_{el} \psi_i \chi_i dr &= \hat{H}_{el} \int \psi_j^* \psi_i dr \chi_i, \\ &= E_j \int \psi_j^* \psi_i dr \chi_i, \\ &= E_j \chi_j, \end{aligned} \quad (2.23)$$

where $\hat{H}_{el} \Psi_j = E_j \Psi_j$ is the electronic Hamiltonian operating on the j th electronic state.

If we make the assumption that the electronic wavefunctions ψ_i and ψ_j are completely free of any dependency on the nuclear kinetic energy, as per the BOA, then part 1 of equation 2.22 can also be similarly simplified,

$$\sum_i \int \psi_j^* \psi_i dr \hat{T}_n \chi_i = \hat{T}_n \chi_j. \quad (2.24)$$

These simplifications lead to the adiabatic Born-Oppenheimer approximation,

$$i \dot{\chi}_j = (\hat{T}_n + E_j) \chi_j. \quad (2.25)$$

However, the assumption that the electronic state is not dependent on the nuclear kinetic energy is only an approximation. Therefore, the resulting equation shown in equation 2.24 is an oversimplification. To correct for this, we must add in coupling terms by having the kinetic energy operator acting on the electronic wavefunctions, rather than being separated from them, shown below.

$$\left[-\frac{1}{2M} \int \psi_j^* \frac{\partial^2}{\partial R^2} \psi_i dr \right] \chi_i. \quad (2.26)$$

This equation comes about by taking the kinetic operator from the Hamiltonian, shown in equation 2.6 and substituting into equation 2.24 [Atomic units are taken, so $\hbar = 1$].

After applying the product rule, and simplifying, part 1 of equation 2.22 can be written as,

$$\left[\underbrace{-\frac{1}{2M} \int \psi_j^* \psi_i dr}_{\hat{T}_n} \nabla^2 - \frac{1}{2M} \int 2 \underbrace{\psi_j^* \nabla \psi_i}_{F_{ji}} dr \nabla - \frac{1}{2M} \int \underbrace{\psi_j^* \nabla^2 \psi_i}_{G_{ji}} dr \right] \chi_i, \quad (2.27)$$

where ∇ and ∇^2 are the first and second partial derivatives with respect to nuclear coordinates, $\frac{\delta}{\delta R}$ and $\frac{\delta^2}{\delta R^2}$, respectively. The first term in equation 2.27 is simply the nuclear kinetic energy, as shown in equation 2.24, and thus can be written as such. Thus equation 2.22, the TDSE, can be written as follows,

$$i\dot{\chi}_j = \left(\hat{T}_n + E_j \right) \chi_j + \left(\sum_i \Lambda_{ji} \right) \chi_j, \quad (2.28)$$

where Λ_{ji} is the non-adiabatic coupling matrix which is as follows,

$$\Lambda_{ji} = -\frac{1}{2M} (2F_{ji} \nabla + G_{ji}). \quad (2.29)$$

G_{ji} are the scalar derivative couplings, a matrix of numbers, and F_{ji} are the derivative non-adiabatic coupling vectors. These terms couple the electronic and

nuclear motion. It is clear that as the mass increases, the coupling terms become diminishingly small, and can eventually be ignored completely.

The introduction of these correction terms means that equation 2.28 is a complete solution of the TDSE. This is the diabatic picture.

Although the TDSE obtained using the BOA, equation 2.25, is sufficient to explain many chemical processes, it has been shown that as the method is applied to more complex situations, for example probing excited state chemistry in polyatomic molecules, this adiabatic approximation breaks down [13, 14]. This break down of the BOA is due to coupling of the electronic motion and the nuclear motion (called vibronic coupling) in areas where two or more potential energy surfaces become close in energy to each other, which is inevitable in systems with many degrees of freedom (DOF) [5]. This break down of the BOA arises due to the non-diagonal coupling term mentioned above, F_{ji} . These can be determined by using the product rule on the Hellmann-Feynman theorem [15],

$$\nabla \langle \psi_i | \hat{H}_{el} | \psi_j \rangle = \langle \nabla \psi_i | \hat{H}_{el} | \psi_j \rangle + \langle \psi_i | \hat{H}_{el} | \nabla \psi_j \rangle + \langle \psi_i | \nabla \hat{H}_{el} | \psi_j \rangle. \quad (2.30)$$

Due to the fact that the electronic wavefunctions are eigenvalues of \hat{H}_{el} , equation 2.30 can be reduced to,

$$\nabla \langle \psi_i | \hat{H}_{el} | \psi_j \rangle = \langle \nabla \psi_i | \psi_j \rangle E_j + E_i \langle \psi_i | \nabla \psi_j \rangle + \langle \psi_i | \nabla \hat{H}_{el} | \psi_j \rangle. \quad (2.31)$$

As the partial derivative operator, ∇ , is anti-Hermitian, this above equation can be rearranged, and set to zero.

$$\nabla \langle \psi_i | \hat{H}_{el} | \psi_j \rangle = \langle \psi_i | \nabla \psi_j \rangle (E_i - E_j) + \langle \psi_i | \nabla \hat{H}_{el} | \psi_j \rangle = 0. \quad (2.32)$$

Substituting F_{ji} into equation 2.32, one obtains the following expression,

$$F_{ij} = \langle \psi_i | \nabla \psi_j \rangle = \frac{\langle \psi_i | \hat{H}_{el} | \psi_j \rangle}{E_j - E_i}. \quad (2.33)$$

It can be seen from equation 2.33 that as two electronic surfaces become close in energy, the F_{ij} coupling term becomes infinitely large as the difference in energy of two electronic states tends to zero. When these energies become degenerate, and the denominator becomes 0, there is a complete breakdown of this approximation. Regions of degenerate energies are called conical intersections, and are discussed in further detail in section 2.6.

A special case of this coupling is known as the Jahn-Teller (JT) effect. The JT effect states that "In an electronically degenerate state, a nonlinear molecule undergoes distortion to remove the degeneracy by lowering the symmetry and thus by lowering the energy.." [16] This is a spontaneous breaking of symmetry to remove degeneracy in molecules with high symmetry. This effect is driven by energetics, and that this distortion lowers the overall energy of the system. There have been several early studies on small systems exhibiting the JT effect, which were optimal systems to investigate due to the high symmetry in relatively small molecules allowing simple models to be easily applied [17, 18, 19]. This will be discussed further in section 2.6.1

2.5 Beyond the Born-Oppenheimer Approximation

Due to the break down of the adiabatic picture when electronic states are degenerate in energy, one can gain more information about the crossing point if a switch to the diabatic picture is made. In the diabatic picture, the electronic states are grouped in terms of chemical character, such as a bond stretch or a torsion angle, rather than in magnitude of energy. This leads to crossing of states, as in figure 2.2, rather than avoided crossings as in the adiabatic picture.

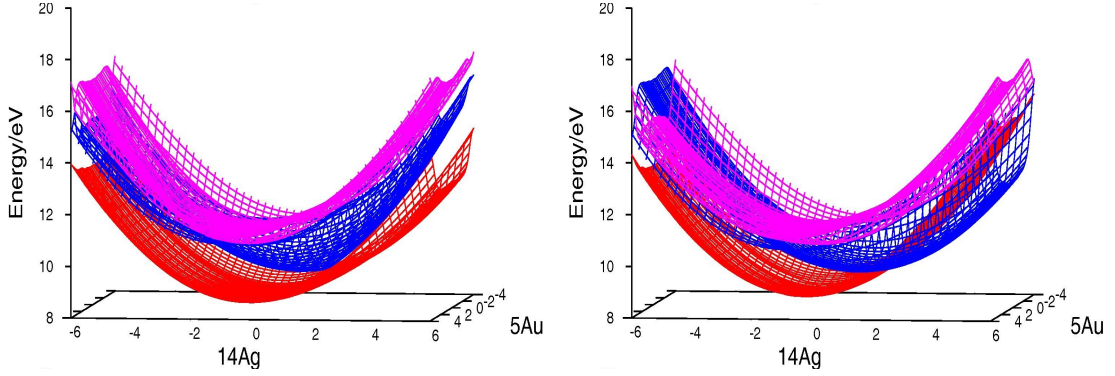


Figure 2.2: The same system shown in both the adiabatic picture (left) and the diabatic picture (right) These are the potential energy surfaces of the lowest three energy states of butatriene [20].

In order to transform into the diabatic picture, firstly, removing the G_{ji} term in equation 2.28 simplifies the equation. This can be achieved by considering the expansion of,

$$\begin{aligned} \sum_i (\nabla + F_{ji})^2 &= \sum_i (\nabla + F_{ji})(\nabla + F_{ji}) \\ &= \sum_i \nabla^2 + (\nabla \cdot F_{ji}) + (F_{ji} \cdot \nabla) + \sum_k (F_{jk} \cdot F_{ki}), \end{aligned} \quad (2.34)$$

where $\sum_k (F_{jk} \cdot F_{ki})$ is the matrix product. This expansion and rearrangement due to the anti-Hermitian nature of the $F_{ji} = -F_{ij}^*$ term leads to,

$$\begin{aligned} \sum_k (F_{jk} \cdot F_{ki}) &= \langle \psi_j | \nabla \psi_k \rangle \langle \psi_k | \nabla \psi_i \rangle \\ &= -\langle \nabla \psi_j | \psi_i \rangle \end{aligned} \quad (2.35)$$

The $(\nabla \cdot F_{ji})$ term above in equation 2.34 can be expanded as,

$$\begin{aligned} (\nabla \cdot F_{ki}) &= \langle \nabla \psi_j | \nabla \psi_i \rangle + \langle \psi_j | \nabla^2 \psi_i \rangle + \langle \psi_j | \nabla \psi_i \rangle \nabla \\ &= \langle \nabla \psi_j | \nabla \psi_i \rangle + G_{ji} + F_{ji} \cdot \nabla. \end{aligned} \quad (2.36)$$

Therefore, equation 2.28 can be rewritten in terms of F_{ji} only, so the whole equation can be written,

$$i\dot{\chi}_i = \left[-\frac{1}{2M} (\nabla + F_{ij})^2 + E_j \right] \chi_j. \quad (2.37)$$

As the F_{ji} term here still includes a singularity at degenerate energies, this term needs to be eliminated. Changing to the diabatic representation in these situations is the obvious choice, as these problematic non-adiabatic terms are removed from the TDSE. The Schrödinger equation can be expressed in the diabatic form,

$$i\tilde{\chi}_i = \sum_j \left(-\frac{1}{2M} \nabla^2 + W_{ij} \right) \tilde{\chi}_j, \quad (2.38)$$

where $\tilde{\chi}$ is the diabatic representation of the nuclear wavefunction and all coupling terms are now included in the non-diagonal W_{ij} potential matrix, with the adiabatic potential energies, E_j , as the eigenfunctions of matrix W_{ij} ,

$$W_{ij} = \langle \psi_i | \hat{H}_{el} | \psi_j \rangle, \quad (2.39)$$

where ψ_α is adiabatic state α .

Changing to the diabatic form can be done by a unitary transformation of the adiabatic wavefunctions into diabatic wavefunctions using an undetermined unitary matrix \mathbf{S} [21]. The adiabatic and diabatic wavefunctions are related to each other by $\tilde{\psi}_a = \sum_i S_{ai} \psi_i$; where \mathbf{S} is the unitary matrix and $\sum_a S_{ia} S_{aj}^\dagger = \delta_{ij}$. There is an assumption that the relationship $\nabla \mathbf{S} = -F \mathbf{S}$ is met for this transformation, where F is the non-adiabatic coupling term described earlier. Also, the matrix \mathbf{S} is specified at a point where the adiabatic and diabatic states are equivalent. This is typically the Frank-Condon point. For example, for the transformation of a 2-state system at a fixed nuclear geometry,

$$\begin{pmatrix} \psi_1 \\ \psi_2 \end{pmatrix} = \begin{pmatrix} \cos \alpha & \sin \alpha \\ -\sin \alpha & \cos \alpha \end{pmatrix} \begin{pmatrix} \tilde{\psi}_1 \\ \tilde{\psi}_2 \end{pmatrix}, \quad (2.40)$$

where α is the mixing angle between adiabatic states ψ_1 and ψ_2 . Using this equation in equation 2.39, one gets the following equations for both the on- and off-diagonal elements,

$$W_{11} = \langle \psi_1 | \hat{H}_{el} | \psi_1 \rangle = E_1 \cos^2 \alpha + E_2 \sin^2 \alpha, \quad (2.41)$$

$$W_{22} = \langle \psi_2 | \hat{H}_{el} | \psi_2 \rangle = E_1 \sin^2 \alpha + E_2 \cos^2 \alpha, \quad (2.42)$$

$$W_{12} = \langle \psi_1 | \hat{H}_{el} | \psi_2 \rangle = (E_1 - E_2) \cos \alpha \sin \alpha, \quad (2.43)$$

where E_i is the adiabatic potential energy of state i , W_{ii} are the diabatic potential energy matrix elements, and W_{ij} are the off-diagonal coupling elements between the electronic states.

2.6 Conical Intersections

As mentioned in the previous section, conical intersections occur when the energy of two electronic states become degenerate. This results in a surface where the electronic and nuclear motion can no longer be approximated to be separable, see figure 2.1 for an example of this point.

Conical intersections can be differentiated into different classes and topographies. They can be classified by the role of the point group symmetry in their existence [22]. There are three types of intersections: symmetry required, accidental symmetry allowed and accidental no symmetry intersections [23]. For a two-state conical intersection, two conditions are needed. When the electronic Hamiltonian is built in a diabatic basis, the following is obtained,

$$\mathbf{H}_{el} = \begin{bmatrix} H_{11} & H_{12} \\ H_{21} & H_{22} \end{bmatrix}. \quad (2.44)$$

For the eigenvalues of the two states to become degenerate, and therefore intersect, then $H_{11} = H_{22}$, and $H_{12} = H_{21} = 0$.

The non-crossing rule, first posited in 1929 [7], states that these two conditions cannot both be met in system with ≤ 2 degrees of freedom and thus form an avoided crossing, as in figure 2.3.

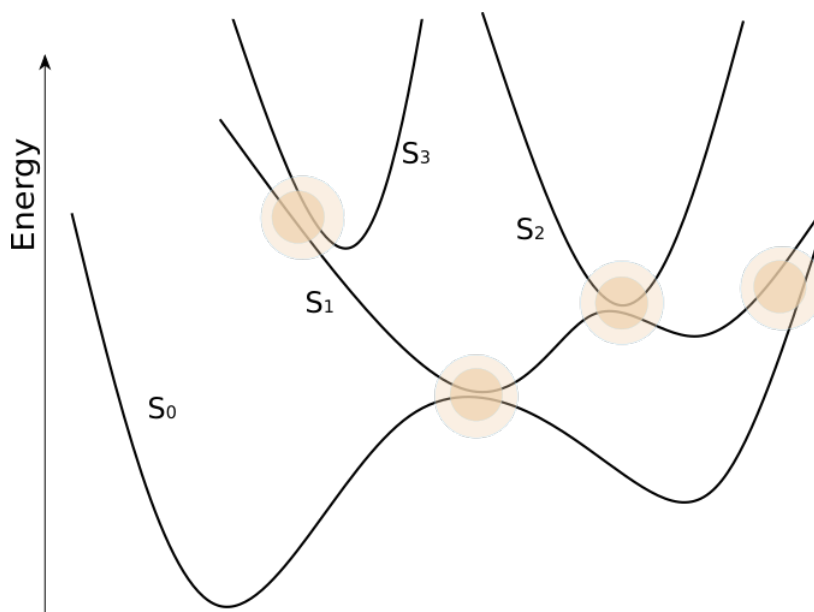


Figure 2.3: An example of several highlighted avoided crossings in a 4 adiabatic state system, adapted from reference [24].

As the dimensionality of these crossings is $N-2$, where N is the number of atoms in the system, for these diatomic molecules, there is only one internal coordinate—the interatomic distance, so the non-crossing rule can be applied. However, after many years of computations and experiments, it was proven not only that same symmetry crossings are ubiquitous in polyatomic molecules [23, 25, 26, 27], but they often play a crucial role in many chemical processes.

If the states involved in the intersection are of degenerate symmetry, such as those belonging to E or T representations, then both the conditions mentioned at the start of this section are met due to symmetry, and thus, these can be referred to as symmetry-required intersections. This type of intersection is also known as the Jahn-Teller effect and will be discussed further in section 2.6.1. If two or more non-degenerate states cross, then the resulting conical intersection can be classed as an accidental symmetry-allowed intersection or accidental no symmetry intersection. For the symmetry allowed intersection, it is assumed that for states with different

symmetry, the second condition mentioned above, $H_{12} = H_{21} = 0$, can be satisfied. However, the on-diagonal conditions only maybe meet at particular points R and so meets this condition accidentally. The final class is the accidental no symmetry intersections, where the conditions are met through no result of symmetry at all, and are purely accidental. These types of conical intersections are, therefore, difficult to locate and their significance has only been investigated properly in the last few years.

Conical intersections can also be categorised by their topology. They can be either peaked intersections, where the energy minimum of the higher energy level is also the point where the systems cross, as in part (a) in figure 2.4 They can also be sloped intersections, where the energy minimum is lower than the conical intersection, as in part (b) in figure 2.4. In the latter case, quantum tunnelling can be observed.

2.6.1 Jahn-Teller Systems

The Jahn-Teller effect refers to the degenerate states induced by symmetry, and have been extensively studied throughout the years. The Jahn-Teller theory states that a symmetrical molecule in a degenerate state will geometrically distort to lift the degeneracy in order to stabilise the state [16]. The vibrational modes which can break the degeneracy of the states is dependent on their symmetry. In general, degeneracy can be broken if the direct product of the two electronic states contains the symmetry element of the vibrational mode, i.e. the direct product of the two electronic states and the vibrational mode must include the totally symmetric mode, as shown in 2.45. These vibrational modes are said to be Jahn-Teller active.

$$\Gamma_i \otimes \Gamma_j \otimes \Gamma_\alpha \subset A_1, \quad (2.45)$$

where Γ_i and Γ_j are the electronic states, and Γ_α is the vibrational mode.

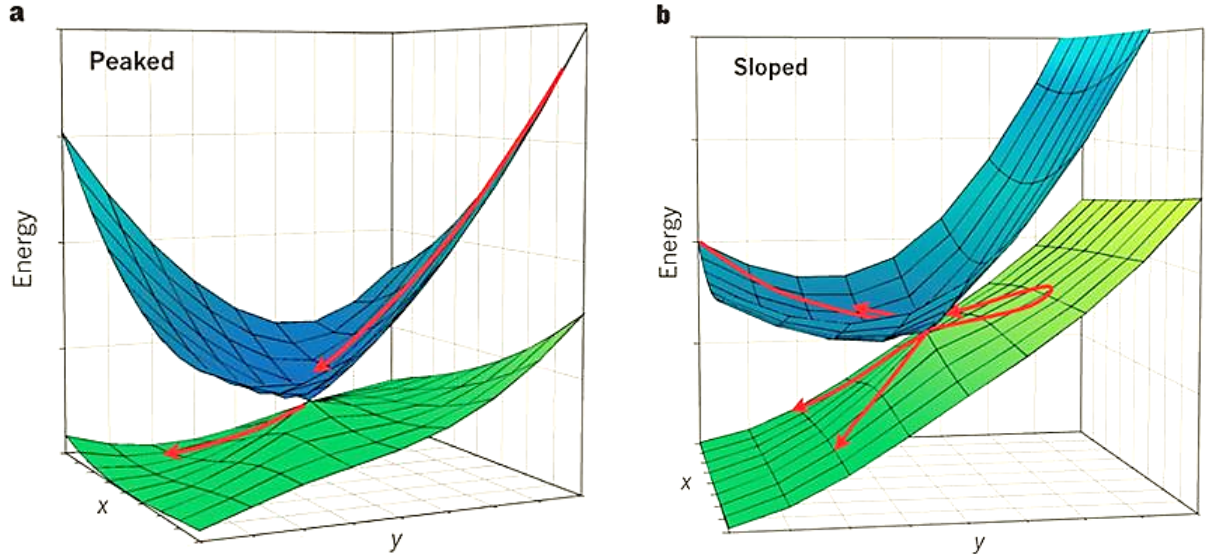


Figure 2.4: An schematic of (a) a peaked conical intersection and (b) a sloped intersection [28]. The excited wavepacket moves towards the conical intersection (red arrows) where in (a) the wavepacket passes through the intersection and continues on the lower energy level, and in (b) the momentum of the excited wavepacket causes the wavepacket to move to an area of energy higher than the intersection on the lower surface. This is the tunnelling, where the wavepacket moves to an area on the surface but does not have the energy to cross the energy barrier. The wavepacket then bifurcates in this example, as 2 possible pathways are available.

In a Jahn-Teller system, $i = j$, and so the product of $\Gamma_i \otimes \Gamma_j$ will always contain the totally symmetric symmetry group.

A common Jahn-Teller problem is the $E \otimes e$ effect. This is the case where a doubly degenerate mode of symmetry e lifts the degeneracy of a doubly degenerate electronic state, E [29, 30], and has been researched in many different systems [31, 32]. This is due to $E \otimes E \supset E + A$ in most non-Abelian point groups. As the totally symmetric representation cannot lift the degeneracy of the state, then vibrational modes which can couple and break degeneracy are the degenerate e modes, hence $E \otimes e$.

Another less common Jahn-Teller problem is the $E \otimes b$ effect. The direct product of the doubly degenerate E electronic state of certain symmetries do not reproduce the E representation, but instead result in the totally symmetric A

and the B irreducible representations, resulting in the $E \otimes b$ effect, where the degeneracy is lifted by pair of vibrations with b symmetries.

There has been research into this effect on molecules such as Allene [33, 34, 35] and pentatetraene [36]. These molecules are ideal systems to probe this $E \otimes b$ Jahn-Teller effect as they both belong to D_{2d} group, which shows this type of effect, and only have 15 and 21 DOF respectively. Therefore, due to the small size, the effects are easily modelled for all DOF in the system. The Jahn-Teller effect in Allene will be discussed further in chapter 4.

2.7 Semiconductors and Solar Cells

2.7.1 Why are semiconductors important?

The ultimate aim of this thesis was to simulate an electron transfer from a dye into a semiconductor. Semiconductors are materials which are only conductive under certain conditions. This arises due to the small energy gap between the valence and conduction bands of the solid material, meaning that a small input in energy is enough to promote electrons from the full valence band into the empty conduction band, allowing a free flow of electrons and thus behaving as an electrical conductor, as shown in figure 2.5.

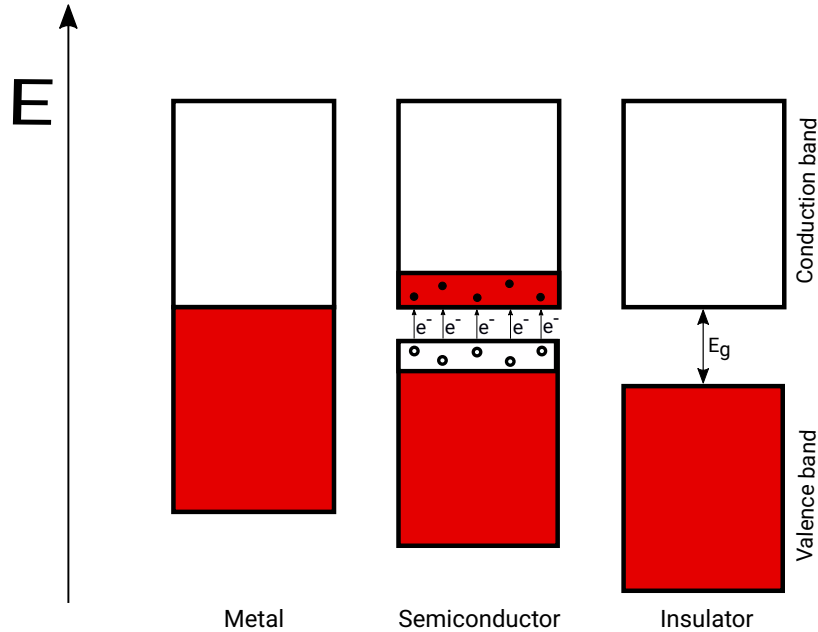


Figure 2.5: A schematic which shows the band structure of a metal, a semiconductor, and an insulator. One can see that with enough energy, the electrons in a semiconductor can be promoted into the conduction band and the material behaves as a metal.

Due to this property, semiconductors are very important materials and are used in a wide range of applications, from being an essential component in household electronics, to the advancement of semiconductor lasers [37], to the use in photovoltaic cells [38].

2.7.2 Solar Cells

Due to the fight against climate change and the search for more sustainable energy resources, there has been a growing interest in recent years in alternative, cleaner energy sources. One avenue of this research is using semiconductors to convert energy from the sun into electrical energy, in a photovoltaic cell. The sun emits energy in the infrared, visible and ultra-violet range, meaning that the band gap of a useful semiconductor should correspond to this energy, i.e. 0.5-5 eV. A large problem with semiconductors is that the efficiency of energy conversion is dependent on the width of the band gap, E_g . Too large a band gap, and only

photons with high energy will be able to promote electrons into the conduction band. However, too small an energy gap means that a large proportion of the energy from the photon is converted into thermal energy, which will decrease efficiency. There have been theoretical investigations which show that for a single P-N junction semiconductor, a band gap of 1.34 eV is the optimum width in order to reach the maximum efficiency with respect to the spectral energy distribution of the sun, the so-called Shockley-Queisser limit, after the initial paper on this calculation [39], see figure 2.6. Following on from this initial finding, early research

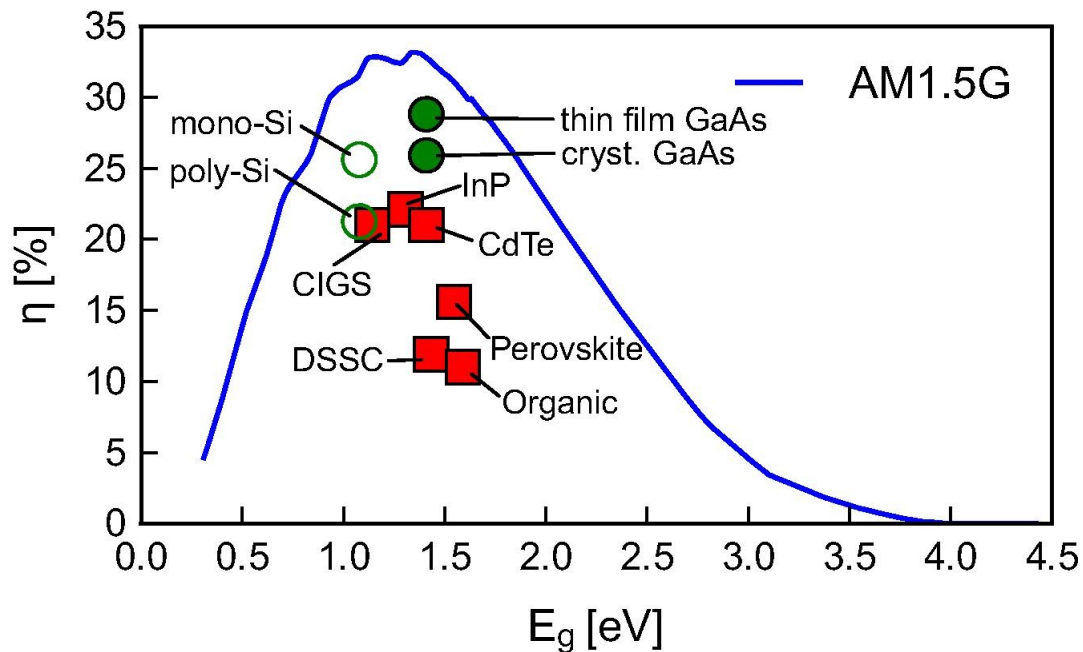


Figure 2.6: The Shockley-Queisser limit for a solar cell at 298.15 K. The efficiencies for energy conversion of different types of semiconductor are shown. Homo- and hetero-junctions are shown as green circles and red squares respectively, with indirect and direct band gaps shown as unfilled and filled symbols respectively. The AM1.5G refers to the spectral irradiance, corresponding to sunlight on the earth's surface which has been scattered by the atmosphere. Taken from [40]

in the field of photovoltaics focused on semiconductors with band gaps close to this optimum, which is why the first commercially used solar cells were silicon based, which has an energy gap of 1.1 eV. These first generation solar cells are still the

most widely used cells due to their high efficiency [41], and abundance of silicon. The cost of production of these first generation solar cells drove the development of second generation technologies, also known as thin-film solar cells. These solar cells are only a few micrometers thick and so are viable at a lower cost, although have a much lower efficiency [42] than first generation cells. The manufacturing problems associated with these second generation cells, such as availability or toxicity of materials, has led to the inspiration of third generation solar cells. Unlike the previous generations, which rely on a P-N junction design, these solar cells incorporate new materials into the semiconductor to make them more efficient by capturing a wider range of solar energy. One example of this is a dye-sensitised solar cell (DSSC), which are also referred to as the Grätzel cell, as they were invented in 1991 by Grätzel and O'Regan [43]. DSSCs consist of dye molecules attached to the surface of a nanocrystalline semiconductor film, with the photoexcitation of the dye molecule resulting in an electron transfer into the conduction band of the semiconductor. The dye molecule is then reduced by the electrolyte [44]. A scheme for this process is shown in figure 2.7.

2.7.3 How can the efficiency of solar cells be improved?

Although these DSSCs are comparatively low cost to make when compared to silicon based semiconductors, their current low efficiency means that there needs to be further development before they have commercial viability. Currently, the efficiency of DSSCs has reached 12% [46], which is far lower than first and second generation cells, where efficiencies of up to 46% have been achieved for a multi-junction first generation solar cell [47]. The theoretical efficiency of DSSCs has been shown to be over 20% [48], and therefore there has been extensive research over recent years to try and increase the efficiency of these cells. There are many factors when considering the efficiency of these cells, including the charge recombination rate, and subsequent dissipation of energy. One key step that determines

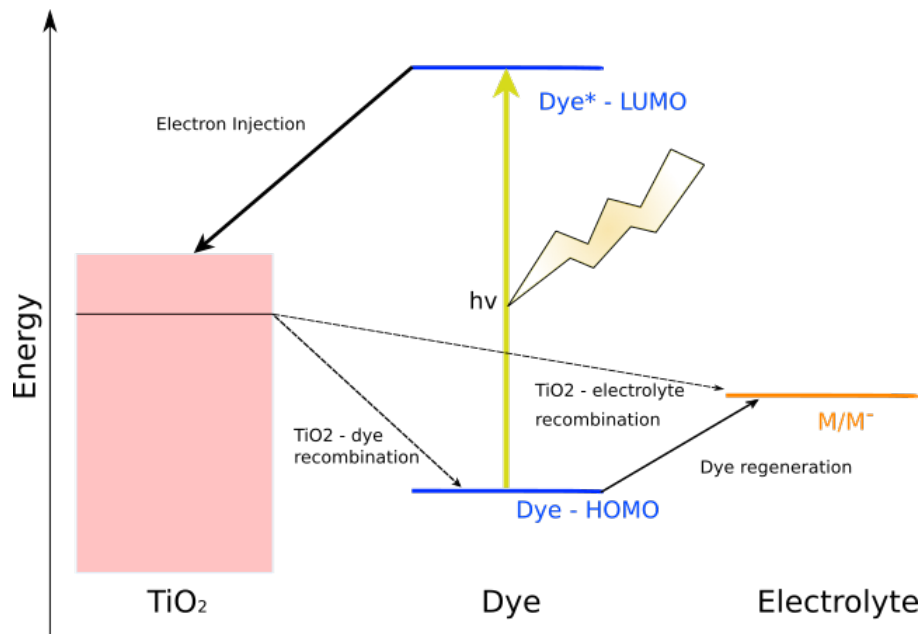


Figure 2.7: A schematic showing the energy levels and charge transfer in a DSSC, with TiO₂ as the semiconductor. Figure adapted from [45].

the efficiency is the initial electron injection process from the dye into the semiconductor, which is why it is this process that is the main focus of this thesis. This will be discussed further in chapter 5. By understanding this step in more detail, it opens the door for designing more efficient, and more commercially viable DSSCs.

Chapter 3

Methodology

3.1 Introduction

Development of methods based on the BOA to solve the time independent Schrödinger equation received much attention for many decades [49, 50, 51], but the thought of solving the time dependent Schrödinger equation was mostly ignored. Heller's seminal work in the 1970's on Gaussian wavepackets sparked the interest in finding solutions to the TDSE [52]. This paper led to a significant increase in popularity of finding numerically exact solutions to the nuclear wavefunction found in the TDSE and has led to wide breadth of methods by which this can be achieved. This equation mentioned in the previous chapter is repeated here,

$$i\hbar\dot{\Psi}(R, r, t) = \hat{H}\Psi(R, r, t). \quad (3.1)$$

The Hamiltonian operator, \hat{H} can be either in the diabatic or adiabatic form, as described in section 2.5. The Hamiltonian itself is split into a kinetic and potential operator acting upon the system.

Firstly, in order to determine the potential operator, or potential energy surfaces of the system (PES), the time independent Schrödinger equation, TISE must be solved for the electronic structure. Two main categories of these so-called *ab initio* methods are molecular orbital theory based wavefunction methods [53, 54, 55], and density functional theory based methods [56, 57]. These will be discussed

further in section 3.2.

The methods for which the TDSE can be solved also falls into two main categories, and depend on whether the nuclei are treated classically or as quantum particles [5], and are labelled as approximate methods or exact methods, respectively. In the classical approach, the particles in the system are treated as classical objects with classical trajectories and properties. Quantum mechanical approaches treat the nuclei as a wavefunction, instead of the classical particle, and propagate the nuclear wavefunction using a propagation scheme [58], and include all quantum effects. This wavefunction propagating over an electronic surface is called a wavepacket - a superposition of eigenstates. By representing the operator and expanding the nuclear wavefunction in a time independent product basis set, the TDSE can be solved using a variational principle. These exact quantum methods will be discussed in more detail in section 3.5.1. As previously mentioned, these exact methods represent the system as a wavefunction. However, if we want to move beyond this wavepacket picture, and represent an incoherent mixture of pure states in an exact manner which includes all quantum interferences, one must use density matrices. These density matrices allow environmental and thermal effects to be easily included in the quantum system. The derivation and dynamics of these density matrices, and their potential, will be discussed in section 3.6 and chapter 6, respectively.

3.2 Electronic Structure

For solving the TDSE, it is necessary to pre-compute the potential energy surfaces, PES, i.e. solve the TISE, as in the previous section shown in it's simplest form,

$$\hat{H}_{el}\Psi_{el} = E_{el}\Psi_{el}, \quad (3.2)$$

where the electronic Hamiltonian, under the BOA, can be written as follows

$$H_{el} = T_e(r) + V_{eN}(r, R) + V_{ee}(r) + V_{NN}(R) \quad (3.3)$$

where T_e is the electronic kinetic energy operator, and V_{eN} , V_{NN} and V_{ee} are the interactions for the electron-nuclei, nuclei-nuclei and electron-electron, respectively. The separation of nuclear and electronic motion under the BOA means the TISE can be solved at a specific nuclear configuration, R .

Determining E_{el} at different R configurations will give us the PES of the system of interest. This is achieved using electronic structure, or *ab initio*, methods. Two main categories of electronic structure methods that this thesis will cover are molecular orbital theory approaches [59], and density functional theory approaches [60].

3.3 Molecular Orbital Theory

For the methods discussed in this section, it is approximated that a system containing N -electrons can be expressed as a product of N one-electron basis functions called the Hartree product,

$$\Psi_{el}(x_1, \dots, x_N) = \psi_1(x_1)\psi_2(x_2) \dots \psi_N(x_N), \quad (3.4)$$

where Ψ_{el} is the total electronic wavefunction with spatial and spin coordinates (x_i) , where $(x_i) = (R, \omega_i)$. ψ_i is the one-electron wavefunction, or orbital, containing the i^{th} electron at coordinate x_i . However, this Hartree product fails to satisfy the antisymmetry principle. This antisymmetry principle states that electronic wavefunctions must be antisymmetric under the exchange of any 2 electrons,

$$\Psi(x_1, x_2) = -\Psi(x_2, x_1), \quad (3.5)$$

where this example is a wavefunction consisting of 2 electrons with spatial and spin coordinates of x_1 and x_2 . In this 2 electron example, the Hartree product can

be written for both electron configurations,

$$\Psi(x_1, x_2) = \psi_1(x_1)\psi_2(x_2), \quad (3.6)$$

$$\Psi(x_2, x_1) = \psi_1(x_2)\psi_2(x_1). \quad (3.7)$$

The problem can be clearly seen by the fact that $\Psi(x_1, x_2) \neq -\Psi(x_2, x_1)$. This failing of the antisymmetry principle is the core reasoning behind the development of Hartree-Fock, HF, theory.

3.3.1 Hartree Fock Theory

In order to satisfy the antisymmetry principle, Ψ_{el} can be written using a Slater determinant [53],

$$\Psi_{el}(x_1, \dots, x_N) = \frac{1}{\sqrt{N!}} \begin{vmatrix} \psi_1(x_1) & \psi_2(x_1) & \dots & \psi_N(x_1) \\ \psi_1(x_2) & \psi_2(x_2) & \dots & \psi_N(x_2) \\ \vdots & \vdots & \ddots & \vdots \\ \psi_1(x_N) & \psi_2(x_N) & \dots & \psi_N(x_N) \end{vmatrix}, \quad (3.8)$$

where $\psi_M(x_N)$ is the M^{th} single electron orbital containing the N^{th} electron. Therefore, one could write the previously mentioned 2 electron example system shown equation 3.5 as,

$$\Psi(x_1, x_2) = \frac{1}{\sqrt{2}} [\psi_1(x_1)\psi_2(x_2) - \psi_2(x_1)\psi_1(x_2)], \quad (3.9)$$

where $\psi_1(x_1)$ is electron 1 in spin orbital 1, and $\psi_2(x_1)$ is electron 1 in spin orbital 2, and so on.

The ground state energy of the system is given as,

$$E_{el} = \langle \Psi_{el} | \hat{H} | \Psi_{el} \rangle, \quad (3.10)$$

and corresponds to the lowest energy Slater determinant, where electron 1 occupies spin orbital 1, and electron 2 occupies spin orbital 2, and so on until the N^{th} electron occupies the N^{th} spin orbital, according to the Aufbau principle.

The electronic Hamiltonian,

$$\hat{H}_{el} = \sum_{i=1}^N -\frac{1}{2}\nabla_i^2 - \sum_{i=1}^N \sum_{A=1}^M \frac{z_A}{r_{iA}} + \sum_{i=1}^N \sum_{j=i+1}^N \frac{1}{r_{ij}}, \quad (3.11)$$

can be separated into the one-electron part - the kinetic energy and the Coulomb interactions of electrons with the nuclei - and the two-electron part, the electron-electron Coulomb interaction,

$$\hat{H}_{el} = \sum_{i=1}^N \hat{h}_1(x_i) + \sum_{i=1}^N \sum_{j=i+1}^N \frac{1}{r_{ij}}. \quad (3.12)$$

where $\sum_{i=1}^N \hat{h}_1(x_i)$ contains all the one-electron terms. The electron-electron Coulomb interaction cannot be exactly solved, and therefore one must resort to approximate methods.

The approximation that HF theory makes is to average the interaction of an electron with all other electrons by a mean field comprised of Coulomb and exchange terms. By representing the electron-electron interaction in this way, one arrives at the Hartree-Fock equation,

$$\hat{f}(x_1) = \hat{h}(x_1) + \hat{V}^{HF}(x_1), \quad (3.13)$$

where $\hat{f}(x_1)$ is the Fock operator, $\hat{h}(x_1)$ is the one-electron Hamiltonian described above, and \hat{V}^{HF} is the HF mean field operator. This mean field operator means that electron i feels the effect of all other $N - 1$ electrons. In the case of closed shell HF, this gives rise to the equation,

$$\hat{f}(r_1)\phi_i(r_1) = \epsilon_i\phi_i(r_1), \quad (3.14)$$

where the Fock operator is acting on spatial orbital ϕ_i with spatial coordinates r_1 to give the orbital energy, ϵ_i . This switch from spin to spatial orbitals arises due to separation of the spin orbital into its spin and spatial functions. As the one-electron Hamiltonian does not depend on spin, the spin functions can be factored out,

$$\langle \psi_i | \hat{h}(r_1) | \psi_j \rangle = \delta_{\sigma_i \sigma_j} (\phi_i | \hat{h}(r_1) | \phi_j) \quad (3.15)$$

where where the spin functions σ_i and σ_j are orthonormal and so reduce to a Kronecker delta function. The now spatial functions of the orbitals are represented in brackets, as opposed to the bra-ket notation, to represent that they are spatial coordinates. This switch from spin to spatial orbitals, and subsequent derivations, are well documented in literature [53, 54, 61].

Solving equation 3.14, however, is non-trivial for molecular systems. A procedure developed by Roothaan [62] suggests that this can be solved by expanding each orbital ϕ_i into a linear combination of atomic orbitals, φ_j , each with their own set of atomic orbital coefficients, c_{ji} , using a basis set comprising of K basis functions, (LCAO),

$$\phi_i = \sum_{j=1}^K c_{ji} \varphi_j. \quad (3.16)$$

This sum of atomic orbitals, or basis functions, makes up a basis set which describes molecular orbital ϕ_i .

The Roothaan equations provide a form for the wavefunction that can now be optimised by finding appropriate values for the LCAO expansion coefficients. This optimisation can be done by applying the variational principle to a trial wavefunction, $\tilde{\Psi}_{el}$. This ensures that the energy of this wavefunction must be greater than or equal to the exact ground state energy solution,

$$E = \frac{\langle \tilde{\Psi}_{el} | \hat{H}_{el} | \tilde{\Psi}_{el} \rangle}{\langle \tilde{\Psi}_{el} | \tilde{\Psi}_{el} \rangle} \geq E_{el}, \quad (3.17)$$

where the calculated energy, E is greater than or equal to the true ground state energy, E_{el} . By adjusting the initial guess wavefunction, and minimising equation 3.17 with respect to the choice of spin orbitals, the wavefunction with the lowest energy, and thus the most true, can be determined.

However, even if an infinite number of basis functions could be included, one would still not arrive at the exact wavefunction solution, as the lack of electron correlation is still present. This is the Hartree-Fock limit. In order for the exact wavefunction to be determined, one moves to the full configuration interaction (full CI) picture,

$$\Psi = C_0\phi_0 + \sum C_r\phi_a^r + \sum C_{r,s}\phi_{a,b}^{r,s} + \dots, \quad (3.18)$$

where the electron correlation is added to the HF Slater determinant, ϕ_0 , by including all the possible excitation determinants. These are the single excitation determinants, ϕ_a^r , double excitation determinants, $\phi_{a,b}^{r,s}$, and so on until all possible excitations are included. These determinants are called configuration state functions, CSFs.

An infinite number of basis functions to describe an infinite number of CSFs would allow the exact electronic wavefunction to be determined, and thus an exact solution of the TISE to be calculated, but this is clearly not possible for any systems bigger than diatomic molecules. Choosing the right basis set which sufficiently describes all the molecular orbitals in the system is key and requires both chemical knowledge and intuition.

As already mentioned at the beginning of this section, the Hartree-Fock approach assumes that the electrons in the system do not correlate with each other. This assumption becomes less and less valid as the size of the system, and thus

number of electrons, increases, and correlation effects become more prominent. Without accounting for these electron correlations, then the PES cannot be accurately calculated for anything but the simplest of systems. There are many methods which can correct for this missing correlation, and are termed post-HF methods. They will be briefly mentioned here, but not discussed in detail.

The Møller-Plesset perturbation theory partitions the electronic Hamiltonian into the Fock operator and a perturbation operator [63]. The complete active space self-consistent field method, CASSCF [55], divides the molecular orbitals into inactive and active orbitals. The active orbitals consist of a subset of the system's orbitals and electrons, whilst the inactive orbitals consist of the occupied core and the remaining unoccupied virtual orbitals. CASSCF then variationally solves the TISE for the active space orbitals, building configurations with all the possible electron excitations within the active space orbitals. This allows a complete set of Slater determinants for a truncated set of orbitals to be described accurately, effectively solving the electronic wavefunction exactly for a set of truncated orbitals. The active space of the CASSCF method consists of choosing which orbitals are most significant to the process of interest and requires careful consideration to ensure that the balance between accuracy and efficiency is achieved. Choosing a large number of orbitals to describe the system brings the method closer to the full configuration interaction method (full CI). Although this will give more accurate results, it is very inefficient.

One can also combine the two previously mentioned methods, termed the complete active space perturbation theory second order, CASPT2 [64]. This extension not only improves accuracy, but can also be used on excited states, unlike the MP2 method.

3.3.2 Electron Propagator Theory

The final method that will be discussed here can be used to calculate the energy of ionised states is electron propagator theory, EPT. This method is based on Koopman's theorem, which states that the ionisation energy is equal to the negative of the energy of the highest occupied molecular orbital (HOMO) [65].

EPT calculates the properties of cationic states from single-particle Green function equations. As only the HF orbitals of the ground state are required in building these Green functions, the wavefunction for the cationic state is not explicitly constructed. As the exact form of these one-particle Green functions are unknown, it is necessary to use a perturbation expansion on powers of the correlation potential. This correlation potential is contained within the self-energy matrix, $\Sigma(E)$. This gives rise to the eigenequation [66],

$$[\hat{F} + \Sigma(E)]\varphi_p(x) = \varepsilon_p\varphi_p(x). \quad (3.19)$$

where \hat{F} is the Fock operator acting on the eigenfunction Dyson orbital, $\varphi_p(x)$. The eigenvalue, ε_p is the ionisation potential [67]. This equation must be solved iteratively by adapting the self-energy matrix. Which perturbation order is used to approximate the ground state wavefunction determines what this is. A zeroth-order perturbation is equivalent to Koopman's ionisation potential. One perturbation function that will be used in this thesis is the Outer Valence Green's function (OVGF) - a so-called diagonal approach [68]. Diagonal approaches take the Dyson orbitals to be proportional to the HF orbitals, and thus any off-diagonal terms in the self-energy matrix are neglected [69]. OVGF includes 2nd and 3rd order perturbation terms, and has been shown to be a useful method for up-to medium sized molecules, with small relaxation effects.

3.4 Density Functional Theory, DFT

As discussed in the previous section, there are many complications associated with the molecular orbital based wavefunction approach to solving the TISE, namely how to account for the electron correlation interaction. The density functional approach replaces this electronic wavefunction with an electron density. Post-HF wavefunction methods become very computationally expensive for large systems, especially the size of systems that are the primary focus of this thesis, as each electron has the 4 coordinates of space and spin. DFT is efficient, simple and is easily combined with nuclear dynamics, with all the information of the system contained within the electron density, which can be described by a simple 3 coordinate function.

The central quantity in DFT is the density, not the wavefunction, where $\rho(r)$ is a functional of the wavefunction, Ψ ,

$$\rho[\Psi(r)] = N \int \cdots \int \Psi(r, x_2, \dots, x_N) \Psi^*(r, x_2, \dots, x_N) dx_2, \dots, dx_N, \quad (3.20)$$

where the electron density, $\rho(r)$, is the number of electrons per unit volume in a given state, and N is the total number of electrons.

The electron density offers all the necessary information needed for the Hamiltonian operator, which is the position and atomic charge of the nuclei, and the total number of electrons. The total number of electrons is obtained by integrating the density, ρ over all space,

$$N = \int \rho(r) dr. \quad (3.21)$$

The position of the nuclei is observed through the electron density maxima, and their atomic charge can be determined through calculating the rate of change in electron density with distance from the nuclei.

Underpinning DFT lies the Hohenberg-Kohn theorems [56]. The first of these states that the ground state electron density, $\rho_0(x_1, x_2, \dots, x_N)$, can uniquely determine the atomic positions, or the external potentials.

From this, one can write the density form of the energy as,

$$E_{el} = T_{el}[\rho(r)] + V_{el}[\rho(r)], \quad (3.22)$$

where T_{el} is the kinetic energy functional of the electrons, and V_{el} is a functional containing all the potential interactions,

$$V_{el}[\rho(r)] = V_{ee}[\rho(r)] + V_{Ne}[\rho(r)]. \quad (3.23)$$

However, there is no simple formalism to determine the density of a system. This leads on to the second theorem which states that DFT obeys the variational principle, and that by choosing different electron densities, those which produce the lower energy are the most correct.

The problem that arises from this now is that the form of these functionals shown above are largely unknown. Without knowing the exact forms of these functionals, applying a variational principle means that the resulting energy may be lower than the real energy of the system. It is for these reasons that a great deal of care must be taken using these methods. To determine the form of these functionals is the real difficulty in DFT.

The Kohn-Sham theory [60] considers a non-interacting reference system that has exactly the same electron density as the real, interacting electron system. The non-interacting electrons are described using a Slater determinant built using a single electron Hamiltonian, very similar to that of HF theory. Partitioning the electrons in this way, the overall energy of the system can now be expressed in terms of the independent particle kinetic energy, $T_s[\rho(r)]$, the Coulomb energy, $J[\rho(r)]$, and a new functional which contains all the unknown forms of electron interactions, $V_{xc}[\rho(r)]$, called the exchange correlation potential,

$$E[\rho] = T_s[\rho(r)] + J[\rho(r)] + V_{xc}[\rho(r)], \quad (3.24)$$

where $J[\rho(r)]$ contains the Coulombic interactions of $V_{ee}[\rho(r)] + V_{Ne}[\rho(r)]$. The exchange correlation potential makes up for all the errors introduced by the previously mentioned approximations, the assumption of non-interacting electrons and the over estimation of electron repulsion energy. DFT rests on finding the best approximation to this exchange correlation functional. Some methods that will be briefly mentioned here which can approximate this functional is the local density approximation (LDA), which approximates $V_{xc}[\rho(r)]$ as a uniform electron gas. This approximation works well for systems with slow changing electron densities, such as in bulk solids. An extension of this are generalised gradient approximation (GGA) functionals, which include the gradient of the electron density to allow for inhomogeneity of the electron gas. Commonly used GGA functionals include BLYP, and PBE, to name but a few. There are also hybrid functionals which combine HF and DFT approaches by replacing a portion of the electron density exchange correlation with a molecular orbital HF exchange energy. These hybrid functionals have had great success and are widely used, with B3LYP the perhaps most prolifically used.

These functionals are semi-empirical, and are all benchmarked against tests on small systems. This means that although DFT is formally exact, it is not technically an *ab initio* method in practice. In fact, HF theory can be thought of as an approximate theory with an exact solution, and DFT as an exact theory with approximate solutions.

3.5 Solving the time dependent Schrödinger equation for the nuclear wavefunction

Touched upon in the introduction of this chapter, solving the TDSE falls into two main categories, classical and quantum exact methods. The first full quantum mechanically exact simulation of the dynamics of a system was first introduced in 1969 [70], and then the development of grid-based methods such as the discrete variable representation (DVR) [57] and the fast-Fourier transform (FFT) [71] led to the efficient calculations known as the standard method.

However, the development of semi-classical methods for much larger systems, such as large biological systems involving environmental effects, have gained in popularity in recent years, such as exact factorisation [72, 73], where the nuclear wavefunction moves over a single time dependent energy surface, and path integral methods [74].

An early example of an approximate method is the Ehrenfest method, first put forward in 1927 [75]. This method describes the motion of the nuclear wavepacket using a classical trajectory using Newton's equations of motion, which evolves in time over a single, mean-field PES [76]. The single-configurational approach of this method means that it is not flexible enough to fully describe a quantum system [77]. Recently, the Ehrenfest approach has been adapted to the multi-configuration Ehrenfest (MCE) approach which aim to overcome the lack of correlations in quantum systems, potentially opening up this method to the study of quantum behaviour [78].

Another method which uses classical trajectories is Tully's trajectory surface hopping technique [79], which instead of using one point-like trajectory, uses a swarm of trajectories to describe the nuclear wavepacket, each behaving independently [24]. This method has been developed to include an algorithm in which the non-adiabatic coupling can induce hops between electronic surfaces, as well as

many other variants upon this surface hopping technique [80]. Just a few examples of surface hopping techniques with different switching mechanisms include fewest switches surface hopping (FSSH) [81] and more recently, fragment orbital-based surface hopping (FOB-SH) [82]. These surface hopping approaches have been shown to be extremely useful in the potential for, e.g. predicting charge transfers in large biological molecules [80].

As these approximate methods are able to treat systems with a larger number of DOF efficiently, and on much longer time-scales, they are crucial methods for simulating dynamics in systems such as protein biochemistry [83], or for systems involving many solvent molecules [84]. However, these trajectory methods break down when certain quantum effects come into play, such as decoherence and tunneling, and are not able to sufficiently describe such processes. There has been several advances in these methods to overcome such limitations, which starts to create a category of its own of semi-classical hybrid methods [85], such as quantum trajectory methods [86] and the emergence of Gaussian wavepacket approximations [87], where the wavepacket is constrained to a Gaussian function.

3.5.1 Multi-configuration time dependent Hartree method

Grid-based methods expand the wavepacket in a time independent product basis [88, 89]. Therefore the nuclear wavefunction with f degrees of freedom, for a particular electronic state, can be written as follows;

$$\Psi(q_1 \dots q_f, t) = \sum_{j_1=1}^{N_1} \dots \sum_{j_f=1}^{N_f} C_{j_1 \dots j_f}(t) \chi_{j_1}^1(q_1) \dots \chi_{j_f}^f(q_f), \quad (3.25)$$

where there are N_k time independent basis functions for the k^{th} degree of freedom (DOF) nuclear coordinates q_k . $C_{j_1 \dots j_f}$ are the time dependent expansion coefficients, for which the equations of motion can be derived, and solved, using the Dirac-Frenkel variational principle [90], in equation 3.26.

$$\langle \partial\Psi | \hat{H} - i\partial_t | \Psi \rangle = 0 \quad (3.26)$$

which, when using atomic units $\hbar = 1$. leads to,

$$i\frac{d}{dt}C_{j_1\dots j_f} = \sum_{\ell_1\dots\ell_f} \langle \chi_{j_1}^{(1)} \dots \chi_{j_f}^{(f)} | \hat{H} | \chi_{\ell_1}^{(1)} \dots \chi_{\ell_f}^{(f)} \rangle C_{\ell_1\dots\ell_f}. \quad (3.27)$$

These are the equations of motion (EOM) for the system [91]. Both the memory demand and computational time for this method increases exponentially with number of DOF, and becomes unfeasible for any systems with ≥ 4 DOF.

Due to this scaling issue, approximate methods must be employed to allow larger systems to be treated. The most easily implemented approximate method is the time dependent Hartree method (TDH), also referred to a the time dependent self-consistent field method (TDSCF). The TDH approach assumes the total wavefunction can be written as a Hartree product of one-dimensional, time dependent functions [92],

$$\Psi(q_1 \dots q_f) = a(t)\varphi^1(q_1, t) \dots \varphi^f(q_f, t). \quad (3.28)$$

As this is not a uniquely defined representation, the following constraints are enforced to derive unique EOM,

$$i \langle \varphi^k | \dot{\varphi}^k \rangle = g^k(t). \quad (3.29)$$

The constraint $g^k(t)$ is given a suitable value so that the EOM are derived using the Dirac-Frenkel variational principle for the coefficients and basis functions, shown below,

$$i\dot{a} = a \left(\langle H \rangle - \sum_{k=1}^f g^{(k)} \right), \quad (3.30)$$

$$i\dot{\varphi}^{(k)} = \mathcal{H}^{(k)}\varphi^{(k)} + (g^{(k)} - \langle H \rangle)\varphi^{(k)}, \quad (3.31)$$

where $\langle H \rangle$ is the expectation value of the Hamiltonian, and \mathcal{H} is the mean field operator. This method turns a f -dimensional problem into an f number of one-dimensional problems, simplifying the calculations and allowing systems of over 100 DOF to be treated.

As the TDH method is a mean-field method, the results are often poor [93]. This has led to improvements on this method by taking several configurations into account, giving rise to the blanket term of multi-configurational time dependent self-consistent field (MC-TDSCF) methods. These methods were pioneered in the 1980s by Kosloff et al [87] and Makri and Miller [94]. Arguably the most efficient of these methods to emerge is the multi-configurational time dependent Hartree method (MCTDH), first published by Meyer et al in 1990 [95].

The MCTDH approach expands the wavefunction of a given state where each DOF, f , in a system can be represented as a direct-product expansion of p sets of basis functions, $\varphi^{(p)}$, or single particle functions (SPFs),

$$\Psi(q_1 \dots q_p, t) = \sum_{j_1=1}^{n_1} \dots \sum_{j_p=1}^{n_p} A_{j_1 \dots j_p}(t) \prod_{k=1}^p \varphi_{j_k}^k(q_k, t), \quad (3.32)$$

where p is the number of DOF in the system, Ψ is the full nuclear wavefunction from the Born-Huang equation in the previous chapter, with nuclear coordinates q_p . A_{j_k} are the time dependent expansion coefficients, and $\varphi_{j_k}^k$ are the time dependent SPFs for the k^{th} DOF. Expanding the wavefunction in this way allows the results to be converged to the exact results by expanding the basis set. Equation 3.32 can be written more simply as components of the Hartree product and a composite of the expansion coefficients,

3.5 Solving the time dependent Schrödinger equation for the nuclear wavefunction

$$\Psi(q_1 \dots q_p, t) = \sum_J A_J \Phi_J, \quad (3.33)$$

where Φ_J is a p dimensional Hartree product of the SPFs, and A_J are the expansion coefficients. J is a multi-index subscript $J = j_1, \dots, j_p$.

The SPFs themselves are expanded as a linear combination of static primitive basis functions, with time independent coefficients. These static basis functions often take the form of a discrete variable representation, DVR. Applying the Dirac-Frenkel variational principle, equation 3.26, two coupled EOM can be derived from equation 3.33, one representing the coefficients,

$$i\dot{A}_J = \sum_L \langle \Phi_J | H | \Phi_L \rangle A_L, \quad (3.34)$$

where the Hamiltonian, H takes the diabatic form from equation 2.38 in the previous chapter. The EOM for the SPFs is as follows ,

$$i\dot{\varphi}_j^{(k)} = (1 - P^k) \sum_{k,l} \rho_{j,l}^k{}^{-1} \langle \hat{H} \rangle_{k,l}^k \varphi_l^k, \quad (3.35)$$

where P is the projection operator, defined as,

$$P^k = \sum_{j=1}^{n_k} |\varphi_j^k\rangle \langle \varphi_j^k|, \quad (3.36)$$

and $\rho_{j,l}^k$ is the density operator defined as,

$$\rho_{j,l}^k = \langle \Psi_j^k | \Psi_l^k \rangle, \quad (3.37)$$

where Ψ_j^k is a "single-hole" wavefunction and $\langle \Psi_j^k | \Psi_l^k \rangle$ is an integration over all the DOF except the k th. $\langle \hat{H} \rangle$ is the mean-field operator acting on the SPFs,

$$\langle \hat{H} \rangle_{jl}^k = \langle \Psi_j^k | \hat{H} | \Psi_l^k \rangle. \quad (3.38)$$

The algorithm for MCTDH can be used with many DOF, and with many sets of basis functions per DOF, allowing this method to range from the limiting case

of TDH, where $n_k = 1$ up to numerically exact standard method, where $n_k = N_k$ [93].

Although the MCTDH approach is able to treat larger systems when compared with the standard approach, it still has limitations in regards to memory and computational efficiency [91].

One way which this method can be adapted to help increase efficiency is mode combination. The SPFs do not need to consist of only 1 mode each, but one can group together several DOF into one combined mode, termed the multi-mode [96]. For example, the multi-mode Q may be an amalgamation of several modes,

$$Q = q_1 + q_2 + q_3 \dots \quad (3.39)$$

This multi-mode is then expanded in the normal MCTDH format.

Another method which has been developed to overcome the limitations of MCTDH is the multilayer-MCTDH (ML-MCTDH), which can expand one or several SPFs themselves in terms of another set of SPFs and so on [97, 98], and is a powerful extension of the MCTDH method. An example of a ML-MCTDH expansion is shown in the following set of equations, where nuclear wavefunction Ψ is expanded into a set of SPFs, φ . One of these SPFs is itself expanded into another set of SPFs, χ , one of which is expanded again into a set of SPFs, ϕ ,

$$\Psi(q_1 \dots q_p, t) = \sum_{j_1=1}^{n_1} \dots \sum_{j_p=1}^{n_p} A_{j_1 \dots j_p}(t) \prod_{k=1}^p \varphi_{j_k}^k(q_k, t), \quad (3.40)$$

$$\varphi(q_1 \dots q_p, t) = \sum_{j_1=1}^{n_1} \dots \sum_{j_p=1}^{n_p} B_{j_1 \dots j_p}(t) \prod_{k=1}^p \chi_{j_k}^k(q_k, t), \quad (3.41)$$

$$\chi(q_1 \dots q_p, t) = \sum_{j_1=1}^{n_1} \dots \sum_{j_p=1}^{n_p} C_{j_1 \dots j_p}(t) \prod_{k=1}^p \phi_{j_k}^k(q_k, t). \quad (3.42)$$

This gives rise to the possible corresponding ML-tree schematic shown below,

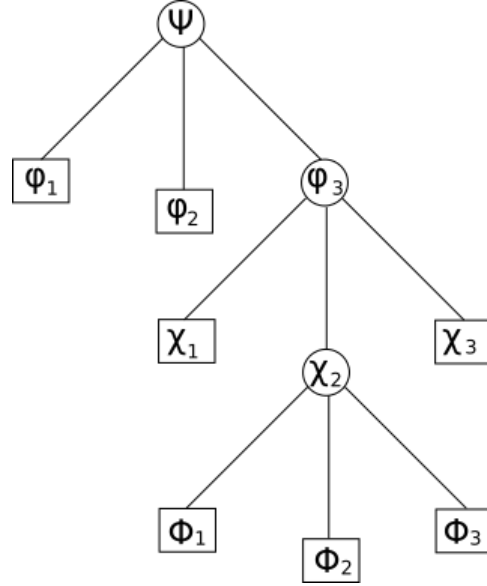


Figure 3.1: An example of a multi-layer tree structure

where each expansion (the circles on diagram 3.1) are called "nodes", with each node terminating in another node or the standard primitive basis expansion of the SPFs. Expressing the nuclear wavefunction in this layered way is very flexible, and can be many layers deep [99].

Within each layer of the tree, as in MCTDH, all coefficients and SPFs have their own EOM. The top layer EOM are identical to standard MCTDH - where the standard MCTDH can be thought of the special case where the ML tree consists of just one layer. In fact, the EOM for the SPFs are formally the same for all layers [100], shown in equation 3.35. The difference lies in the construction of the density matrix. For the ML-MCTDH approach it reads,

$$\rho_{ij}^{z,k_l} = \sum_{a,b=1}^{n_{k_{l-1}}^{z-1}} \rho_{ab}^{z-1,k_{l-1}} \sum_{J^{kl}} A_{a;J^{kl},i}^{z*} A_{b;J^{kl},j}^z, \quad (3.43)$$

where the reduced density matrix ρ_{ij}^{z,k_l} for node z and mode k_l requires the expansion of the coefficients for the current node as well as the layer above. The ML-MCTDH approach seems more complicated than standard MCTDH, and for

smaller systems it is much less efficient [99]. However, as the system size increases, the efficiency of propagating both the SPFs and their coefficients decreases using the standard MCTDH method. ML-MCTDH combines modes into smaller groups, now with a new layer of more manageable coefficients. Further reading on the intricacies of the EOM for the ML-MCTDH method is widely available in the literature, Wang et al [98, 100, 101], and Meyer et al [99, 102, 103, 104] in particular have well explained derivations.

The MCTDH equations shown in this section are general solutions to the TDSE. In order to make them applicable to molecular systems one needs a molecular Hamiltonian, comprising of the kinetic energy operators and the potential energy surfaces. In the work in this thesis, these PES are in the diabatic matrix form as described in chapter 2, section 2.5. Much of the computational cost of these grid-based calculations comes from the requirement of pre-calculating the PES of the system that is being probed. This process is a long, and often impossible process. Therefore, there will always be a numerical limitation to these grid-based methods. This has led to the development of direct dynamics, which calculates the PES on-the-fly [105]. By replacing the SPFs of MCTDH with multidimensional Gaussian functions, one can run dynamics and calculate the PES on-the-fly. Although the time taken to calculate the PES is side-stepped, for larger systems the effort needed to compute gradients and Hessians is not insignificant, and is often the bottle neck to these methods.

3.6 Density Matrices

As discussed in the previous section, a nuclear wavefunction can be expanded in terms of eigenfunctions. This wavefunction is represented by a pure state vector, or a quantum superposition of pure state vectors. In order to predict the final state of these systems after a chemical process has taken place, the initial state

must be known. However, if the initial state of a system is unknown, such as when the system is in thermal equilibrium, one can no longer express the system as a wavefunction. The system exists in a mixed state [106], and is represented by a density operator,

$$\rho = \sum_i P_i |\psi_i\rangle\langle\psi_i|, \quad (3.44)$$

where P_i is the probability that the system is in pure state ψ_i .

Representing the system using probabilities in this way allows environmental effects on the system dynamics to be included [107], meaning that open systems can be described using these density matrices. As mentioned in the previous chapter, 2.3, instead of solving the Schrödinger equation as one would for a pure state propagation, the time evolution of the density matrix is now represented as the following,

$$\begin{aligned} \dot{\rho} &= -i[H\rho - \rho H], \\ \dot{\rho} &= \mathcal{L}(\rho), \end{aligned} \quad (3.45)$$

where \mathcal{L} is the Liouvillian superoperator.

Within the MCTDH formalism, there are two formalisms of density matrices depending on the type of basic functions used- type I and type II [107, 108].

3.6.1 Type I Density matrix, ρ -MCTDH(I)

Type I density operators are analogous to the MCTDH scheme for wavefunction expansion, as in equation 3.32, but instead the density operator is expanded into single-particle density operators (SPDO),

$$\rho(Q_1, \dots, Q_f, Q'_1, \dots, Q'_f, t) = \sum_{\tau_1=1}^{n_1} \cdots \sum_{\tau_f=1}^{n_f} B_{\tau_1 \dots \tau_f}(t) \prod_{\kappa=1}^f \sigma_{\tau_\kappa}^{(\kappa)}(Q_\kappa, Q'_\kappa, t), \quad (3.46)$$

where $B_{\tau_1 \dots \tau_f}$ are the normal MCTDH expansion coefficients, and $\sigma_{\tau_\kappa}^{(\kappa)}$ are the SPDOs.

As a density operator is Hermitian, the B coefficients must be real and the SPDOs are also Hermitian. These properties are conserved throughout the propagation [91]. As with the standard wavefunction MCTDH, this representation is not unique and constraints are necessary to ensure orthonormality. Similar to the derivation of the EOM for MCTDH, equations 3.36, 3.37 and 3.38, if the MCTDH density matrix is defined as,

$$\mathcal{D}_{\mu\nu}^k = \sum_{\tau} B_{\tau\mu}^* B_{\tau\nu}^k, \quad (3.47)$$

note the change in notation for this density matrix from that of the MCTDH case, so as to avoid confusion. The projector operator is defined as,

$$P^k = \sum_{\nu=1}^{n_k} |\sigma_{\nu}^k\rangle\rangle\langle\langle\sigma_{\nu}^k|, \quad (3.48)$$

and the mean field Liouvillian superoperator is defined as,

$$\langle\langle\mathcal{L} - \mathcal{G}\rangle\rangle_{\mu\nu}^k = \langle\langle\Pi_{\mu}^k|(\mathcal{L} - \mathcal{G})\Pi_{\nu}^k\rangle\rangle, \quad (3.49)$$

where \mathcal{G} contain the aforementioned constraints on the system. The double brackets in the above equations refer to the differences in this approach to the standard wavefunction approach. The integration takes place in Liouville space, rather than the Hilbert space, taking the trace of the product of matrices rather than a vector product.

Given these definitions, the EOM for coefficients, and the SPDOs, of the Type I density matrix operator can be defined as [107],

$$i\dot{B}_{\tau} = \sum_{\tau'} \langle\langle\Omega_{\tau}|(\mathcal{L} - \mathcal{G})\Omega_{\tau'}\rangle\rangle B_{\tau'} \quad (3.50)$$

where Ω_{τ} is the Hartree product of the SPDOs. The SPDOs EOM,

$$i\dot{\sigma}^k = \mathcal{G}^k \sigma^k + (1 - P^k)(\mathcal{D}^k)^{-1} \langle\langle\mathcal{L} - \mathcal{G}\rangle\rangle^k \sigma^k. \quad (3.51)$$

The computational effort for this type I formalism lies in the number of SPDOs.

3.6.2 Type II density matrix, ρ -MCTDH(II)

These SPDOs can be further expanded using SPFs as used in the MCTDH method for wavefunctions,

$$\rho(Q_1, \dots, Q_f, Q'_1, \dots, Q'_f, t) = \sum_{\tau_1=1}^{n_1} \cdots \sum_{\tau_f=1}^{n_f} B_{\tau_1 \dots \tau_f}(t) \prod_{\kappa=1}^f |\psi_{j_\kappa}^{(\kappa)}(Q_\kappa, t)\rangle \langle \psi_{l_\kappa}^{(\kappa)}(Q'_\kappa, t)|. \quad (3.52)$$

This is known as the type II density operator. The EOM for the coefficients for the Type II density matrices is as follows [107],

$$i\dot{B}_{J,L} = \langle \Phi_J | (\mathcal{L} - \mathcal{G})(\rho) | \Phi_L \rangle, \quad (3.53)$$

and for the SPFs of the density matrix,

$$i\dot{\psi}^k = g^k \varphi^k + (1 - P^k) Tr\{(\mathcal{L} - \mathcal{G})(\rho)\rho\}_k (\mathcal{D}^{2,k})^{-1} \varphi^k, \quad (3.54)$$

where \mathcal{D} is the single particle reduced density matrix. The computational effort scales in this formalism with the coefficients.

As a consequence of adhering to the Dirac-Frenkel variational principle, the MCTDH wavefunction conserves both total probability and energy. However, these quantities are not conserved for density matrices, although the energy becomes increasingly preserved with convergence.

An exciting development of this method is using the ML-MCTDH formalism of the density matrix, ρ -ML-MCTDH, as there is very little, if any, data published using this method. The ρ -ML-MCTDH method is analogous to the ρ -MCTDH, as the ML-MCTDH is to the MCTDH method. The SPDOs which the full wavefunction can be expanded into in the ρ -MCTDH approach, equation 3.46 in this section, can be further expanded upon as in the ML-MCTDH expansion. These

have analogous EOM as the ML-MCTDH SPFs and coefficients, but the Hamiltonian operator is replaced with the Liouvillian operator. This novel technique can open the door to treating larger systems in an exact way, whilst also including temperature and solvent effects.

Chapter 4

Allene

4.1 Introduction

Allene, C_3H_4 , is an interesting molecule as it is the smallest in the cummulene series, as well as having D_{2d} symmetry. As mentioned briefly in 2.6, when in the radical cationic form it exhibits an $E \otimes b$ Jahn-Teller conical intersection, where the doubly degenerate ground state can couple to vibrational modes with symmetry b . This doubly degenerate electronic state arises due to the possibility of the positive charge lying at either end of the molecule, figure 4.1. It therefore provides a suitable challenge to simulate a electron transfer process, with the added challenge that the conical intersection is directly at the Franck-Condon point. This means that there is strong vibronic coupling immediately after ionisation [109].

Using the data published in Woywod and Domcke’s paper [35] as an initial reference for a comparison to the experimental data, this chapter will analyse the dynamics of the allene molecule, after removing an electron, using the vibronic Hamiltonian coupled with Multi-Layer Multi-Congurational Time Dependent Hartree method, ML-MCTDH. The ground state configuration of allene is as follows (ignoring the core-shell),

$$(3a_1)^2(2b_2)^2(4a_1)^2(3b_2)^2(1e)^4(2e)^4$$

Removing an electron from the HOMO results in the double degenerate ground

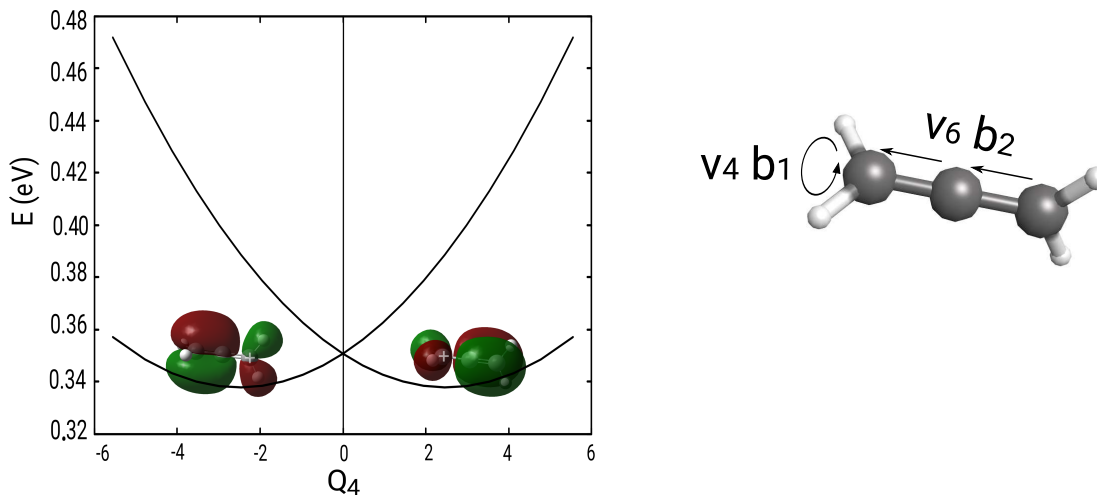


Figure 4.1: On the left: The PES of the diabatic ground state along normal mode 4. This curve was obtained from a Taylor expansion around the neutral ground state of allene, at $Q=0$. Mode 4 corresponds to the torsional mode of b_1 symmetry. This is the mode that drives the charge transfer along the molecule. On the right: The allene molecule showing the two most significant vibrational modes, ν_4 and ν_6 , of b_1 and b_2 symmetry. These correspond to the torsional mode and the asymmetric stretch, respectively.

state of the cation, the \tilde{X}^2E state, whose main progression in the photoelectron spectrum arises due to the torsional mode, ν_4 .

A vibronic coupling Hamiltonian was set up, incorporating up to second order coupling terms in order to reproduce the experimental photoelectron spectrum. This Hamiltonian is constructed in a basis of diabatic states, meaning that the Hamiltonian may be written as,

$$\mathbf{H} = \mathbf{T}_N \mathbf{1} + \mathbf{W}, \quad (4.1)$$

where $\mathbf{T}_N \mathbf{1}$ is the kinetic energy operator acting on the identity matrix. This operator uses mass-frequency scaled normal coordinates, and the kinetic energy operator takes the following form,

$$T_N = -\frac{\omega}{2} \frac{\partial^2}{\partial Q^2}, \quad (4.2)$$

where Q is the normal mode, with corresponding frequency ω . \mathbf{W} is a Taylor

series of diabatic potentials of coupling matrices expanded around the equilibrium geometry of the ground state of neutral allene,

$$\mathbf{W} = \mathbf{W}_{ij}^{(0)} + \mathbf{W}_{ij}^{(1)} + \mathbf{W}_{ij}^{(2)} + \dots \quad (4.3)$$

The zeroth-order potential energy matrix can be expressed as the simple harmonic approximation of the ground state potential energy surface (PES) of neutral allene. This term is on-diagonal, and is expressed,

$$\mathbf{W}_{ii}^{(0)} = \sum_{\alpha} \frac{1}{2} \omega_{\alpha} Q_{\alpha}^2 + E^{(i)}, \quad (4.4)$$

where $E^{(i)}$ is the energy of state, i , with the vibrational frequency, ω_{α} of the mass-frequency scaled normal mode Q_{α} . In the 2 state cationic allene model, $E^{(1)} = E^{(2)}$ and is the vertical ionisation energy.

The first-order linear coupling elements are written as,

$$\mathbf{W}_{ii}^{(1)} = \sum_{\alpha} \kappa_{\alpha}^i Q_{\alpha}, \quad (4.5)$$

$$\mathbf{W}_{ij}^{(1)} = \sum_{\alpha} \lambda_{\alpha}^{ij} Q_{\alpha}, \quad (4.6)$$

where κ_{α}^i and λ_{α}^{ij} are the first derivatives with respect to the coordinates, either on-diagonal or off-diagonal respectively. These are defined as,

$$\kappa_{\alpha}^i = \frac{\partial}{\partial Q_{\alpha}} \langle \phi_i | H_{el} | \phi_i \rangle = \frac{\partial V_i}{\partial Q_{\alpha}}, \quad (4.7)$$

$$\lambda_{\alpha}^{ij} = \frac{\partial}{\partial Q_{\alpha}} \langle \phi_j | H_{el} | \phi_i \rangle, \quad (4.8)$$

where ϕ are the diabatic electronic states obtained from the transformation from adiabatic to diabatic states described in chapter 2, and λ_{ij} is the off-diagonal, non-adiabatic coupling between diabatic states ϕ_i and ϕ_j . These terms are only non-zero if certain symmetry requirements are met. As the ground state of allene in

the cationic radical form is of the 2E type, the direct product of this representation is,

$$[E \times E] = A_1 + B_1 + B_2. \quad (4.9)$$

D_{2d}	A_1	A_2	B_1	B_2	E
A_1	A_1	A_2	B_1	B_2	E
A_2	A_2	A_1	B_2	B_1	E
B_1	B_1	B_2	A_1	A_2	E
B_2	B_2	B_1	A_2	A_1	E
E	E	E	E	E	$A_1 + [A_2] + B_1 + B_2$

Table 4.1: The irreducible representation product table for D_{2d} symmetry

For vibrational mode, α , to linearly couple the electronic states, i and j , the condition $\Gamma_i \otimes \Gamma_j \otimes \Gamma_\alpha \subset A_1$ must be satisfied. Therefore, it is clear from the direct product, equation 4.9, and the product table, table 4.1, that only modes of A_1 , B_1 and B_2 symmetry have non-zero linear coupling elements, with the torsional B_1 mode on the off-diagonal.

Allene, C_3H_4 , has 15 normal modes which have the following irreducible representation:

$$\Gamma = 3A_1 + B_1 + 3B_2 + 4E \quad (4.10)$$

In the linear vibronic coupling model, therefore, it can be seen that there are three A_1 and B_2 modes which contribute a linear coupling parameter and one B_1 mode. The symmetry of the Jahn-Teller problem means that for A_1 modes, $\kappa^1 = \kappa^2$, while for b_2 modes, $\kappa^1 = -\kappa^2$ [5]. The overall Hamiltonian using first order coupling is constructed in full,

$$\mathbf{H} = \sum_{i=1}^{15} \frac{\omega_i}{2} \left(-\frac{\partial^2}{\partial Q_i^2} + Q_i^2 \right) \mathbf{1} + \begin{bmatrix} E_E & 0 \\ 0 & E_E \end{bmatrix} + \begin{bmatrix} \sum_{i=1}^3 \kappa_i Q_i + \sum_{i=5}^7 \kappa_i Q_i & \lambda_4 Q_4 \\ \lambda_4 Q_4 & \sum_{i=1}^3 \kappa_i Q_i - \sum_{i=5}^7 \kappa_i Q_i \end{bmatrix}, \quad (4.11)$$

where the modes refer to the labels given in table 4.2. This is the first order coupling, as it only takes into account the modes which couple most strongly, i.e. a linear Q term.

The parameters for this Hamiltonian were determined using VCHam program—the Vibronic Coupling HAMiltonian package implemented within the Quantics software. This program fits a polynomial to the *ab initio* data points, and these polynomial fittings give the parameters for the Hamiltonian, where the linear coefficients for the polynomials give the λ/κ values, the second order coefficients give γ parameters, and so on and so forth. For fitting the PES for allene, up to fourth order terms have been included. This is discussed more in the next section.

4.2 Electronic Structure Calculations

4.2.1 Vibrational Mode Analysis

Firstly, a geometry optimisation of the ground state of the neutral allene molecule was performed using Møller-Plesset second order perturbation theory (MP2), with a Pople basis set of 6-31G(d). Following this, a vibrational analysis of the molecule was performed using MP2, with a basis set of 6-311++G(2d,2p). These frequencies are calculated by determining the second derivatives of the energy with respect to the nuclear coordinates. These results are listed in table 4.2, and are compared to the experimental results reported by Mahapatra et al, [33].

In order to calculate the coupling constants, i.e. the κ and λ values, the VCHam

Mode Label	Symmetry	Description	ω (eV)	ω Expt. (eV) [33]	Deviation
ν_1	A ₁	in-sync HCH sym. stretch	0.39796	0.3738	+6.46%
ν_2	A ₁	in-sync HCH bend	0.18687	0.1789	+4.46%
ν_3	A ₁	CCC sym. stretch	0.13966	0.1330	+5.01%
ν_4	B ₁	Torsion	0.10974	0.1072	+2.37%
ν_5	B ₂	out-of-sync sym. HCH stretch	0.39794	0.4224	-5.79%
ν_6	B ₂	CCC asym. stretch	0.26051	0.2426	+7.38%
ν_7	B ₂	out-of-sync HCH bend	0.17960	0.1733	+3.64%
ν_8	E	HCH asym. stretch	0.40902	0.4322	-5.36%
ν_9	E	in-plane HCH wag	0.12638	0.1238	-1.85%
ν_{10}	E	out-of-plane HCH wag	0.10296	0.1043	-1.28%
ν_{11}	E	CCC bend	0.03795	0.0440	-13.75%

Table 4.2: Vibrational frequencies of normal modes of ground state neutral allene taken with MP2/6-311++G(2d,2p) level of theory. All vibrations were calculated using Gaussian 09 program.

program was used to fit the potential energy surfaces, which were calculated using both Electron Propagator Theory (EPT) and the Complete Active Space SCF method, CASSCF, using a (3,4) active space. This active space means that there were 3 electrons in 4 active orbitals. This configuration is shown in figure 4.2. This

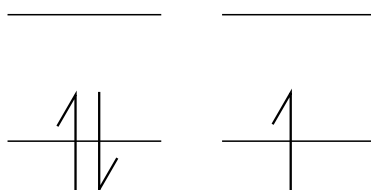


Figure 4.2: The (3,4) active space of allene. It consists of the occupied degenerate HOMO π orbitals, and the unoccupied degenerate LUMO π^* orbitals.

active space was chosen as previous work [110] had shown that a (3,2) active space for allene produced good results, and using a (3,4) active space seemed chemically sensible as it included the additional 2 π^* valence orbitals in the active space.

The results of the ionisation potentials calculated for each of these methods is shown in table 4.3.

Method	Vertical Ionisation potential (eV)
EPT	10.184
CASSCF	8.233
Experiment [111]	10.305

Table 4.3: The ionisation potentials for allene calculated using EPT and CAS(3,4) compared to the experimental values

It is clear from the results of this that the EPT method to calculate the ionisation potential is much more accurate than the CASSCF method. Therefore, the calculations in this chapter were continued using the results obtained using the EPT method, and a more thorough mapping of the CAS active space was deemed unnecessary.

In order to calculate the diabatic surfaces of allene, the software VCHam implemented in Quantics was used. The VCHam program works by deriving a realistic model of the vibronically coupled Hamiltonian when given a set of *ab initio* data points of the PES surfaces of interest at a given geometry along nuclear coordinate, Q . Using a least squares fit algorithm using a conjugate gradient optimisation scheme, each parameter is optimised. This approach allows fully parameterized models to be generated easily. The linear coupling constants are determined initially by finding the gradient of the potential energy surface following a displacement from the neutral ground state geometry, Q_0 . The higher order coupling parameters are built upon this. The parameterized surfaces calculated are shown in the diagram in figure 4.3.

The A_1 symmetry v_1 and v_3 modes were best represented as Morse potentials:

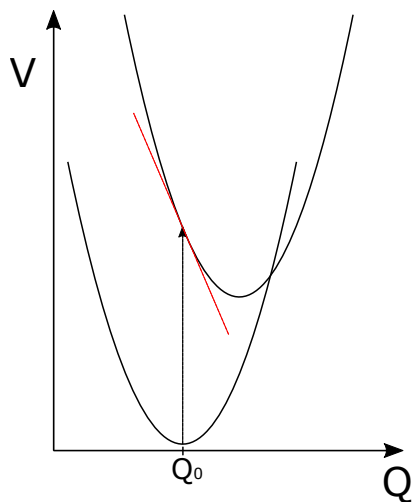


Figure 4.3: A sketch of a PES along some normal mode, Q , to show how kappa values are calculated for each normal mode

to be expected from a symmetric stretch mode. This Morse potential is of the form,

$$V = D_0(1 - e^{-\alpha(Q-Q_0)})^2 + E_0, \quad (4.12)$$

The remaining modes were described using either simple quadratic harmonic potentials or quartic harmonic potentials of the form,

$$V = \frac{1}{24}\epsilon Q^4 + \frac{1}{2}\gamma Q^2 + \kappa Q + \frac{1}{2}\omega Q^2, \quad (4.13)$$

where the second quadratic term, $\frac{1}{2}\omega Q^2$, is simply the harmonic frequency of the neutral ground state. The energy surfaces of each mode can be seen in figure 4.4, with all the fitting parameters given in table 4.4. Since the e modes do not couple on the first order, and therefore the plots do not give significant insight, they have been omitted from figure 4.4.

A list of the calculated coupling constants for the \tilde{X}^2E state of the allene radical cation can be seen in table 4.5. The coupling strength, κ/ω or λ/ω , factor in the vibration of the mode and therefore gives a true assessment on how displaced

Harmonic Oscillator Potentials						
Symmetry	Mode	Frequency	State	κ	γ	ϵ
a ₁	2	0.1868	1,2	-0.0500	0.0013	0.0001
b ₁	4	0.1097	1,2	± 0.2819	0.0389	0.0105
b ₂	5	0.3979	1	0.0287	0.0047	0.0320
			2	-0.0027	0.0047	0.0470
b ₂	6	0.2605	1,2	± 0.3129	-	-
b ₂	7	0.1796	1,2	± 0.0124	-	-
e	8	0.4090	1	-	0.1133	0.6918
			2	-	0.1107	0.0687
e	9	0.0.1264	1	-	0.0380	-
			2	-	-0.0218	-
e	10	0.1030	1	-	0.1198	-
			2	-	0.0766	-
e	11	0.0379	1	-	0.0400	0.0144
			2	-	0.0328	0.0171

Morse Potentials						
Symmetry	Mode	State	D_0	α	Q_0	E_0
a ₁	1	1	29.174	0.0853	0.1888	-0.0077
		2	26.659	0.0892	0.1888	-0.0077
a ₁	3	1,2	39.711	0.0423	0.3757	-0.0102

Table 4.4: A table showing all the fitting parameters of the polynomials used to fit against the *ab initio* points calculated in VCHam using EPT.

the mode is, and thus how significant it is to the process of interest. For determining the coupling strength of the Morse potential modes, ν_1 and ν_3 , they were approximated to a harmonic oscillator to obtain the κ values.

Mode	Frequency (eV)	κ/λ (eV)	κ/ω or λ/ω
$\nu_1(a_1)$	0.3979	-0.0827	0.2078
$\nu_2(a_1)$	0.1868	-0.0500	0.2676
$\nu_3(a_1)$	0.1396	-0.0689	0.4935
$\nu_4(b_1)$	0.1097	0.2819	2.2306
$\nu_5(b_2)$	0.3979	± 0.0287	0.0721
$\nu_6(b_2)$	0.2605	± 0.3129	1.2011
$\nu_7(b_2)$	0.1796	± 0.0124	0.0690

Table 4.5: The calculated coupling constants for the \tilde{X}^2E state of allene radical cation, where the off-diagonal λ value refers to the ν_4 mode. The identical frequency of modes ν_1 and ν_5 is purely coincidental.

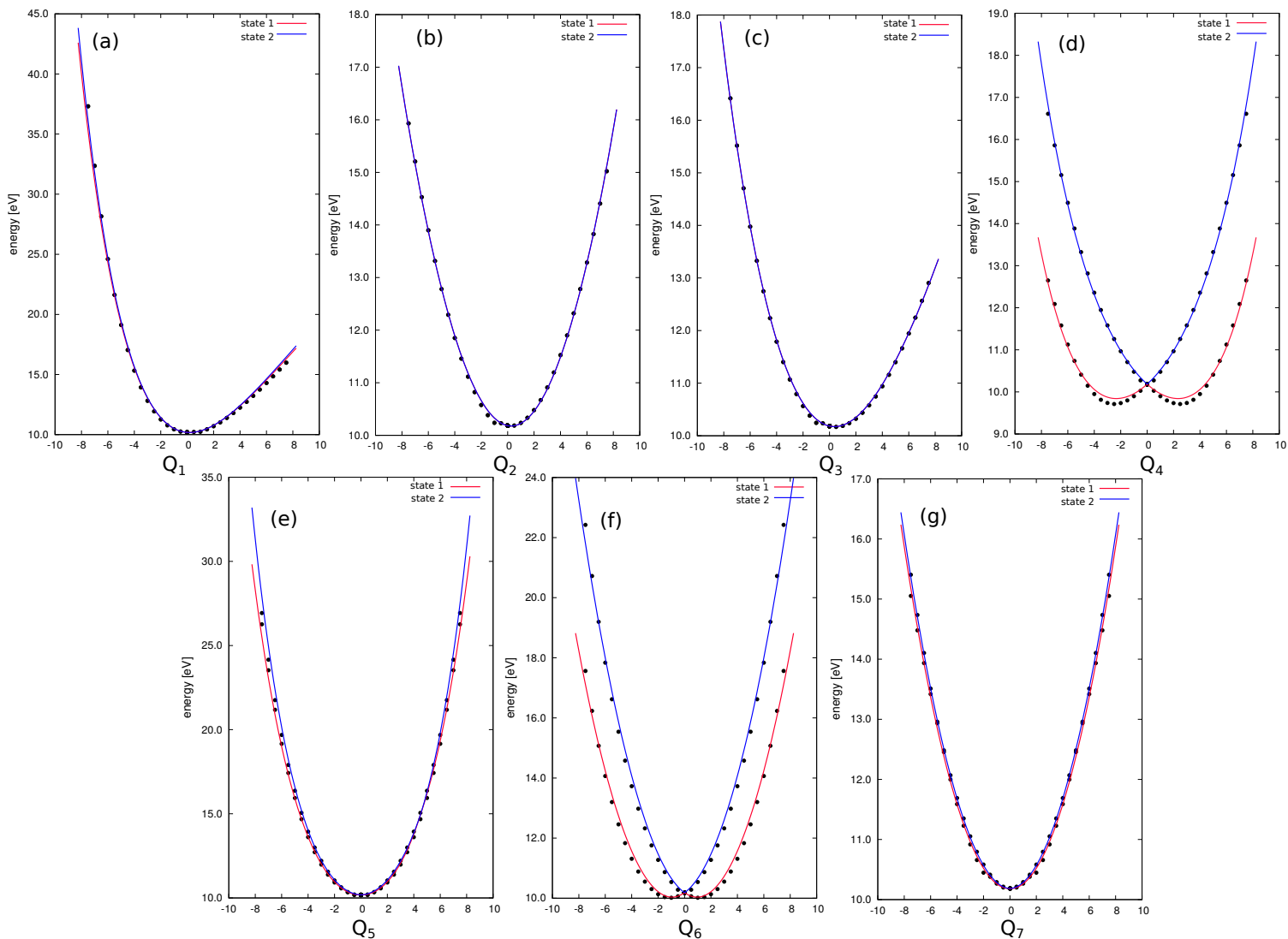


Figure 4.4: The calculated adiabatic \tilde{X}^2E state along the dimensionless nuclear coordinate, Q , of (a) ν_1 , (b) ν_2 , (c) ν_3 , (d) ν_4 , (e) ν_5 , (f) ν_6 , and (g) ν_7 modes, calculated using EPT, and fitted using VCHam.

It can be seen from table 4.5 and the plots in figure 4.4, that modes ν_4 and ν_6 , the torsional mode and C-C anti symmetric stretch respectively, are strongly Jahn-Teller active in this state and both lead to a large splitting of this degenerate ground state. Upon calculating the spectrum, it was discovered that it is essential to include the ν_3 mode to get full detail in the spectrum. This is not unexpected, given the relatively high coupling parameter of ν_3 .

The parameters of these 2 most significant modes were also calculated using the CASSCF results, as a comparison. The table of parameters and the plots of

Method	Mode	κ	γ	ϵ
EPT	ν_4	0.2819	0.0389	0.0105
	ν_6	0.3129	-	-
CASSCF	ν_4	0.2882	0.0122	0.0169
	ν_6	0.3108	0.0396	-

Table 4.6: A table showing the fitting parameters of the polynomials for the significant ν_4 and ν_6 modes used to fit against the *ab initio* points calculated in VCHam using CASSCF.

modes ν_4 and ν_6 are shown in table 4.6 and figure 4.5, respectively.

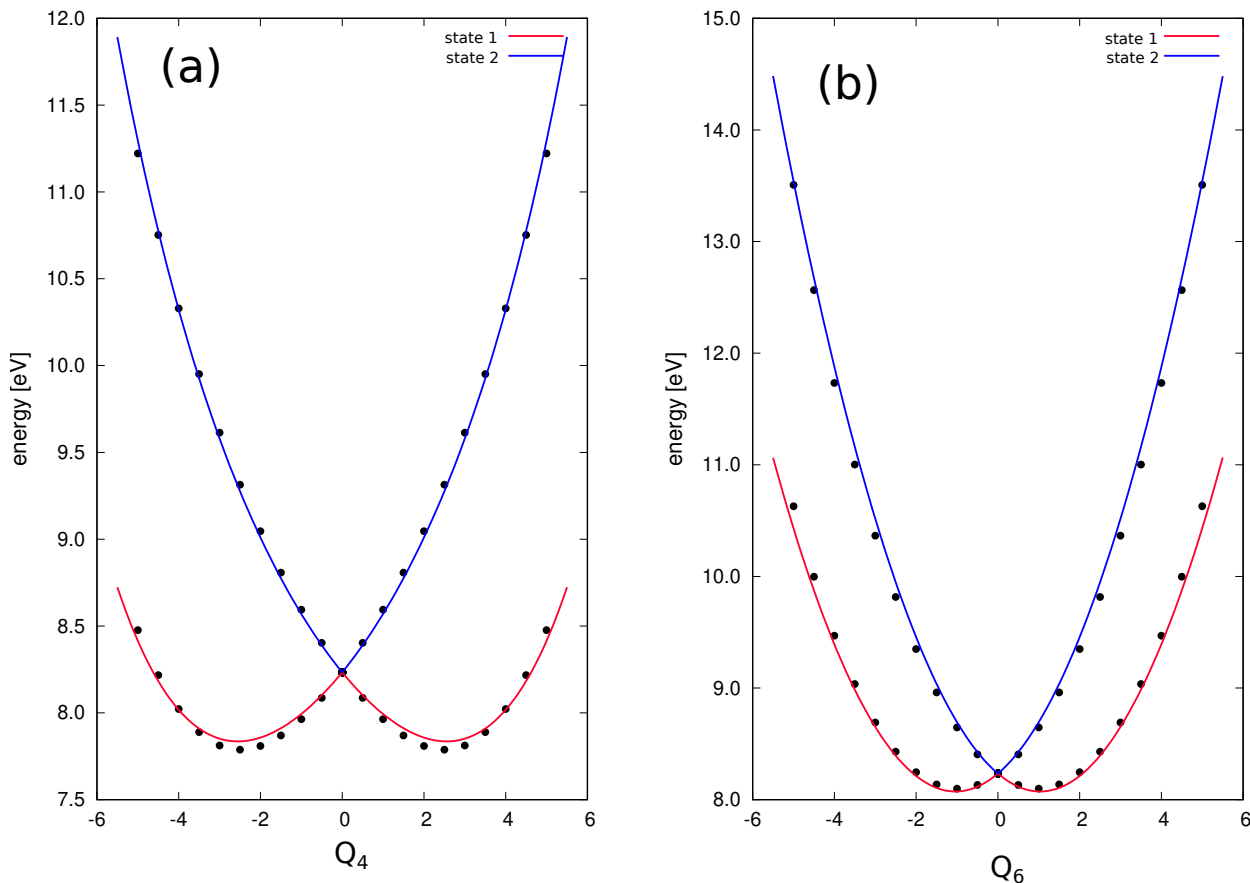


Figure 4.5: The calculated adiabatic \tilde{X}^2E state along the significant (a) ν_4 and (b) ν_6 modes, calculated using CASSCF, and fitted using VCHam.

Despite the incorrect energy determination of the CASSCF method, the overall PES of the significant modes look very similar. This can be verified by looking

at the close polynomial fitting parameters in table 4.6. The similarity in the PES calculated using the two different methods allows us to have confidence that EPT has correctly calculated the PES of the system.

4.3 Calculating the Spectrum

4.3.1 The Theory

The quantum dynamics were performed using the Quantics software package [112], which uses a wavepacket propagation using the MCTDH method. All 15 normal modes were included in the final calculation, but the first step was to test the limits of the standard MCTDH method. A simple 3 mode calculation, which included ν_4 , ν_6 and ν_3 , was performed. The number of SPFs and primitive basis functions for each of these modes are shown in table 4.7.

Mode	Number of SPFs	Primitive basis functions
$\nu_3(A_1)$	16	21
$\nu_4(B_1)$	12	43
$\nu_6(B_2)$	12	15

Table 4.7: Number of SPFs and primitive basis functions for the modes involved in a 3d calculation for Allene

The set of primitive basis functions in which the single particle functions can be represented was chosen to be a harmonic oscillator DVR.

To first test the limits of the MCTDH method, the full system was reduced to 7 modes, which served as a good intermediary between what MCTDH can feasibly do and an easy test for the ML-MCTDH. This includes all the modes with a linear coupling parameter, κ . These were described using the combination modes shown in table 4.8, along with the number of SPFs required for convergence. Convergence was judged by looking at the natural orbital populations at the end of the propagation which should ideally be $<10^{-3}$, as well as if the spectra changed significantly by adding more SPFs.

Mode	Number of SPFs
$Q_1(\nu_4+\nu_6)$	14
ν_3	12
$Q_3(\nu_7+\nu_5)$	12
$Q_4(\nu_1+\nu_2)$	12

Table 4.8: The number of SPFs used for the modes involved in a 7d calculation for Allene

As the full system consists of 15 modes, in order to calculate the spectrum of this full system it was necessary to use the multilayer approach, as discussed in section 3.5.

The multilayer approach (ML-MCTDH) is a hierarchical form of the wavefunction used from the standard MCTDH [113], and is highly flexible and can be applied to systems with many 100s of atoms. For a quick summary, ML-MCTDH works off the premise that the basis functions, or single particle functions (SPFs), that the nuclear wavefunction can be expanded into, using the standard MCTDH method, can themselves be expanded further into another set of SPFs, which may also be further expanded, and so on and so forth,

$$\begin{aligned}
\Psi(Q_1 \dots Q_p, t) &= \sum_{j_1=1}^{n_1} \dots \sum_{j_p=1}^{n_p} A_{j_1 \dots j_p}^1(t) \underbrace{\varphi_{j_1}^1(Q_1, t)} \dots \varphi_{j_p}^p(Q_p, t), \\
\varphi(Q_1 \dots Q_\kappa, t) &= \sum_{j_1=1}^{n_1} \dots \sum_{j_\kappa=1}^{n_\kappa} A_{j_1 \dots j_\kappa}^2(t) \underbrace{\chi_{j_1}^1(Q_1, t)} \dots \chi_{j_\kappa}^\kappa(Q_\kappa, t), \\
\chi(Q_1 \dots Q_f, t) &= \dots
\end{aligned} \tag{4.14}$$

Through these expansions, the result can be expressed as a tree diagram (ML-tree) to conveniently illustrate the structure of the wavefunction. The ML-tree used for the final calculations performed on allene is shown in figure 4.6, showing the number of basis functions for each branch of the tree required.

The groupings chosen for the calculation were based on the strength of the coupling constants, and how significant they are in predicting the spectrum. The ν_4 , ν_6 and ν_3 were most important, necessary in fact, in predicting the spectrum

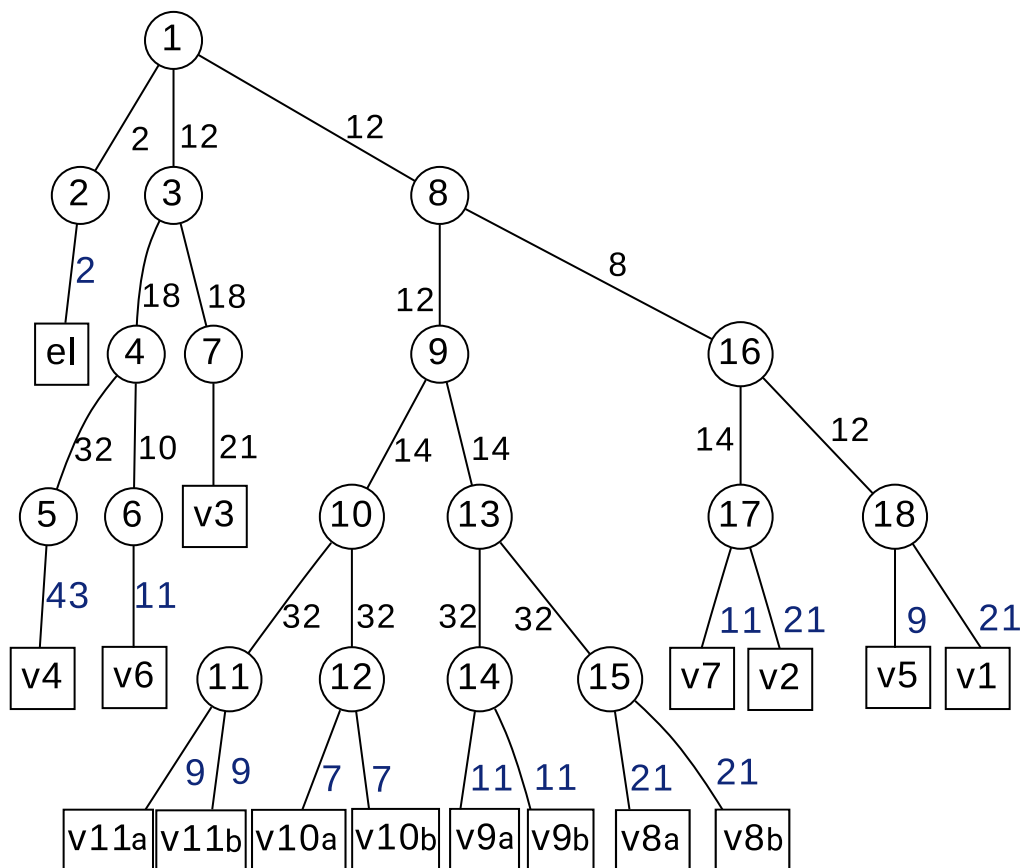


Figure 4.6: The ML-tree used to construct the nuclear wavefunction for 15D allene. The first layer separates the vibrational degrees of freedom (DOF) from the electronic DOF. The number of SPFs used are shown, as well as showing the number of primitive basis sets used to represent the SPFs in the deepest layer, shown here in blue.

of allene and are therefore grouped together. The remaining B_2 and A_1 modes, ν_5 , ν_7 , ν_1 and ν_2 are grouped together as these modes couple with the electronic states most strongly, i.e. on the first order. These are then further separated into B_2 and A_1 groups. Finally, all the E modes are grouped together, and further separated out according to their coupling strengths. The number of SPFs in each layer of the ML-tree were increased until the results were converged, with respect to the photoelectron spectrum.

4.3.2 The Photoelectron Spectrum

Using the QUANTICS package [112], the vibronic Hamiltonian was set up in the operator file using all calculated parameters. All calculations were propagated for 100 fs, with an output calculated every 1 fs. This seemed like a reasonable propagation time which found the balance between efficiency and accuracy. As an example, shown below in figure 4.7 are the 3D spectra obtained by running the propagation for different lengths. The propagation was run for 30, 50, 100 and 200 fs.

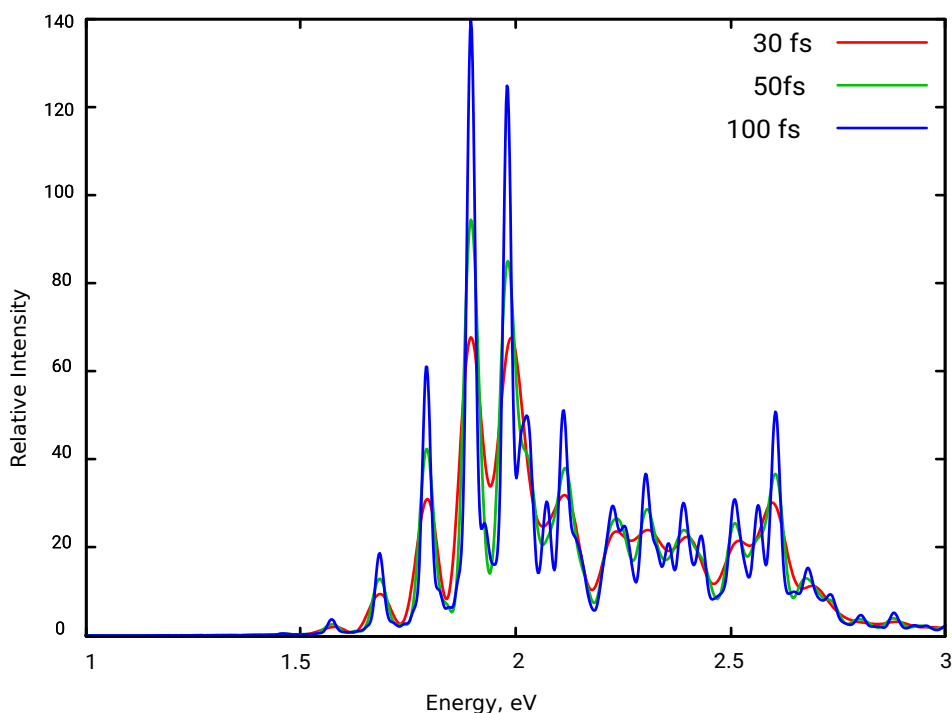


Figure 4.7: The \tilde{X}^2E band of the photoelectron spectrum of allene including 3 modes for a propagation run for 30 fs (red), 50 fs (green) and 100 fs (blue). The calculation was also run for 200 fs, but as it exactly overlays the 100 fs spectrum, it has not been included.

There is no additional detail observed in the spectrum by running the propagation for 200 fs compared to that obtained by a 100 fs propagation, and therefore a propagation time of 100 fs was chosen.

The photoelectron spectrum is calculated by performing the Fourier transform

of the autocorrelation function, which is a measure of overlap between the initial and final wavefunction. Figure 4.8 shows the autocorrelation function for the 3D spectrum obtained using a 100 fs propagation time before the Fourier transform.

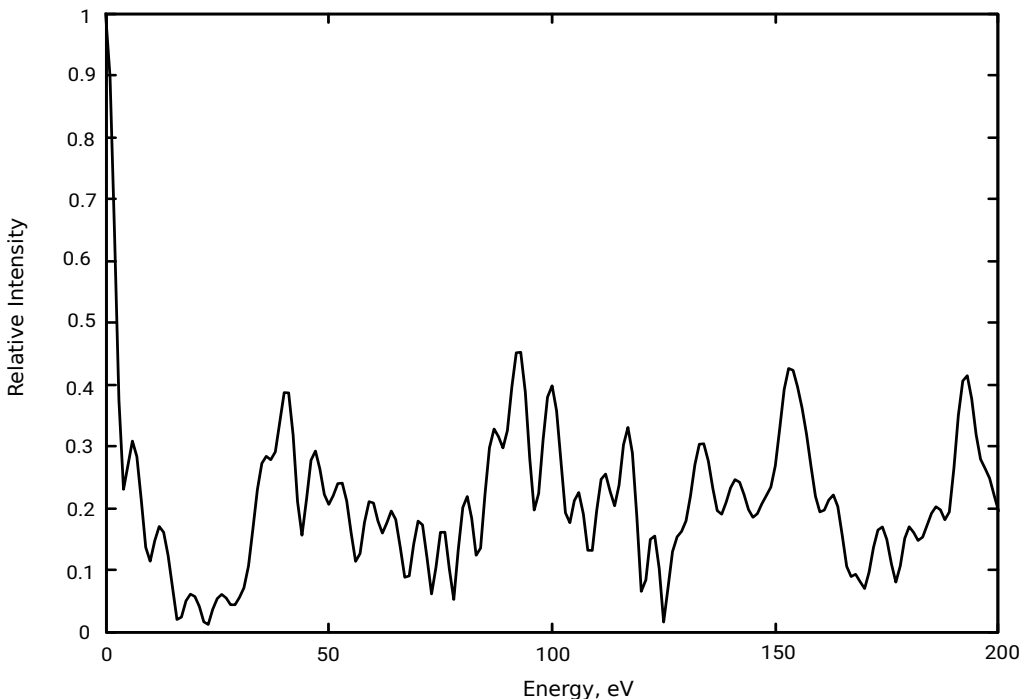


Figure 4.8: The autocorrelation function of the 3D propagation run for 100 fs)

The timings of the calculations are shown in table 4.9.

DOF	MCTDH	ML-MCTDH
3	2 mins	-
7	16 mins	-
15	493.5 hrs	4.8 hrs

Table 4.9: The timings of the propagation of allene to calculate the photoelectron spectrum, using MCTDH and ML-MCTDH, comparing a system containing 3, 7 and 15 DOF.

It should be noted that even after 493 hours, the MCTDH 15 mode calculation still had not reached convergence. It is clearly visible from table 4.9 the exponential scaling of the MCTDH method, and how the use of the ML-MCTDH approach makes treating larger systems quantum dynamically much more feasible.

The relative energy of the plotted spectra in this chapter were shifted to account for 2 factors - the zero-point energy, and also to ensure the adiabatic ionisation peak was in accordance with the experimental peak. Zero-point energy is given by the formula,

$$Z.P.E = \sum_1^i \frac{\omega_i}{2} \quad (4.15)$$

The spectrum was first calculated including only the three most significant modes, ν_4 , ν_6 and ν_3 , in order to verify that the parameters calculated were correct, and to ensure that the vibronic coupling Hamiltonian was a suitable choice for predicting these spectra. It can be seen from this calculated spectrum, figure 4.9(a), that the progression is dominated by the ν_4 mode, confirming the high coupling parameters calculated for this mode. The vibronic structure of the low energy part of the spectrum is well reproduced, as well as the overall width of the peak, but the broadness of the vibronic structure of the high energy part of the spectrum is less well reproduced. This may be due to the exclusion of the rest of the normal modes, or because only coupling terms up to second order are included. Also, the structure of the spectrum is also very sensitive to the frequency and kappa parameters, and therefore, these parameters may not yet be fully optimised.

The spectrum was calculated for the 7D system next, to test the limits of the MCTDH method, and to investigate whether the full spectrum could be reproduced by only including the linear couplings, without the need to go to higher order vibronic coupling, i.e. including the E modes. The results of this are shown in figure 4.9(b). This spectrum, again predicts the low energy part of the spectrum well, accurately predicting the first and second peaks. Including these other first order modes, compared to the previous 3D model, this can much more accurately predict the high energy end of the spectrum. It correctly predicts the position of many of the peaks, as well as replicating the correct intensity trail off.

The full 15-dimensional spectrum, which includes all the vibrational modes,

was then calculated. The results of this are shown in figure 4.9(c). As can be seen, the width of the peak envelope is accurately well reproduced, as well as the relative positions of most of the vibrational peaks. The high energy end of the spectrum is arguably more accurately replicated than in the spectrum that only contains 3 DOFs. However, the low energy part loses some of its characteristic peaks, due to interference from the additional modes, although the adiabatic peak remains well replicated. As these dynamics are run over energy surfaces which are parameterised polynomials, these energy surfaces are not completely accurately calculated. Therefore, as the number of vibrational modes included increases, the errors accumulate. As previously mentioned, the calculation is very sensitive to the frequency and kappa input values, and a more extensive convergence of these parameters would result in a more accurate photoelectron spectrum.

The final spectrum presented here will use the parameters calculated using CASSCF. This is the 3D system, using the same modes as previously used for this sized system, ν_4 , ν_6 and ν_3 . This spectrum is shown in figure 4.10, comparing the experimental spectrum to the one obtain using Quantics.

It can be seen from figure 4.10 that whilst the fitting parameters calculated using CASSCF were similar to those using EPT, the spectrum obtained is not nearly as good a comparison to the experimental spectrum. Comparing figure 4.10 to figure 4.9(a), the CASSCF spectrum is noisy, predicts peaks where there are no peaks, and fails to predict the first peak in the spectrum completely.

4.3.3 The state populations

The PESs plotted in figure 4.4 are the adiabatic state representations, where the states are ordered by energy. Looking at the populations of these states over the course of the propagation gives insight into when the wavepacket reaches the conical intersection. However, in this particular system, as the propagation starts at the conical intersection, the diabatic representations of the states give more

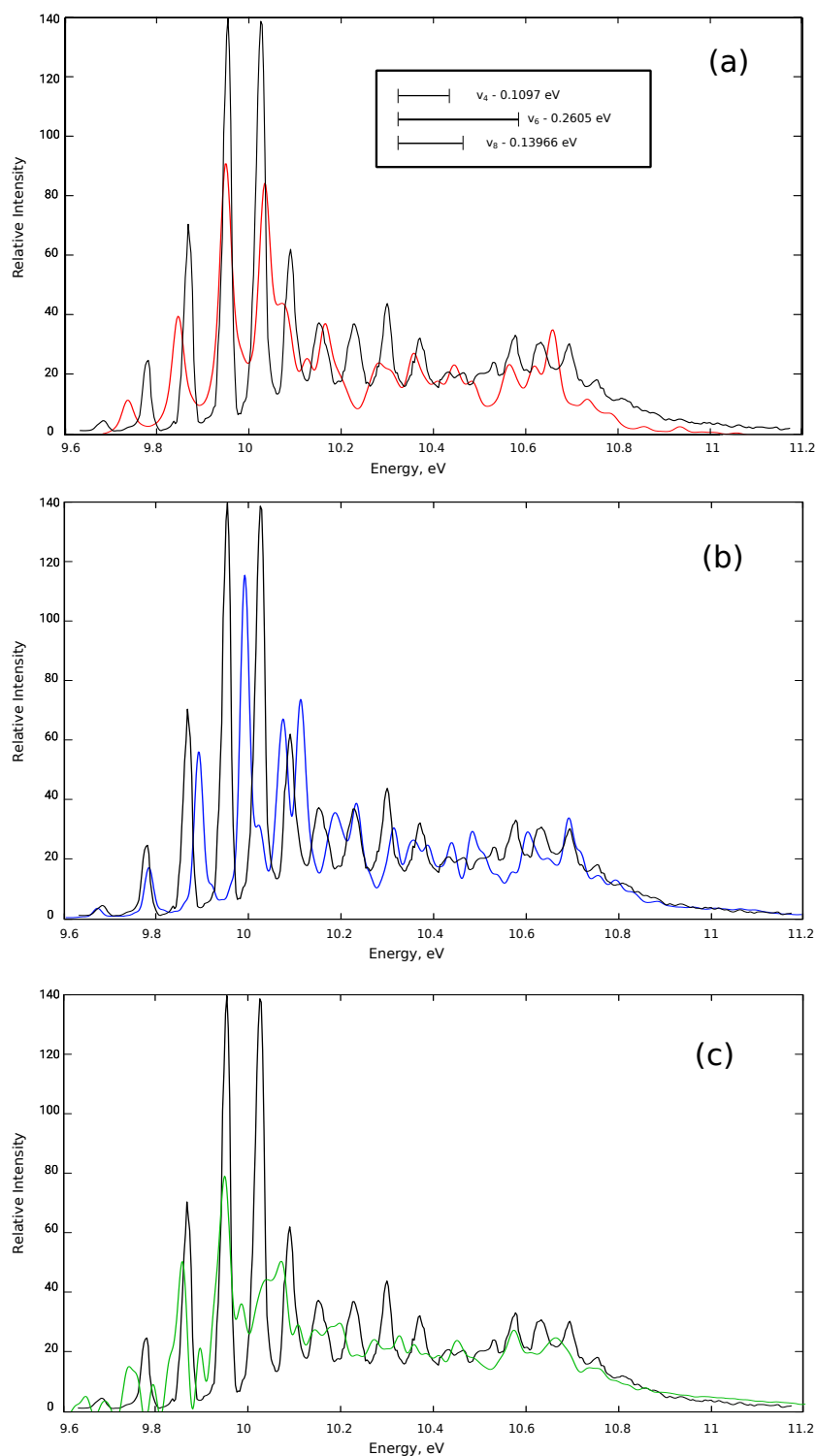


Figure 4.9: The \tilde{X}^2E band of the photoelectron spectrum of allene. The experimental spectrum [111] is plotted in black on each graph along with the results using (a) 3 modes (red plot). The vibrational frequencies of these modes are also shown in the inlay. (b) 7 modes (blue plot), and (c) the full 15 mode system (green plot). All calculated plots have been shifted to overlap the adiabatic peak to that in the experimental spectrum.

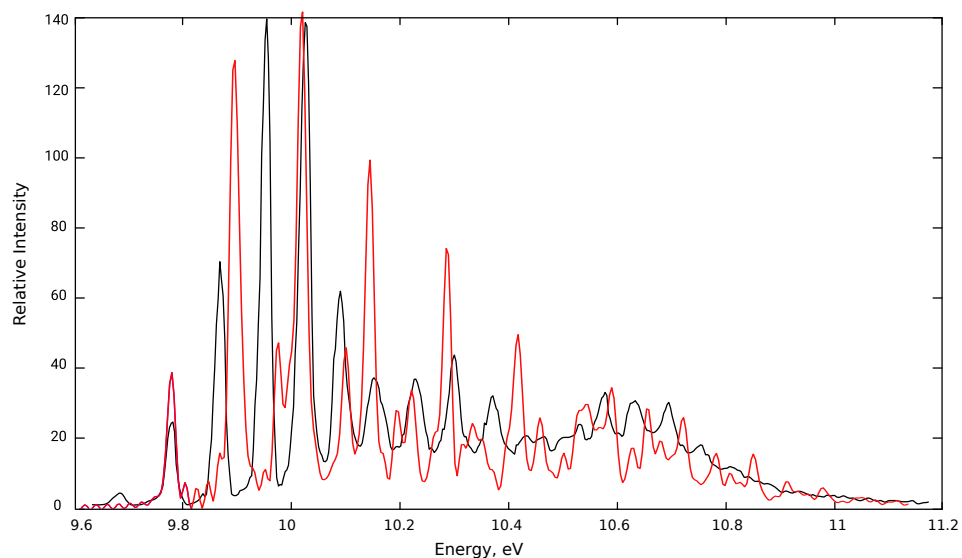


Figure 4.10: The \tilde{X}^2E band of the photoelectron spectrum of allene using the CASSCF parameters. The experimental spectrum [111] is plotted in black, with the calculated spectrum in red.

information about the charge transfer. Diabatic states are ordered by chemical character and cross at conical intersections. As an example, the diabatic PES along ν_4 is shown in figure 4.11.

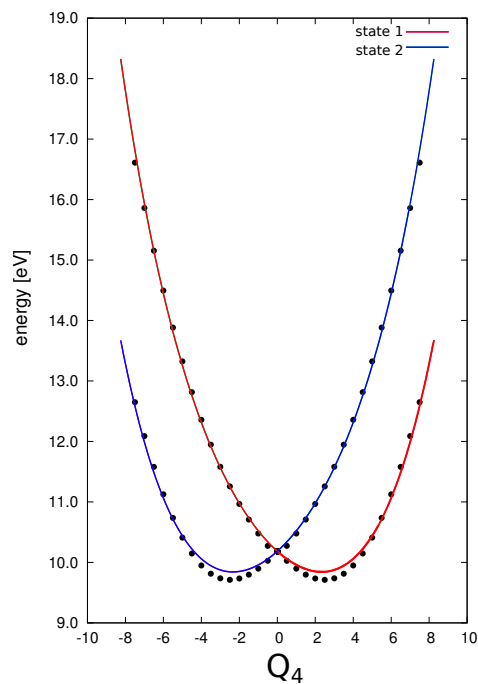


Figure 4.11: The diabatic \tilde{X}^2E state along ν_4

The diabatic state populations for the 3 propagations were also calculated, and are shown in figure 4.12.

The wavepacket starts the propagation fully in state 2. It only takes 15 fs for the wavepacket to have equally populated the two states in all 3 system sizes. The wavepacket oscillates back and forth between the two states. In the larger systems, 7D and 15D, the wavepacket energy is quenched by the additional vibronic motion, and the wavepacket stabilises more quickly. In the 7D system, it stabilises into equally populating the 2 states by 70 fs. In the full 15D system, the system stabilises with the majority of population in state 2 after just 40 fs.

One can also gain insight into the behaviour of the three most active modes, ν_4 , ν_6 and ν_3 , by plotting the mode expectation values for each of the systems studied. This shows how much each mode gets excited by the charge transfer by determining the position of the centre of the wavepacket along the PES of the mode and state of interest. The results of this are shown in figure 4.13.

Mode ν_6 and ν_3 show that they are excited by the charge transfer as seen by the increased oscillatory movement of the expectation value of the wavepacket along those modes.

Due to the symmetry of the torsional motion, to see the effect of the charge transfer on the coupling mode ν_4 we need to calculate the expectation value of the step function at $Q=0$, i.e a torsion angle of 90° . This is a Heaviside step function, where the expectation value measures the proportion of the wavepacket which is to the right hand side to the function placed at $Q=0$. These results are shown in figure 4.14.

In the 3D and 7D, charge transfer leads to a closing up of the torsion, whereas in the 15D calculation the torsion returns to its initial value of 90° .

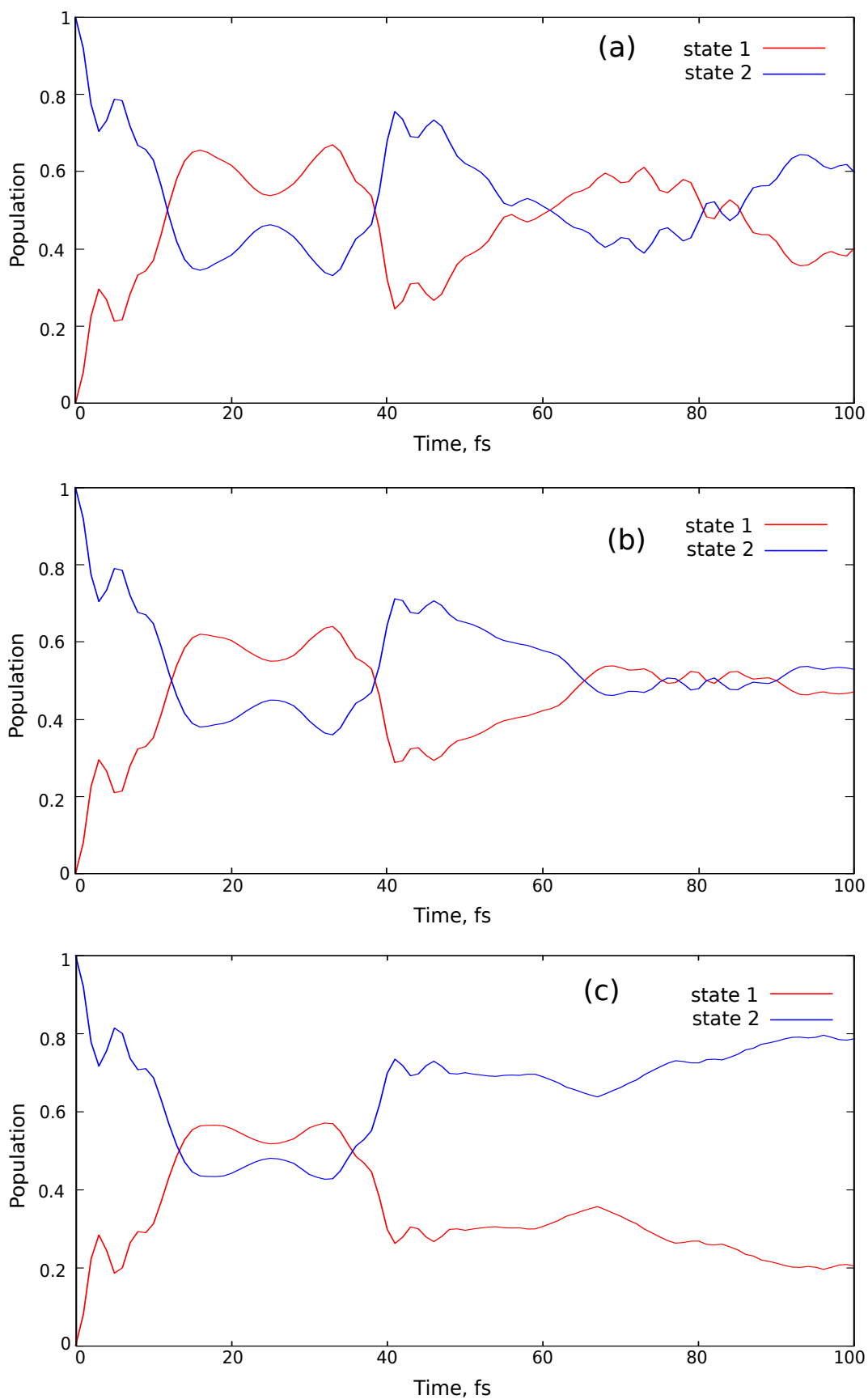


Figure 4.12: The diabatic state populations in the (a) 3D, (b) 7D, and (c) 15D system. The system begins the propagation in state 2.

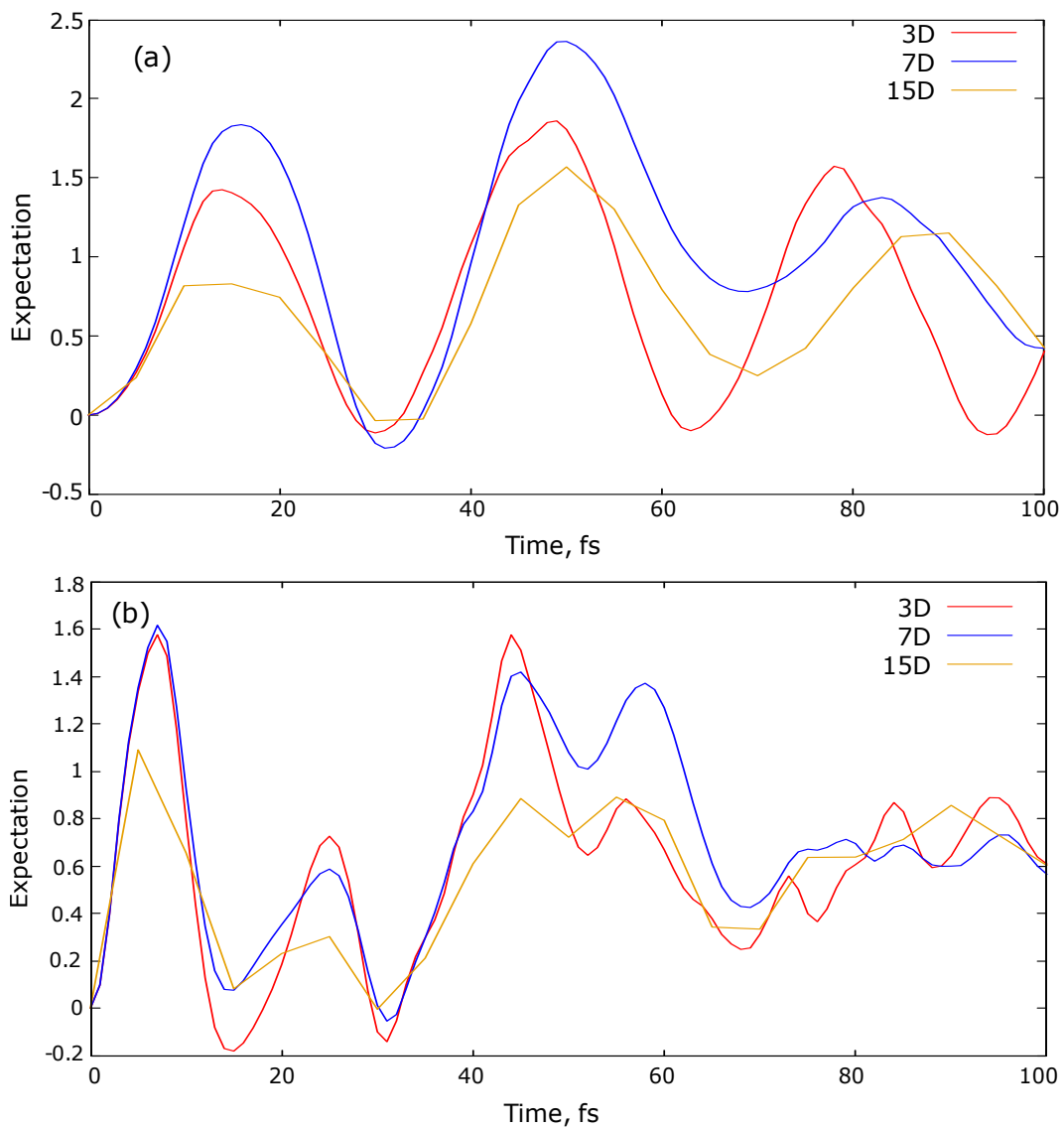


Figure 4.13: The mode expectation values of (a) ν_6 , and (b) the ν_3 in state 2 of the 3D, 7D and 15D systems

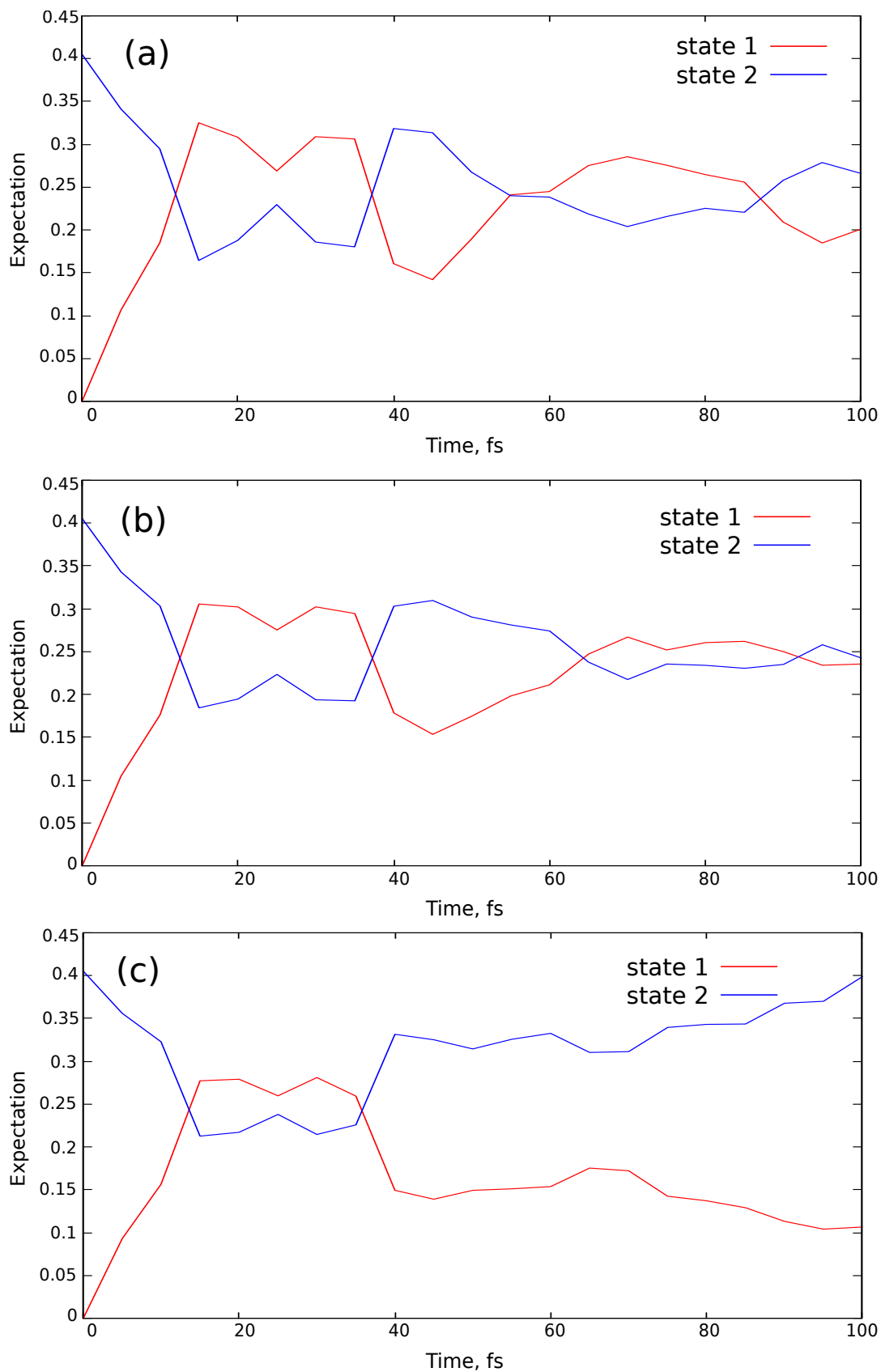


Figure 4.14: The expectation value of the step function along the torsional ν_4 in the (a) 3D, (b) 7D, and (c) 15D system.

4.4 Summary

From looking at the calculated photoelectron spectra for allene, as well as previous studies on various other systems [114, 115, 116], it can be shown that the vibronic Hamiltonian is a robust way to predict the photoelectron spectrum, and, especially when coupled to a ML-MCTDH calculation, the vibronic Hamiltonian can provide an efficient method to investigate larger, more complicated systems quantum dynamically. The main bottleneck to this method, as with all of these types of grid based methods, is that the PESs needed to be calculated before any quantum dynamics calculations can take place. In order to fully parameterise and optimise the potential surface of allene, a molecule with just 7 atoms, could potentially take years, and thus becomes the biggest hurdle to these methods. The most obvious way to overcome this problem would be to choose a method which removes the need to pre-calculate these energy surfaces. Direct dynamical methods, as mentioned in chapter 3, are able to calculate the PESs on-the-fly, and therefore offer a promising method to expand this research.

Chapter 5

Coumarin-343 - TiO₂

5.1 Introduction

The photoinduced electron transfer at dye-semiconductor interface has been extensively studied experimentally [117, 118, 119, 120], in particular the electron injection process. This is where the electron in the excited state of the dye molecule is injected into the conduction band of the semiconductor, and is a crucial step in the efficiency of dye-sensitised solar cells, as described in 2.7.2. This electron injection process is ultra-fast, with some injection times recorded as fast as 6 fs, such as for an alizarin dye molecule adsorbed on TiO₂ [120]. In this chapter, the electron injection process of an electron in the excited state of Coumarin-343 (C-343) into the conduction band of TiO₂ was investigated, taking into account the couplings to nuclear motions. This injection process has been recorded to take several tens of femtoseconds, meaning that there must be vibronic coupling affecting the process [121]. Therefore, a simple decay function is not sufficient enough to explain the decay of the donor state population, and a quantum dynamical approach which includes the vibrations of the system is required to fully explain the dynamics of this process. Due to the fact that the continuum of acceptor states representing the conduction band of the semiconductor has to be taken into account, this dye-semiconductor interface is not as well studied theoretically as it is experimentally, with questions as to how the continuum couples to the dye

molecule, as well as any solvent environment. Data published in a series of studies by Thoss et al [122, 123, 124], where the injection time of an electron from an excited Coumarin dye molecule to the conduction band of TiO₂ was modelled, was used as a benchmark for these results. The first step in simulating the dynamics of this process was to determine the optimised structure of C-343, as well as the vibrational frequencies. These calculations, described in section 5.2, were performed using density functional theory (DFT), with a B3LYP functional and a cc-pVTZ basis set, using the Gaussian 09 [125] software package. The dynamics of the dye-semiconductor system were initially described using a Anderson-Newns type Hamiltonian [126],

$$H = T + |\phi_g\rangle V_g \langle \phi_g| + |\phi_d\rangle V_d \langle \phi_d| + \sum_k |\phi_k\rangle V_k \langle \phi_k| + \sum_k (|\phi_d\rangle V_{dk} \langle \phi_k| + |\phi_k\rangle V_{kd} \langle \phi_d|), \quad (5.1)$$

where V_g is the ground state PES, and V_d and V_k are the potential energy elements of the diabatic matrix of the donor state $|\phi_d\rangle$, and the discretised continuum of acceptor states, $|\phi_k\rangle$, respectively. The details and results of these calculations can be found in section 5.8. As in allene, the potential energy surfaces (PES) of the donor and acceptor states are Taylor expansions around the equilibrium geometry of the ground state of the dye molecule at the Franck-Condon point.

With time, it became apparent that this model has been misinterpreted and that it is, in fact, an unsuitable method to describe this electron injection process. This is due to the incorrect description of how the electronic state coupling terms, V_{dk} , are determined. The failings of this method are discussed further in section 5.8. A change of approach was needed, and the model system was changed from a donor-acceptor Hamiltonian based on PES to an atomistic Hamiltonian, where the donor state energy is that of the HOMO of the first excited state of C-343 relative to the bottom of the conduction band of TiO₂, and the acceptor states

are formed by a representation of the binding site energies of the semiconductor, the parameters of which are based on the previous tight-binding approach. The details and results of this new method can be found in section 5.9. This new model is able to give electron transfer rates which include the effects of vibronic coupling.

5.2 Electronic Structure

All the following calculations were performed using Gaussian-09 [125], unless stated otherwise. Firstly, the geometry of C-343 was optimised and the vibrational modes calculated in the ground state. As the dye attaches onto the semiconductor surface in the deprotonated form, this was repeated for both protonated and deprotonated C-343. Following the determination of the vibrational modes, it was decided which of these modes were of most significance to an electron transfer process. Electronic structure calculations were then performed on a few small TiO₂ clusters, of varying sizes, in order to determine some additional parameters and the geometry of the C-343-TiO₂ complex. The results of these calculations will be discussed in the following sections.

5.3 Geometry Optimisation

C-343 - C₁₆H₁₅NO₄ - can exist in many conformers, both with respect to the geometry around the nitrogen and geometry of the -COOH group. It has been shown that the syn- and anti- geometry around the nitrogen play little to no part in the dynamics of this process [127], and therefore the lower energy syn-C-343 conformer was chosen. With respect to the conformation of the -COOH group, there are three possible geometries, shown in figure 5.1.

Despite the energy of the arbitrarily named Geometry-1 conformer is the lowest, due to the formation of an intermolecular hydrogen bond creating a 6-membered ring, a further vibrational analysis showed that the conformer used in the Thoss et

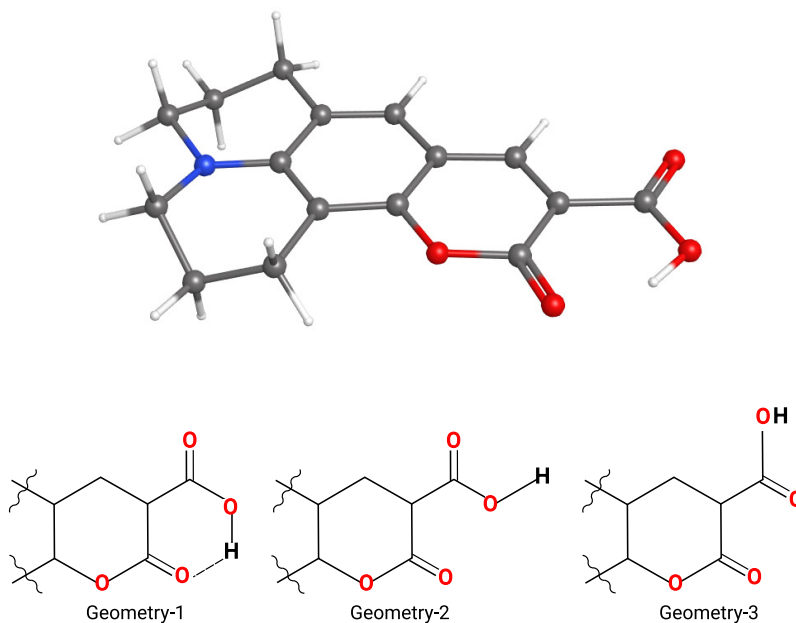


Figure 5.1: The top panel shows the optimised structure of Coumarin-343, in Geometry-1. Labelled below are the possible conformers of the -COOH group. For clarity, only the acid part of C-343 has been shown.

al series [128], to which the results shown here were benchmarked, was Geometry-3. Therefore, the vertical excitation and ionisation energy calculations, and the resulting force parameters, on the isolated dye molecule proceeded using Geometry-3. The choice of this conformer ultimately should not greatly affect the results as when the dye is attached to the surface of the semiconductor, the hydrogen on the -OH group detaches and migrates to the semiconductor surface, meaning there is no distinction of these geometries after surface adsorption. The optimised geometry of the dye molecule in chosen Geometry-3 can be seen in figure 5.2.

The optimised geometry of the deprotonated dye is shown in figure 5.3.

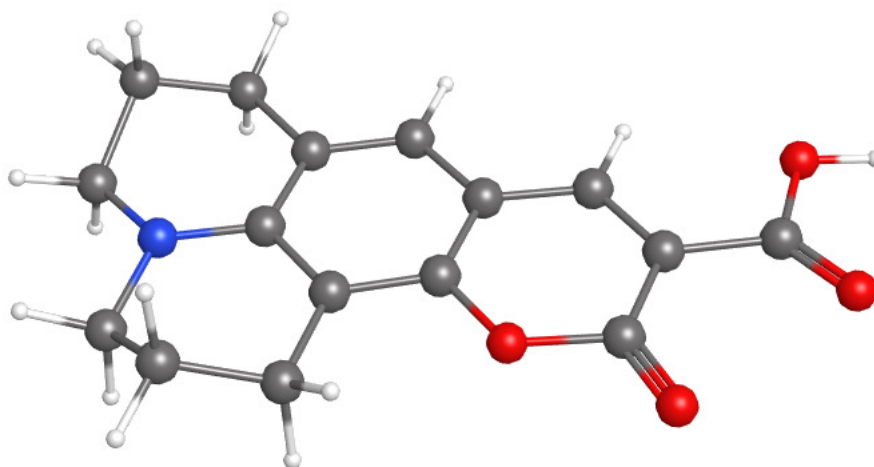


Figure 5.2: The optimised geometry of Coumarin-343 used in the following calculations. The molecule is effectively planar, except for the puckering around the nitrogen. Upon adsorption to the TiO_2 surface, the hydrogen on the hydroxyl group detaches and bonds to a terminal oxygen in the semiconductor .

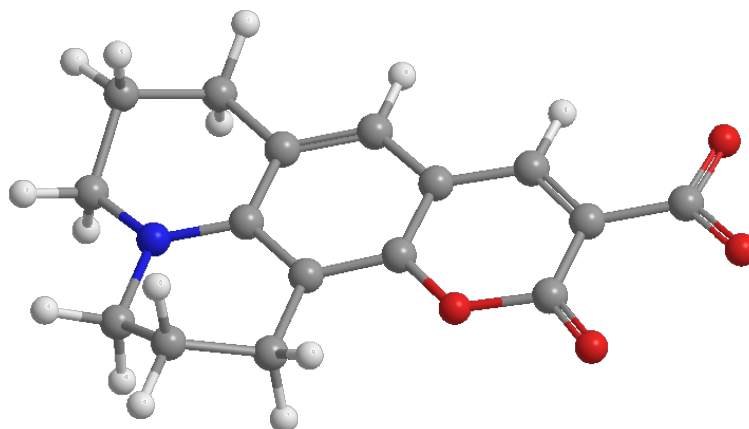


Figure 5.3: The optimised geometry of deprotonated form of Coumarin-343. The molecule has not lost any planarity by losing a proton.

5.4 Normal Mode analysis

Using the optimised protonated structure of C-343 in geometry-3, the vibrational modes were determined using different levels of theory and compared to other theoretical values [123], with the results using a B3LYP/cc-pVTZ basis set best

mirroring these values. These results are shown in table A.1 in the appendix.

From these normal modes, the kappa values were determined as described in chapter 4. Here, the donor kappa values, (κ_i^d) , refer to the displacement of the first excited state of the isolated dye molecule, and the acceptor kappa values, (κ_i^a) , refer to the displacement of the ground state of the cationic dye molecule, both with respect to the ground state of the neutral dye molecule. With 102 normal modes, in order to simulate the dynamics of this process, it was beneficial for the preliminary propagations to identify the key modes that are important to this charge transfer. These modes were chosen on the coupling strength. This is a unit-less parameter which can be determined by the relationship (λ_i/ω_i) , where λ_i is the reorganisation energy and ω_i is the frequency of the normal mode, i . The reorganisation energies, λ_i^α , were calculated from the relationship shown below and are associated with transitions from the ground state to the excited state and the cation of C-343, where $\alpha = d$ or a , respectively,

$$\lambda_i^\alpha = \frac{(\kappa_i^\alpha)^2}{2\omega_i}. \quad (5.2)$$

The reorganisation energy of electron transfer is associated with a transition from the excited state of the dye molecule to the ground cationic state, and is expressed as,

$$\lambda_i^{ET} = \frac{(|\kappa_i^d - \kappa_i^a|)^2}{2\omega_i}, \quad (5.3)$$

where the λ_i^{ET} refers to the reorganisation energy of electron transfer. A simple schematic of what these equations represent is shown in figure 5.4.

In order to choose which of the modes of C-343 were significant in the electron transfer process, a threshold of 0.1 was chosen for the λ_{ET} coupling parameter. This allowed 102 modes to be initially reduced to 17 modes, as shown in table 5.1.

These 17 modes contain $\sim 84\%$ of the total reorganisation energy for the transi-

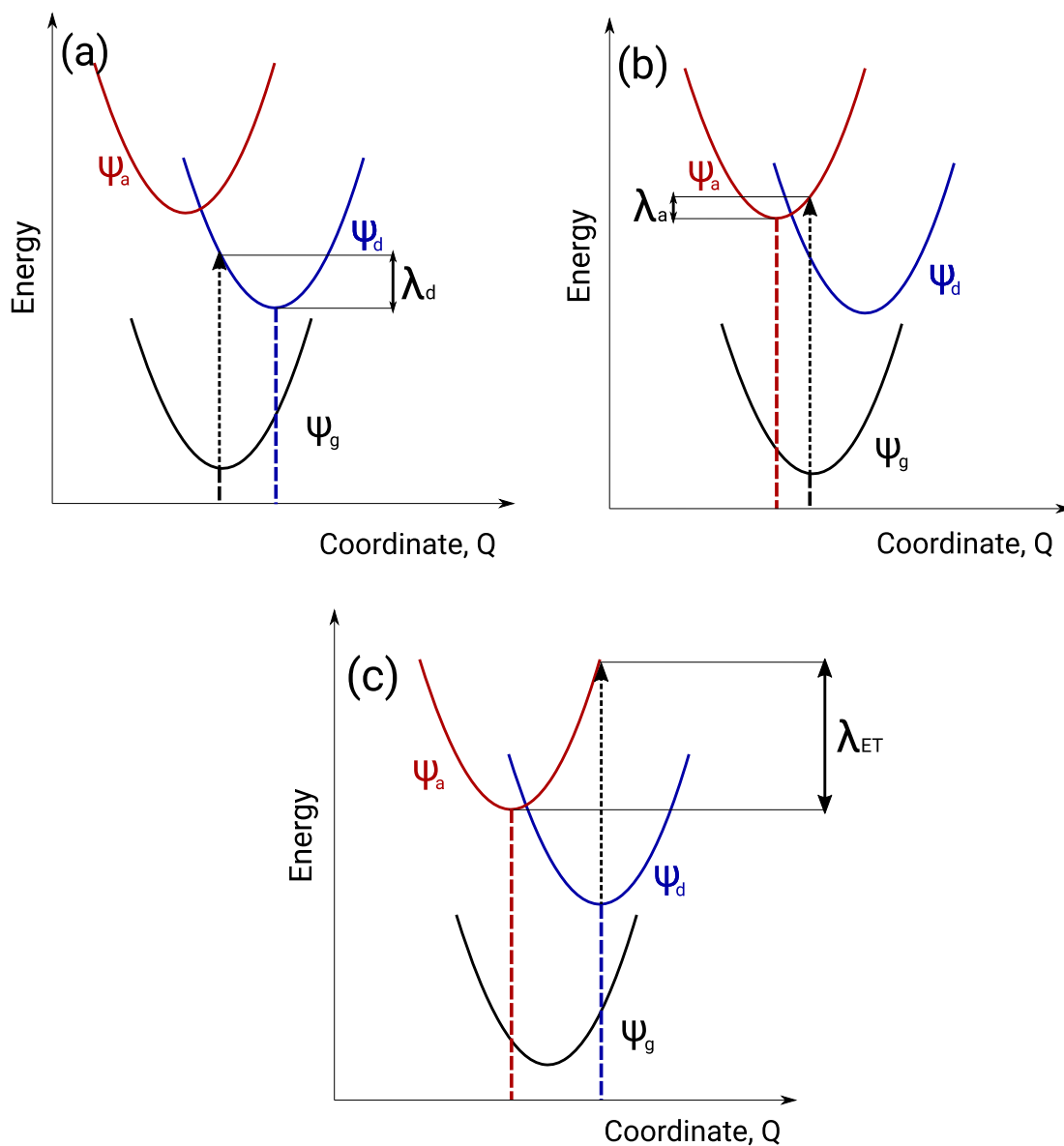


Figure 5.4: A schematic showing the reorganisation energy in a three state system along some normal mode, Q . In all three diagrams, the black state, ψ_g , represents the ground state, the blue state, ψ_d represents the donor state, and the red state, ψ_a , represents the acceptor state. (a) shows the donor reorganisation energy, λ_d . (b) shows the acceptor reorganisation energy, λ_a . (c) shows the reorganisation energy of the electron transfer process, λ_{ET} .

tion to the electron transfer process, where the total reorganisation energy, shown in equation 5.4, is the sum of the reorganisation energies. Therefore, using only these 17 modes is a good approximation of the full system. The 4 most significant modes alone contain 64% of the total reorganisation energy, and therefore provide

Mode	ω (eV)	κ^d (eV)	κ^a (eV)	λ^{ET} (eV)	Coupling Strength
6	0.01579	0.05815	-0.03995	0.30471	19.29622
7	0.01723	0.00455	0.07570	0.14687	8.522713
5	0.01205	-0.00139	-0.01865	0.01236	1.025842
10	0.02812	-0.00031	0.03637	0.02392	0.850690
1	0.00334	0.00200	-0.00191	0.00229	0.686325
15	0.04332	0.01165	-0.03146	0.02145	0.495237
9	0.02704	0.00688	-0.01751	0.01100	0.406751
11	0.03361	0.02104	-0.00523	0.01027	0.305385
17	0.05022	-0.03889	0.00026	0.01526	0.303795
14	0.04072	0.00585	-0.02578	0.01228	0.301544
3	0.00673	0.00168	-0.00319	0.00175	0.260554
19	0.05412	0.00712	-0.02928	0.01224	0.226135
30	0.08521	0.00339	-0.05002	0.01674	0.196431
29	0.07944	-0.03378	0.01269	0.01359	0.171105
86	0.22078	-0.04414	0.06700	0.02797	0.126703
25	0.06939	0.01730	-0.01748	0.00872	0.125653
13	0.03886	-0.00296	0.01599	0.00462	0.118921

Table 5.1: The coupling strengths of the main vibrations in Coumarin-343. All values are mass-frequency scaled. It is clear from the table that mode 6 is by far the most significant mode for electron transfer, which is a rocking motion of the carboxyl group.

a good starting point for the preliminary calculations.

$$\lambda_{Tot}^{ET} = \sum_i \lambda_i^{ET} \quad (5.4)$$

5.5 TiO₂

The choice of TiO₂ as the semiconductor was based on the fact that it is one of the most promising semiconductors for solar applications [129], on top of the fact that it has already been well studied both experimentally and theoretically [123, 124, 130]. TiO₂ exists in three main polymorphs - anatase, rutile and brookite [131]. The anatase polymorph has been shown to be the most photoactive of all three [132], with the most stable, and common, surface having a (101) orientation, shown in figure 5.5.

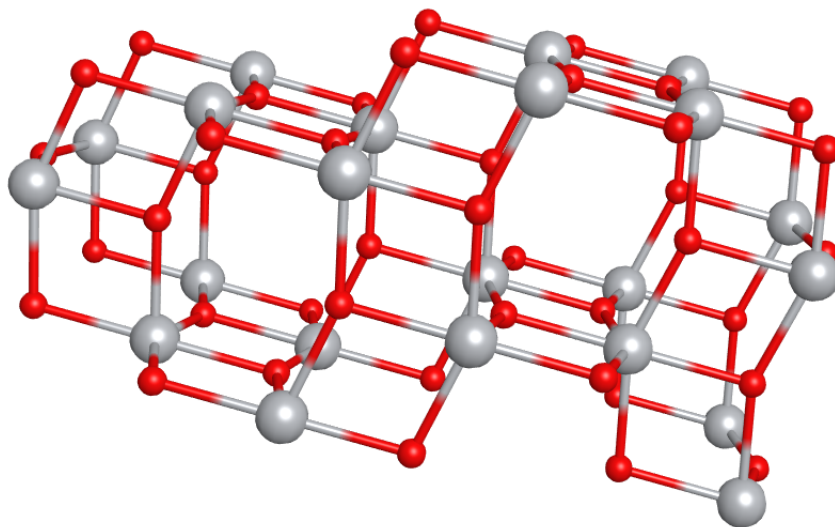


Figure 5.5: A (101) surface of anatase TiO₂

In order to find the electronic structural properties of a C-343 dye molecule attached to a TiO₂ surface, firstly, a small (TiO₂)₈ cluster was optimised. The starting geometry of this cluster was obtained from experimental data published by Howard et al. from the x-ray diffraction results [133]. Then the optimised geometry of a dye molecule adsorbed onto a small (TiO₂)₂ dimer was performed. Both these structures are shown in figure 5.6.

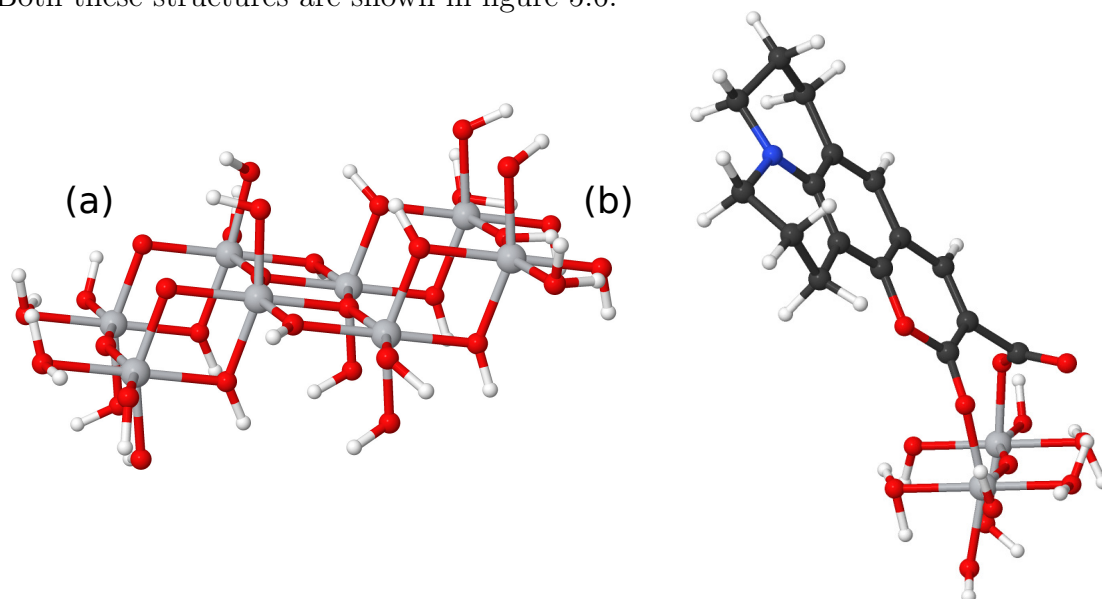


Figure 5.6: The optimised geometry of (a) (TiO₂)₈(H₂O)₁₄ cluster and (b) (TiO₂)₂(H₂O)₅ cluster with the deprotonated C-343 dye molecule attached

The resulting optimised geometry of the deprotonated dye molecule after this geometry optimisation was attached to the larger $(\text{TiO}_2)_8$ cluster, allowing only the bonds attaching the dye to the TiO_2 to optimise. The resulting geometry is shown in figure 5.7.

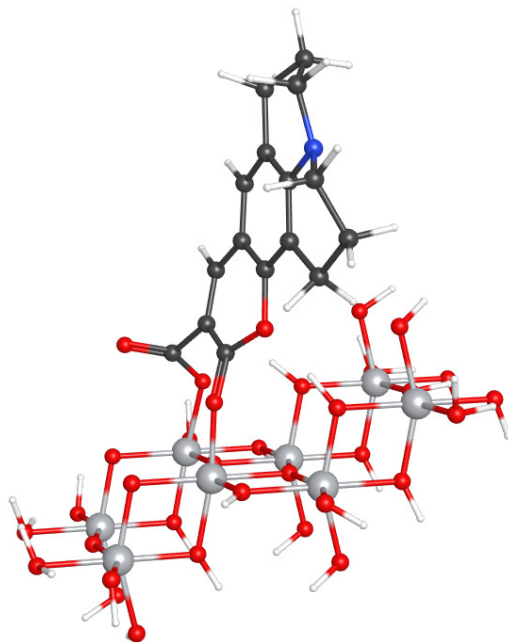


Figure 5.7: The optimised geometry of a $(\text{TiO}_2)_8(\text{H}_2\text{O})_{14}$ cluster with the deprotonated C-343 dye molecule attached

Using this optimised geometry, the energy of the molecular orbitals of this complex were determined.

5.6 Molecular Orbitals

The donor state of the system is the first excited state of C-343. A TDDFT and an EOM-CCSD calculation on the isolated C-343 molecule agreed that this excited state arises due to an electron promotion from the HOMO to the LUMO. The results of these calculations can be found in table 5.2. Both calculations were run using the same input geometry, using a cc-pVTZ basis set. In both cases, the orbitals had the same character.

	Excited state	Energy (eV)	Oscillator strength
EOM-CCSD	HOMO \rightarrow LUMO	4.4376	0.9332
TDDFT	HOMO \rightarrow LUMO	3.3784	0.5935
Expt. [134]	-	2.8051	-

Table 5.2: This table shows that the first excited state of C-343 arises from the promotion of an electron from the HOMO to the LUMO, as confirmed by both EOM-CCSD and TDDFT. This is compared to the experimental absorption λ_{max} of C₃₄₃ obtained in methanol.

The difference in values between the experimental and quantum chemical results could be attributed to solvent-solvent interaction effects [135], which becomes more and more prominent in high polar solutions. Experimental studies have shown that as the polarity of the solvent increases, the absorption λ_{max} decreases, and the peak in the spectrum becomes broader [135].

Therefore, although the calculated energy gap is too large to be fully efficient in the visible spectrum and is much larger than has been shown experimentally, this system is more of a test to check the methods used, rather than as a design for the best DSSC so therefore we were happy to continue with this system.

The donor state can be thought of as the LUMO of the C-343 dye molecule. The HOMO and LUMO of C-343 were calculated, and are shown in figure 5.8.

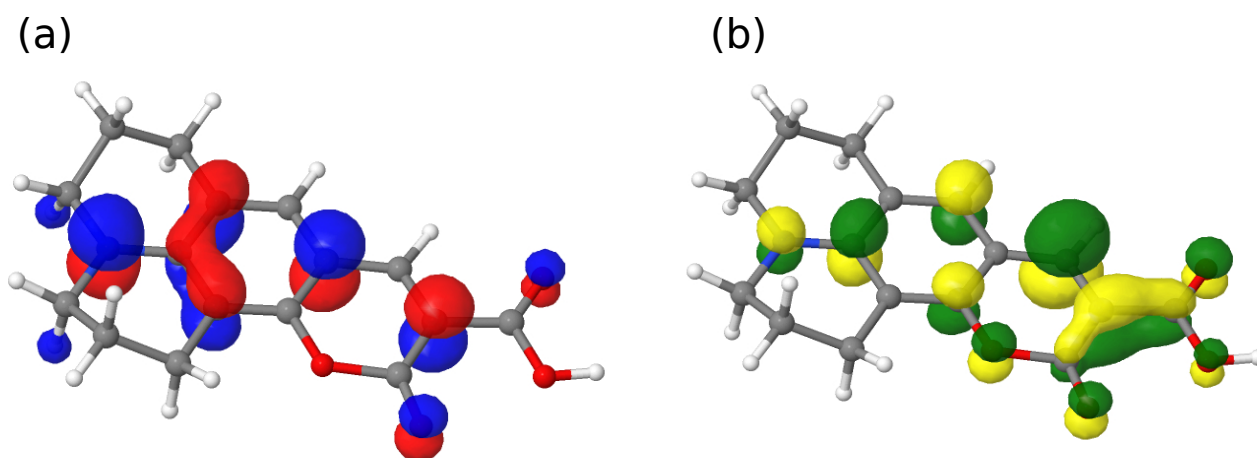


Figure 5.8: (a) The HOMO of the isolated C-343 dye molecule (b) The LUMO of the isolated C-343 dye molecule

Since the donor orbital of the isolated dye is known, the next step was to find the donor orbital of the C-343-TiO₂ complex. A MO calculation on the smallest complex, the dye attached to a (TiO₂)₂ dimer, was performed. The donor orbitals of the complex was chosen to best represent the LUMO of the isolated dye molecule. This was orbital 126, and is shown in figure 5.9.

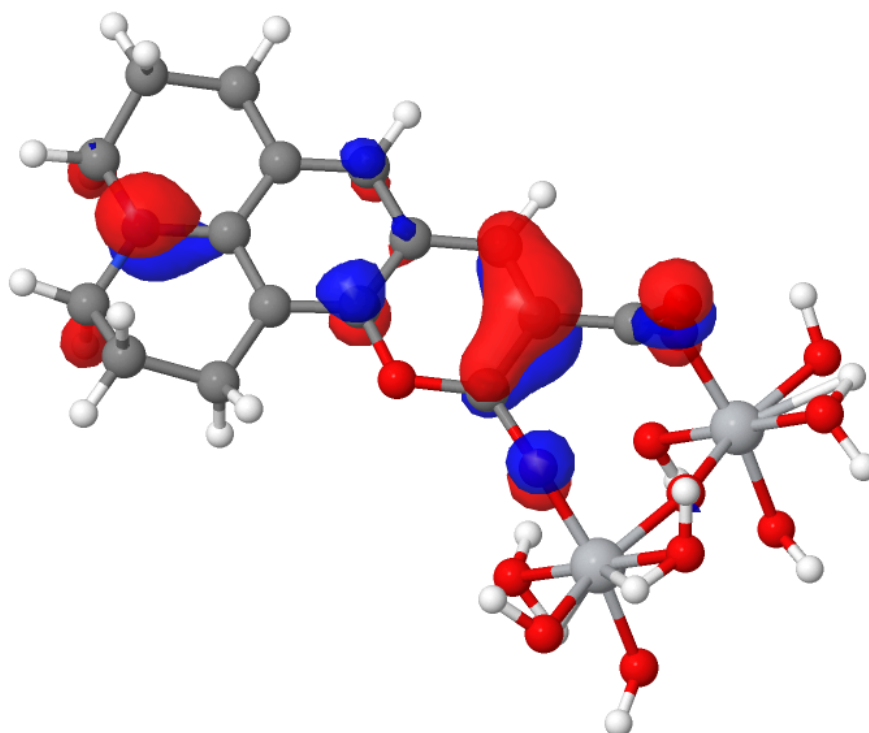


Figure 5.9: The donor orbital of the dye-semiconductor cluster

These acceptor orbitals were defined as being those which are localised on the TiO₂ cluster only. Looking at the orbital overlap between the donor and acceptor orbitals could give some insight into the parameters of the model- namely, the coupling between the dye and the semiconductor. This will be discussed further in section 5.9.

5.7 Electron transfer

Having determined some electronic structure parameters for both the dye and semiconductor clusters, as well as the dye-semiconductor complex, in order to determine the electron transfer time the next step was to run quantum dynamics simulations starting from the donor state. The propagation of the wavepacket was performed using the Quantics software package [112]. The MCTDH and ML-MCTDH method, both of which are discussed in chapter 3, were used to determine the dynamics. The grouping of vibrational modes using these methods were based on coupling strength alone, as symmetry could not be used on this system as in the case of allene. In order to ensure convergence had been reached, the natural orbital populations were checked as in the previous chapter, as well as checking whether the state population plots change by adding more SPFs. The tight-binding Hamiltonian that was used in both the approaches had not been tested before using this software. It was, therefore, necessary to implement certain aspects of it into the code. This included setting up the decay width function for the off-diagonal parameters used in the first method that will be discussed, as well as setting up the acceptor matrix used for the atomistic approach of the second method. This will all be expanded upon in more detail in the following sections.

5.8 Dynamics I

5.8.1 The Hamiltonian

The initial model used, inspired by the series of papers published by Thoss et al [123, 128, 136], was based on an Anderson-Newns type Hamiltonian (shown in equation 5.5), with a one-dimensional tight binding parameterisation to find the eigenvalues and eigenfunctions of the semiconductor,

$$H = T + |\phi_g\rangle V_g \langle \phi_g| + |\phi_d\rangle V_d \langle \phi_d| + \sum_k |\phi_k\rangle V_k \langle \phi_k| + \sum_k (|\phi_d\rangle V_{dk} \langle \phi_k| + |\phi_k\rangle V_{kd} \langle \phi_d|), \quad (5.5)$$

where V_g , V_d and V_k correspond to the diabatic potential energy surfaces of the ground state of the dye molecule, the donor state- which refers to the first excited state of the dye -, and the continuum of acceptor states on the conduction band of the semiconductor, respectively.

This method is based on modelling the system as a spin-boson type system, with a donor and acceptor state, except instead of having only one acceptor state, there is now a continuum of acceptor states. This can be seen in figure 5.10.

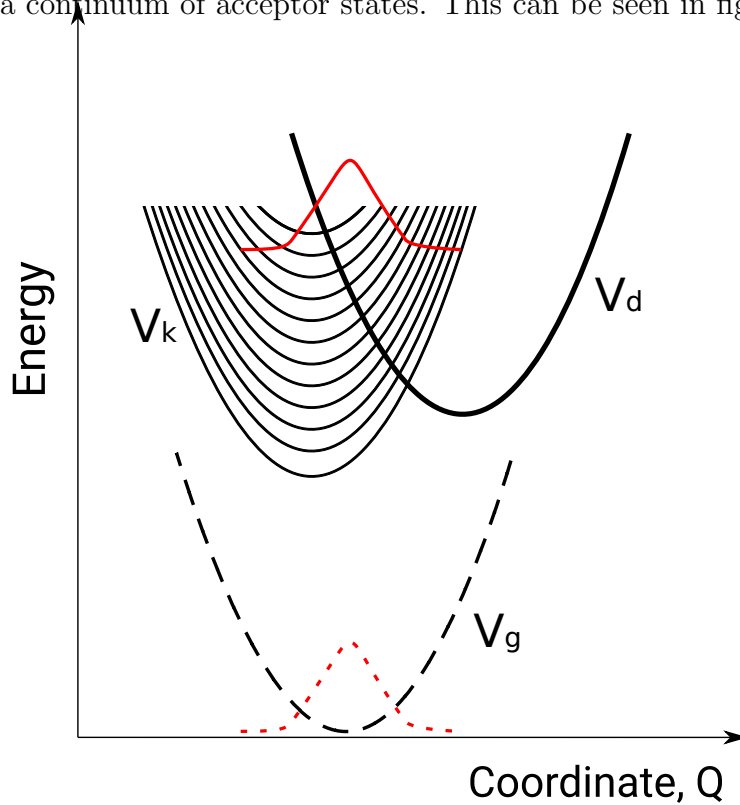


Figure 5.10: An illustration of the PES along some coordinate, Q , of the ground, donor and acceptor states, V_g , V_d and V_k respectively, adapted from [1].

The coupling between the donor and acceptor states is determined by the off-diagonal coupling matrix elements, V_{dk} , which can be determined by the energy-dependent decay width of the donor state,

$$\Gamma(E) = 2\pi \sum_k |V_{kd}|^2 \delta(E - \epsilon_k). \quad (5.6)$$

The parameterisation of the energy decay function was adapted from the tight-binding model developed by Petersson et al [136] which describes electron injection rates from a dye molecule into a semiconductor. This model gives the energy-dependent decay width as,

$$\Gamma(E) = \frac{2v_0^2(E - E_0)}{v^2} \sqrt{1 - \left[\frac{(E - E_0) - \epsilon^2 - 2v^2}{2v^2} \right]^2}. \quad (5.7)$$

Here, E_0 is the mean energy value of the conduction and valence bands of the semiconductor, $\pm\epsilon$ are the on site energies of the atoms in the metal semiconductor, v is the nearest neighbour coupling matrix element, and v_0 is the coupling element between the semiconductor and the chromophore. The limitation of $\epsilon + E_0 \leq E \leq E_0 + \sqrt{4v^2 + \epsilon^2}$ was imposed in order to contain the energy values within the width of the conduction band of TiO_2 . The parameters were initially set to E_0 as -1.6 eV and ϵ as 1.6 eV, so that the bottom of the conduction band was at zero. v was set to 2 eV and v_0 to 1 eV. These parameters were found semi empirically by Petersson et al [136], and are determined to resemble the lower 3d group of the conduction band of TiO_2 .

A simple schematic of this approach can be shown in diagram 5.11.

If only linear coupling terms are taken into account for the donor and acceptor states, then the following equations for the diabatic PES can be written, in mass-frequency scaled coordinates as,

$$V_g(Q) = \epsilon_g + \frac{1}{2} \sum_l \omega_l Q_l^2, \quad (5.8)$$

$$V_d(Q) = \epsilon_d + \sum_l \kappa_l^d Q_l + \frac{1}{2} \sum_l \omega_l Q_l^2, \quad (5.9)$$

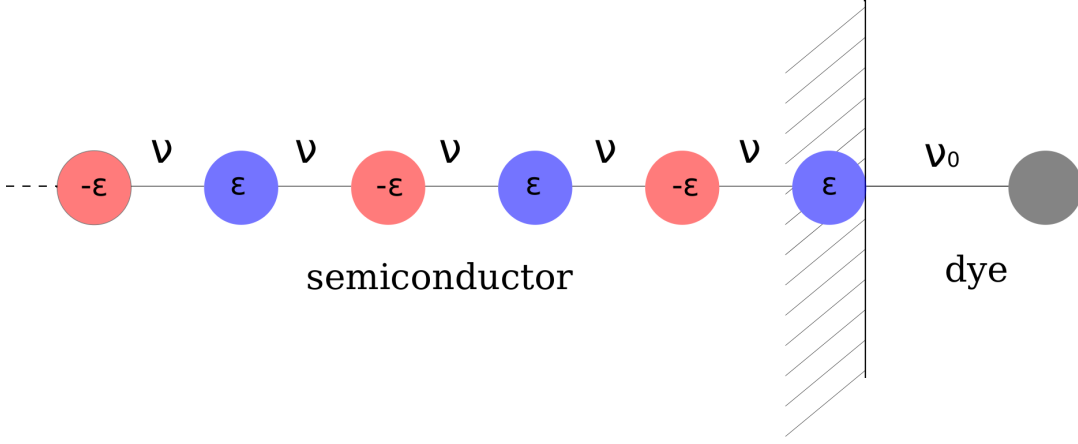


Figure 5.11: A schematic showing how the 1D tight binding approach was applied to the dye-semiconductor system. Adapted from [136]. The on-site matrix elements alternate signs to depict either a titanium site ($+\epsilon$) or an oxygen site ($-\epsilon$).

$$V_a(Q) = \epsilon_k + \sum_l \kappa_l^a Q_l + \frac{1}{2} \sum_l \omega_l Q_l^2, \quad (5.10)$$

where ϵ_g , ϵ_d and ϵ_k are the energies of the ground state, donor state and acceptor states at the ground state equilibrium geometry respectively. The kappa, κ , constants, as in section 4.1, are obtained by calculating the gradients of the donor or acceptor states at the equilibrium geometry, and contain the information necessary to couple nuclear motion to the electronic states. The matrix form of the Hamiltonian can be expressed as in matrix 5.11. For simplicity and clarity, in this example there is only 4 states in the acceptor continuum.

$$\begin{pmatrix} & \phi_g & \phi_d & \phi_{k1} & \phi_{k2} & \phi_{k3} & \phi_{k4} \\ \phi_g & V_g & 0 & 0 & 0 & 0 & 0 \\ \phi_d & 0 & V_d & V_{dk} & V_{dk} & V_{dk} & V_{dk} \\ \phi_{k1} & 0 & V_{dk} & \epsilon_{k1} + V_a & 0 & 0 & 0 \\ \phi_{k2} & 0 & V_{dk} & 0 & \epsilon_{k2} + V_a & 0 & 0 \\ \phi_{k3} & 0 & V_{dk} & 0 & 0 & \epsilon_{k3} + V_a & 0 \\ \phi_{k4} & 0 & V_{dk} & 0 & 0 & 0 & \epsilon_{k4} + V_a \end{pmatrix} \quad (5.11)$$

The on-diagonals of both the whole matrix, and the acceptor sub-matrix, con-

tain all the electronic and vibrational information. Each acceptor site, ϕ_k , couples vibronically to the donor state, ϕ_d , via the off-diagonal V_{dk} parameter.

The effect of nuclear motion on the dynamics of this electron transfer process can be considered from two different, but theoretically equivalent, approaches. The first approach of vibronic coupling, called the normal mode approach, couples all the vibrational DOF to the electronic states in the same way, and is described by the Hamiltonian shown below, showing only the vibronic coupling and omitting the donor-acceptor coupling,

$$H_N = T + \frac{1}{2} \sum_l [\omega_l Q_l^2 - |\phi_d\rangle 4c_l Q_l \langle \phi_d|], \quad (5.12)$$

where T is the kinetic energy, and Q_l is the position of the l th normal mode, of frequency ω_l , and the c_l specifies the vibronic coupling term. These vibrational modes can represent both the intramolecular modes of the dye molecule, as well as any surrounding solvent or bath modes. The coupling parameters, c , can be determined by the spectral density,

$$J(\omega) = \frac{\pi}{2} \sum_l \frac{c_l^2}{\omega_l} \delta(\omega - \omega_l). \quad (5.13)$$

This spectral density describes the response of the solvent polarisation to the change of the charge distribution upon excitation or ionisation to the excited state or cationic state, respectively.

However, if all 102 normal modes of the dye were considered, without even taking the semiconductor into account, this is beyond the ability of the MCTDH method. Therefore a different approach is needed here.

This leads to the second approach implemented to couple nuclear motion with the electronic states selects only the few vibrational modes which are most significant to the electron transfer process. This is called the reaction coordinate approach. The remaining "insignificant" modes can be combined into a harmonic

bath. The nuclear Hamiltonian for this approach is simplified to,

$$, H_N = H_S + H_B + H_{SB} \quad (5.14)$$

where H_S is the system Hamiltonian and H_B is the bath. The bath-system coupling, H_{SB} , is determined, as in the normal mode approach, by a spectral density. The system Hamiltonian has a similar form to that used in chapter 4 for allene, where:

$$H_S = T + \frac{1}{2} \sum_l \omega_l Q_l^2 + \sum_l |\phi_d\rangle \kappa_l^d Q_l \langle \phi_d| + \sum_l \sum_k |\phi_k\rangle \kappa_l^a Q_l \langle \phi_k|, \quad (5.15)$$

where the few most significant modes, along coordinates Q_l , have vibronic coupling parameters of κ_l^d and κ_l^a , depending on whether the coupling to the donor state or the continuum of acceptor states is considered, respectively. These vibronic coupling parameters are related to the reorganisation energy by $\lambda_l = \frac{(|\kappa_l^d - \kappa_l^a|)^2}{2\omega}$. These parameters have already been discussed in more detail in section 5.4.

The remaining vibrational modes of the dye molecule are represented as a bath of harmonic oscillators,

$$H_B = \tilde{T} + \frac{1}{2} \sum_j \tilde{\omega}_j \tilde{Q}_j^2, \quad (5.16)$$

where $\tilde{\omega}_j$ and \tilde{Q}_j^2 are the frequencies and reaction coordinates of the bath modes, respectively. The system-bath coupling is characterised by a spectral density, which is the same as in the previous approach, shown in equation 5.13.

Assuming the wavepacket starts the propagation in the donor state by application of an ultra-short laser pulse, the population decay of the donor state can be calculated and plotted to determine the dynamics of the electron injection process from the donor state into the conduction band of TiO_2 .

Although I will discuss the results of using this method in this next section, as research and time progressed it became apparent that this method of modelling a dye to semiconductor electron injection was incorrect. Therefore, the failings of this method will be highlighted, and a new method was devised which is discussed in section 5.9.

5.8.2 Initial Results

Initially using the vibronic coupling constants from the research reported by Kondov et al [123], the Hamiltonian was set up, and the propagation run. With 102 normal modes, it was beneficial for the preliminary propagations to identify the key modes that are important to this charge transfer. Of all these modes, ν_{83} and ν_{85} were deemed to be the most active. This is due to the conclusion drawn in the publication mentioned above that only the highest frequency modes will have an effect on electron dynamics due to the ultrafast electron injection. Of the highest frequency modes published in the paper, ν_{83} and ν_{85} had the largest coupling strength, table 5.3.

Mode	ω (cm ⁻¹)	κ^d (cm ⁻¹)	κ^a (cm ⁻¹)	Coupling Strength
ν_{83}	1534	563	86	0.05
ν_{85}	1612	-863	10	0.15

Table 5.3: Parameters taken from the results reported by Kondov et al [123]. The κ values were reported in mass-scaled units, thus the κ parameters presented here are not directly comparable to the κ parameters calculated later on in this chapter.

The primitive basis set was chosen using a harmonic oscillator DVR and the propagation was converged with respect to the population decay of the donor state. In order to converge the results, the number of states in the acceptor continuum was increased until the population decay of the donor state remained stable. If too few electronic states were included in the calculation, due to the nature of the grid-based method, the nuclear wavepacket would "bounce" off the edge of the electronic grid during the time of the propagation. This means that although

including more states would not stop the wavepacket ultimately bouncing back, it would not do so in the time frame of the propagation. The size of this grid is set by the number of the DVR functions used to describe each DOF. The wavepacket began the propagation on the donor state at the ground state equilibrium geometry. It can be seen from figure 5.12 that there was almost complete population transfer into the continuum of states after 50 fs if 1499 states were included in the acceptor continuum.

As only two of the vibrational modes are included in this propagation, the wavepacket oscillates between the two states for the rest of the calculation, due to the lack of a vibrational bath. If more vibrational modes are introduced into the Hamiltonian, the energy of the wavepacket would dissipate into the conduction band acceptor states, and there would be no back charge transfer. This is shown in figure 5.13.

Again the vibrational modes chosen to be included are based on their coupling strength to both the donor and acceptor states, listed in table 5.4.

Mode	ω (cm ⁻¹)	κ^d (cm ⁻¹)	κ^a (cm ⁻¹)	Coupling Parameter
ν_7	133	-265	2283	1.17
ν_{14}	312	1289	-4698	0.77
ν_{21}	452	3168	-5017	0.60
ν_{35}	758	7626	-1459	0.31
ν_{49}	1026	7944	-11211	0.41
ν_{55}	1151	5157	10415	0.10
ν_{56}	1172	11229	3355	0.14
ν_{66}	1321	4616	-17337	0.32
ν_{72}	1360	-12170	9920	0.31
ν_{83}	1534	22051	3368	0.22
ν_{85}	1612	-34649	401	0.38
ν_{87}	1795	16396	-17244	0.31

Table 5.4: All parameters are taken from the results reported by Kondov et al [123]. The κ values here were all reported in mass-scaled units, so have been converted to mass-frequency scaled units.

These dynamics were run using a contracted multi-set basis, shown in table

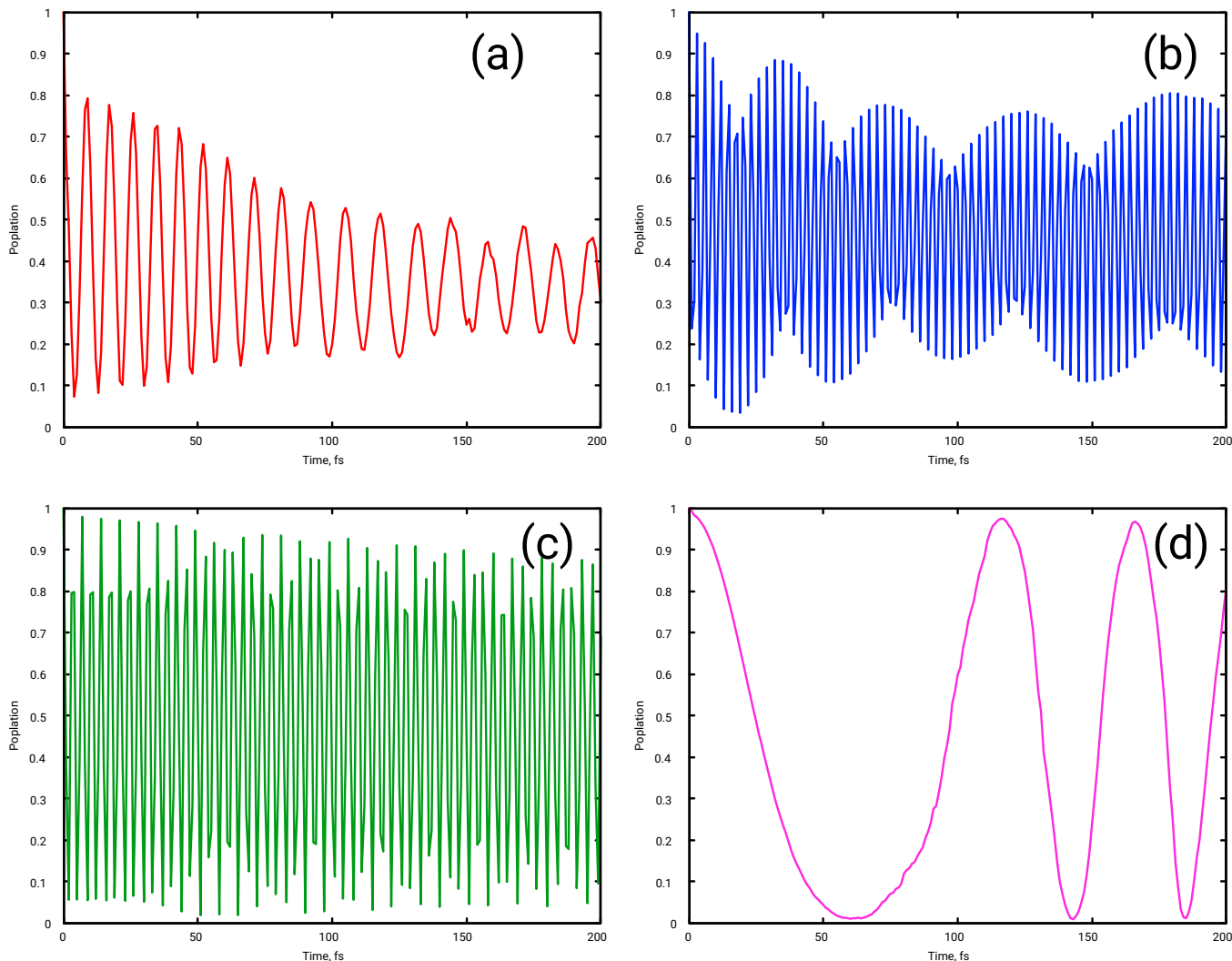


Figure 5.12: The diabatic population of the donor state of the C343-TiO₂ system, with increasing number of states in the acceptor continuum of (a) 101 states (b) 501 states (c) 1001 states (d) 1499 states. These dynamics were run using 5 SPFs for both ν_{83} and ν_{83} t in both the donor and acceptor state.

5.5.

As mentioned at the start of this section, these calculations were all run using the vibrational parameters reported by Kondov et al. This was in order to test the method, and to ensure that the results reported could be replicated. Despite using all the same parameters, the results in the paper could not be replicated. To find out why this was, and to investigate the system further, the next step would

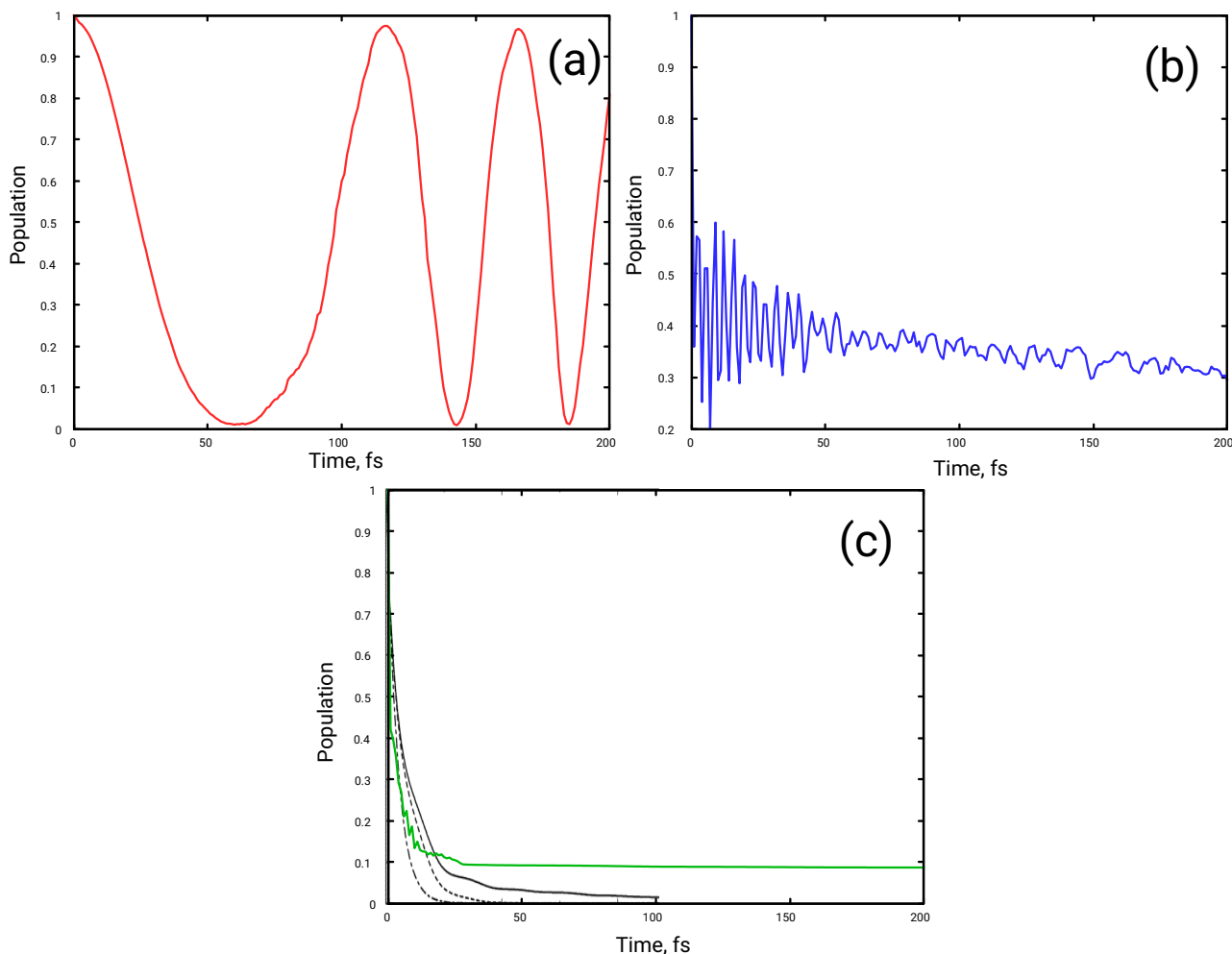


Figure 5.13: The diabatic population of the donor state of the C343-TiO₂ system, including more vibrational modes into the dynamics of the calculation. (a) 2 modes, as repeated from figure 5.12, ν_{83} and ν_{85} (b) 6 modes, ν_7 , ν_{14} , ν_{21} , ν_{83} , ν_{85} and ν_{87} (c) 12 modes, as shown in table 5.4. This is compared to the decay plot from the literature [123]

be to replicate the results using the vibrational frequencies and κ values obtained via the electronic structure calculations done by us on Coumarin-343 .

Number of modes	Contracted basis set	Number of SPFs in donor state	Number of SPFs in acceptor state
2	v83 v85	5	5
6	v7,v14,v21 v83,v85,v87	5	5
12	v7,v14,v21 v83,v85,v87 v56, v66, v72 v35, v49, v55	9	9

Table 5.5: All parameters are taken from the results reported by Kondov et al [123]. The κ values were reported in mass-scaled units, so have been converted into mass-frequency scaled units.

5.8.3 Further Investigations

The starting point was to repeat the first calculations of the previous section, including just 2 DOF. The calculations performed identified a different set of significant modes to the electron transfer as Kondov et al did in their paper. This is due to the difference in κ values obtained from the TDDFT calculations. These are shown in table 5.1. For these preliminary 2D calculations, ν_6 and ν_7 were used. The results of this calculation will not be included as they offer no further information and figure 5.12 accurately enough represents the results of this, i.e. including different modes has no effect on the dynamics. However, when an increased number of electronic states were added, beyond, 1499, an odd trend was observed. The assumption was that the results had converged with respect to the population plot when including 1499 states in the continuum, and that adding more would not change the dynamics further. This assumption was incorrect. Upon including more states, 2499 acceptor states, the decay of the donor state became less smooth again, figure 5.14.

This result was unexpected and in fact, created more questions than it answered. Why should this be? Further investigations showed that only by including exactly 1499 states in the acceptor continuum was the decay plot of the donor

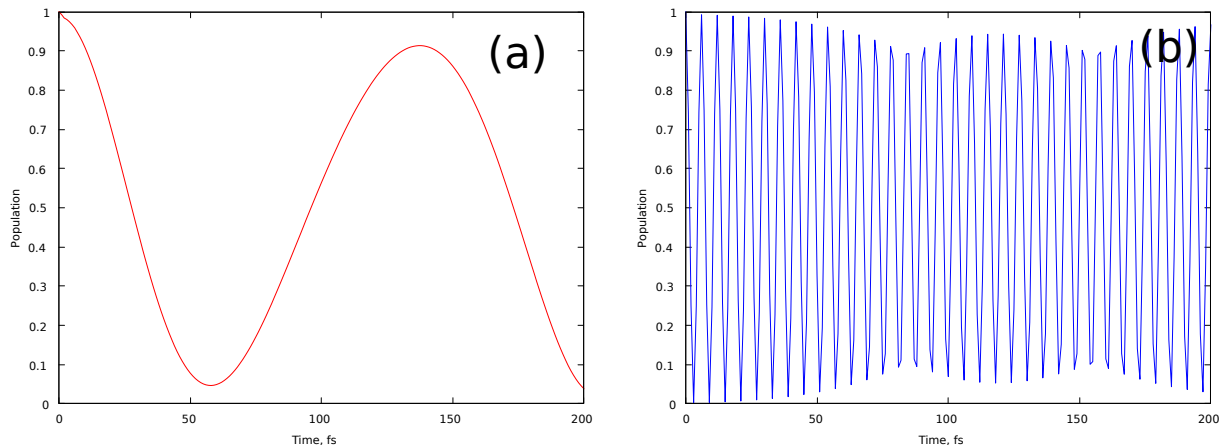


Figure 5.14: The diabatic population of the donor state of the C343-TiO₂ system, with (a) 1499 states and (b) 2499 states in the acceptor continuum. These dynamics were run using 8 SPFs for both ν_6 and ν_7 in both the donor and acceptor state.

state smooth, resembling that of the results published in the reference paper. The next pertinent question now, of course, was why was 1499 this "magic number" of states?

The first thing to check was that it was not the electronic and vibrational parameters that we had calculated ourselves (table 5.1 in section 5.4), rather than using those that Kondov et al had published, as in the previous section. However, adding more states into the continuum, but using Kondov's parameters, generated the same pattern - that as more states are added to the continuum beyond 1499, the decay became "worse", or more oscillatory. This showed that there is an inherent problem with this method, as this should not be the case. The next step now was trying to identify the issue.

The dynamics were stripped back to just the electronic decay only, removing any vibronic coupling that was included. This was to exclude the vibronic Hamiltonian implemented as being the issue here. The same problem as just described persists with the electronic state only dynamics, with this "magic number" of states. Therefore, the issue is with the electronic structure parameters. The

Hamiltonian of the electronic dynamics is as follows, matrix 5.17. As the wavefunction begins the propagation in the donor state, the ground state does not take part in the dynamics, and it is omitted from here on, for clarity. As above, for simplicity, the acceptor is shown here consisting of 4 states in the continuum.

$$\left(\begin{array}{c|c} \phi_d & \phi_k \\ \hline \phi_d & E_d \quad \mathbf{V}_{\mathbf{dk}} \\ \phi_k & \mathbf{V}_{\mathbf{dk}} \begin{bmatrix} \epsilon_{k1} + E_a & 0 & 0 & 0 \\ 0 & \epsilon_{k2} + E_a & 0 & 0 \\ 0 & 0 & \epsilon_{k3} + E_a & 0 \\ 0 & 0 & 0 & \epsilon_{k4} + E_a \end{bmatrix} \end{array} \right) \quad (5.17)$$

The calculated energies of the first excited state and the ground cationic state, E_d and E_a respectively, are close the literature values [127]. Therefore, it is unlikely that these parameters are the issue. Likewise, the ϵ_k values are just simply equidistantly spaced energy levels in the conduction band of TiO_2 , and so are fixed values. Therefore, the problem must be the V_{dk} electronic coupling parameter. This coupling is defined by the decay function

$$\Gamma(E) = 2\pi \sum_k |V_{kd}|^2 \delta(E - \epsilon_k) \quad (5.18)$$

with

$$\Gamma(E) = \frac{2v_0^2(E - E_0)}{v^2} \sqrt{1 - \left[\frac{(E - E_0) - \epsilon^2 - 2v^2}{2v^2} \right]^2} \quad (5.19)$$

The parameters of this decay function are outlined in a previous section. Of these parameters, the only parameter which is not specific to TiO_2 , and determined by solid state theory, is the v_0 parameter. This determines the coupling between the donor state and the first acceptor site.

This parameter was currently set at 4000 cm^{-1} , as per the reference paper, which equates to roughly 0.5 eV. This is a very strong coupling.

By changing the v_0 and determining how this affects the dynamics, the hope was that this would help identify some issues. Arbitrarily choosing 500 states in the continuum as a test, the v_0 parameter was set to a different values, ranging from the original $0.5 \text{ eV} \rightarrow 0.05 \text{ eV}$. The results of this can be seen in figure 5.15.

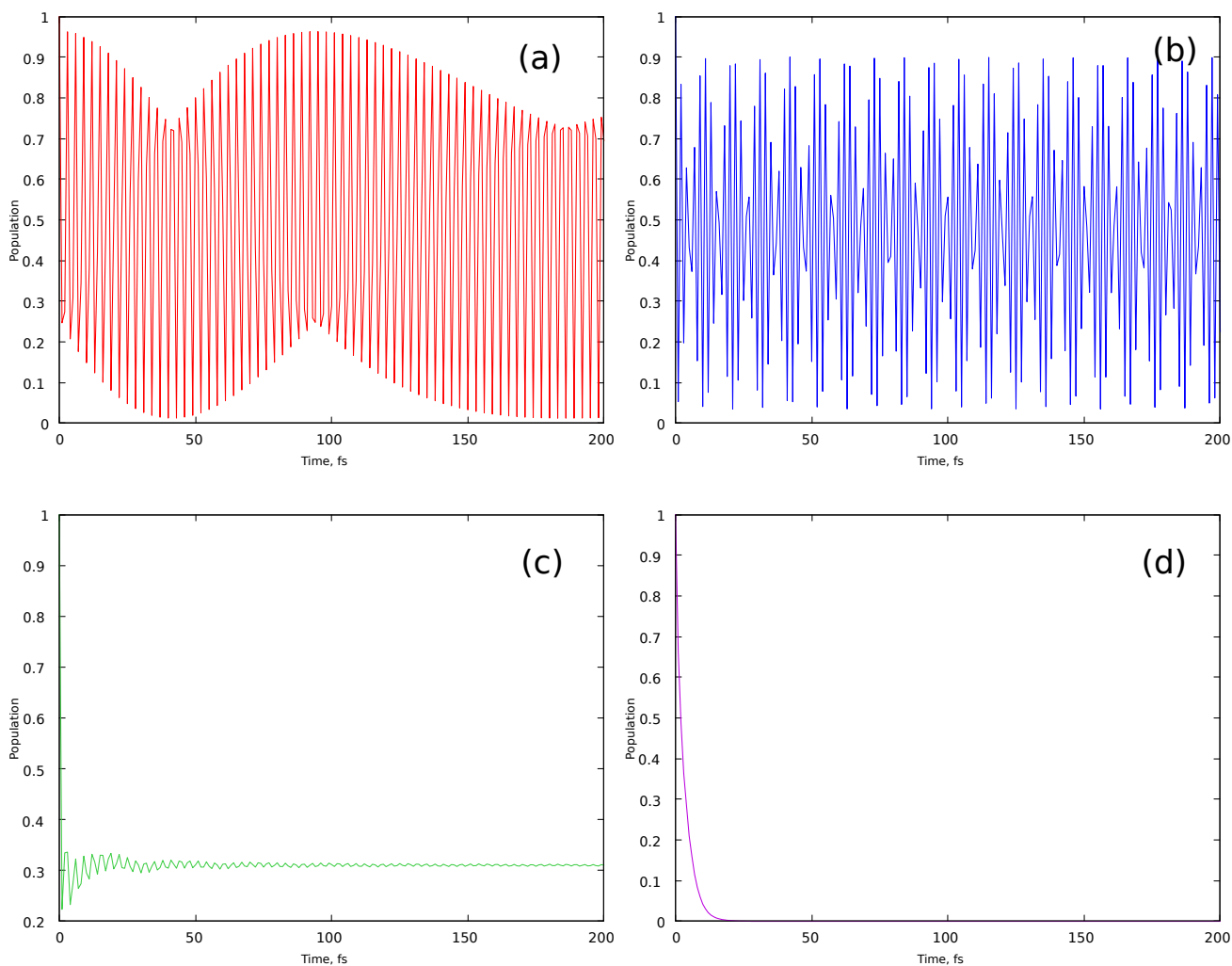


Figure 5.15: The diabatic population of the donor state of the C343-TiO₂ system, at various coupling strengths, with (a) $v_0 = 0.5 \text{ eV}$ (b) $v_0 = 0.3 \text{ eV}$ (c) $v_0 = 0.1 \text{ eV}$ and (d) $v_0 = 0.05 \text{ eV}$. These dynamics were run using electronic dynamics only, with 500 states in the continuum.

The results of this investigation into the effect of changing the v_0 parameter clearly show that the $v_0 = 0.5 \text{ eV}$ set in the paper is much too high, as predicted. In fact, the v_0 parameter must be decreased by a factor of 10 before the population

decay of the donor state replicates that seen in the Kondov paper.

Due to all the unexpected issues with using this method, the approach as to how the decay function calculates the v_{dk} values was scrutinised. v_0 is the only parameter which contains information about the dye molecule, as all other parameters in the decay function are semiconductor specific. The original paper which devised this decay function [136] sets this value to 1 eV, which is then already halved for the Kondov et al paper. This already indicates that there is some inherent problem. Whilst looking at this decay function further, it became apparent that this function had been misinterpreted, both in our studies, and in the series of papers by Kondov et al. It was believed to be a function in which one could input the energy of the donor state, and get out the V_{dk} coupling parameters. However, this equation (equation 5.19) is actually a calibration of donor state energy and electron injection time, i.e. by measuring the time scale of the electron transfer, one can determine the energy of the donor state. This means that this method is not suitable for specifying the coupling used when calculating dynamics. As the research of Kondov et al progressed further, they too ended up changing their whole approach to calculating the dynamics of the system, adding further credence that this approach is not the correct way forward.

5.9 Dynamics II

5.9.1 The Hamiltonian

A new approach to determining the electron dynamics of the system was needed. Taking the previous method as inspiration, the 1-dimensional chain was, once again, implemented.

This representation is similar to the first method, as shown in figure 5.11 in the previous section, but with a few key differences. The main difference is the β' couples the donor state to the first acceptor site only, with the β coupling term

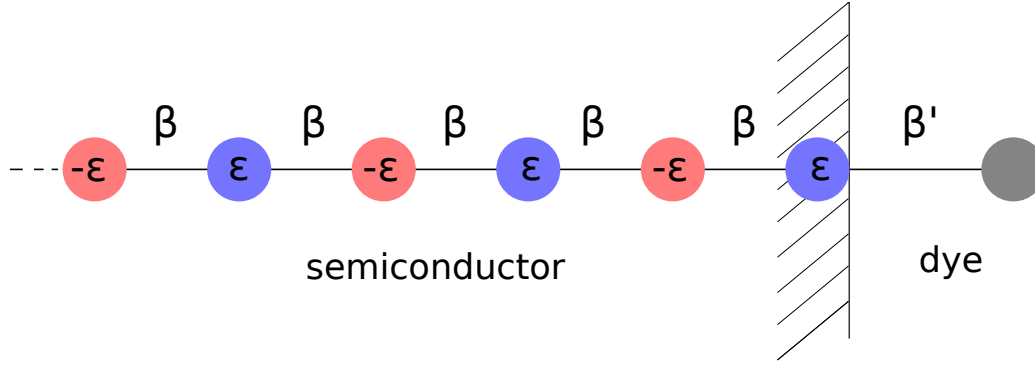


Figure 5.16: A schematic of the dye-semiconductor system, showing the parameters of the new dynamics method.

coupling the nearest acceptor sites. This is shown below in matrix form, matrix 5.20. As before, only 4 states are shown in the acceptor continuum for simplicity.

$$\begin{pmatrix}
 & \phi_d & \phi_{k1} & \phi_{k2} & \phi_{k3} & \phi_{k3} \\
 \phi_d & E_d + \kappa & \beta' & 0 & 0 & 0 \\
 \phi_{k1} & \beta' & \epsilon + \kappa & 0 & 0 & \\
 \phi_{k2} & 0 & \beta & -\epsilon + \kappa & \beta & 0 \\
 \phi_{k3} & 0 & 0 & \beta & \epsilon + \kappa & \beta \\
 \phi_{k3} & 0 & 0 & 0 & \beta & -\epsilon + \kappa
 \end{pmatrix} \quad (5.20)$$

The ϵ and β parameters, as in the previous method, are taken from the Petersson et al paper [136], which were derived from solid state theory. These are set at $\epsilon = 1.6$ eV, and $\beta = 2$ eV. The E_d represents the energy of the donor state, with respect to the bottom of the conduction band, and is set at 3.2 eV. If the acceptor sub-matrix is diagonalised, one can find the eigenvalues of the acceptor continuum. This diagonalisation results in the following band structure for the TiO_2 in this system, figure 5.17.

The valence band and the conduction band can clearly be seen, showing a band

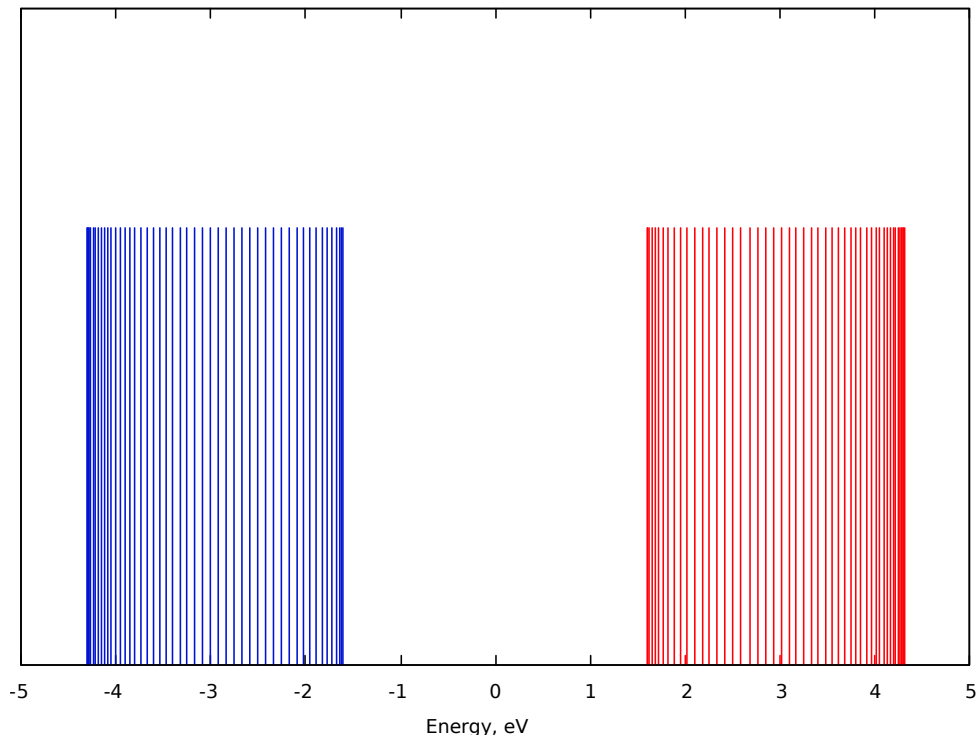


Figure 5.17: The diagonalised acceptor sub-matrix derives the eigenvalues. There are 100 states in the continuum included here.

gap of 3.2 eV, which corresponds to the parameters in this model.

The additional advantage of using this second approach, is that the model can be easily scaled up from a 1D chain to a 2D slab, or 3D block. The donor state would still couple to only the first acceptor site, but these extended systems would contain more β coupling elements. This is a more realistic description of how the charge spreads out once in the semiconductor. Figure 5.18 shows how this method can be adapted for these bigger systems.

5.9.2 Results

Starting where the previous method failed, the first set of results test the dynamics of the wavepacket in a purely electronic basis set, i.e. without any vibronic coupling.

Using the analogous parameters from the previous method, where $E_d = 3.2$

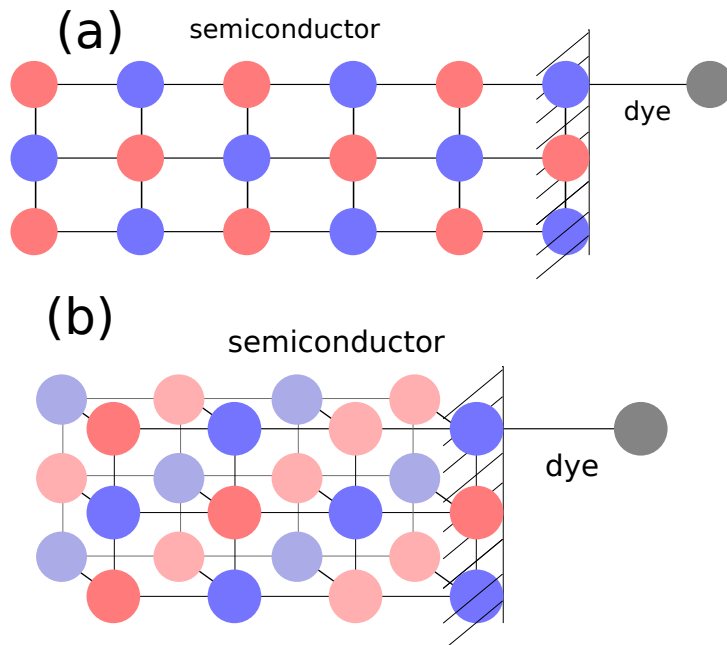


Figure 5.18: A schematic showing how the model used can be easily expanded to an (a) 2D and (b) 3D model.

eV, $\beta = 2$ eV and $\epsilon = 1.6$ eV, the dye-semiconductor coupling parameter, β' , was tested. Using the initial guess of 1 eV, which was shown in the previous method to be much too strong, the β' value was decreased in increments to 0.05 eV. The effect of changing this parameter is shown in figure 5.19. For the sake of time considerations for these preliminary calculations, only 50 states were included in the continuum.

The general trend shows that the stronger the coupling, the faster the initial decay, which makes sense. Even with the expectation that the wavepacket will rebound as an insufficient number of states have been included, setting $\beta'=1$ eV and $\beta'=0.5$ eV is too high, and causes the noise seen in plots 5.19(a) and (b). Conversely, $\beta'=0.05$ eV is too weak a coupling parameter, and does not generate a complete donor state decay.

As mentioned at the end of the previous section, the series of papers used to reference a lot of this work also changed their method. Using a later paper [124] to

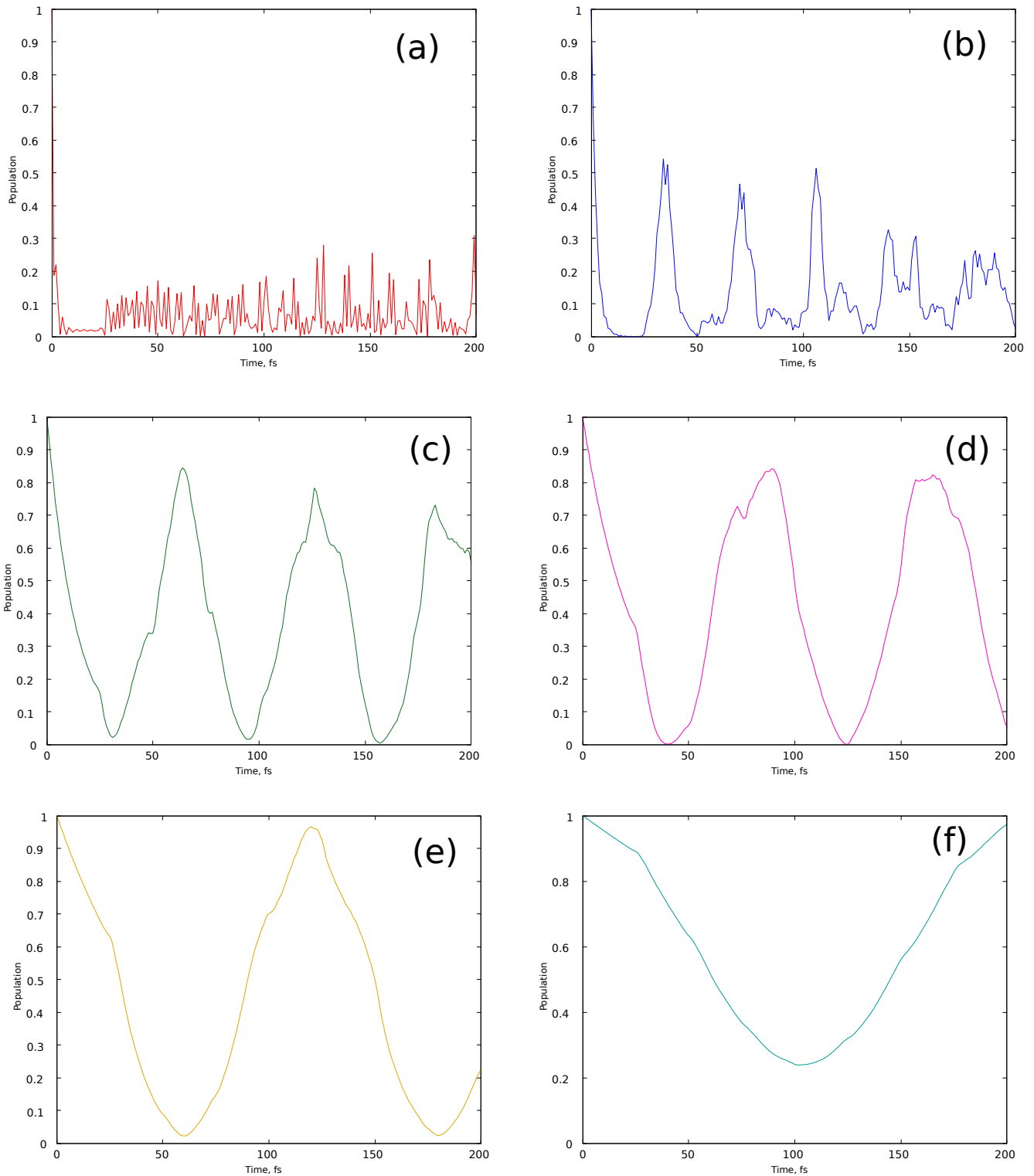


Figure 5.19: The diabatic population of the donor state of the C343-TiO₂ system, testing the effect of changing the β' parameter, where $\beta' =$ (a) 1 eV, (b) 0.5 eV, (c) 0.2 eV, (d) 0.15 eV, (e) 0.1 eV and (f) 0.05 eV.

benchmark results against, it was reported that for electronic dynamics only there was complete donor state population decay after ~ 25 fs. By identifying the β' value which most closely resembles these dynamics from figure 5.19, the β' value of 0.2 eV was chosen. This value was used in all future calculations from here, unless stated otherwise.

Now that the matrix parameters had been determined, the final variable to be finalised was how many states to include in the acceptor continuum before there is no wavepacket rebound observed in the time scale used in the calculations, shown in figure 5.20. Including 500 acceptor states was sufficient for a smooth donor state decay, with no wavepacket rebound effects. Adding more states does not change the dynamics. Therefore, all future calculations will include 500 states in the acceptor continuum, unless stated otherwise.

5.9.3 Adding vibronic coupling

Now that the electronic dynamics have been tested match previously reported data, the next step was to include the vibronic coupling into the Hamiltonian. The expectation was that by including vibronic coupling, vibrational modes will absorb the extra energy and dampen any oscillations. Another expectation was that the donor state will decay slower with the added vibronic coupling, as it is stabilised by the vibronic coupling at short time scales [123].

The effect of adding an increasing number of vibrational modes into the vibronic coupling Hamiltonian was investigated. Beginning with the most active modes, ν_6 and ν_7 , a propagation with 2 DOF was performed. As there are only 2 modes included, this could not be performed using the ML-MCTDH approach. This was followed by the 4D, 9D and 17D ML-MCTDH calculations. The ML-tree diagrams of these calculations are shown in figures 5.21, 5.22 and 5.23, respectively. The groupings of the modes for the ML-trees were based purely off the coupling strength - κ/ω - with similar strengths being grouped together initially, and split

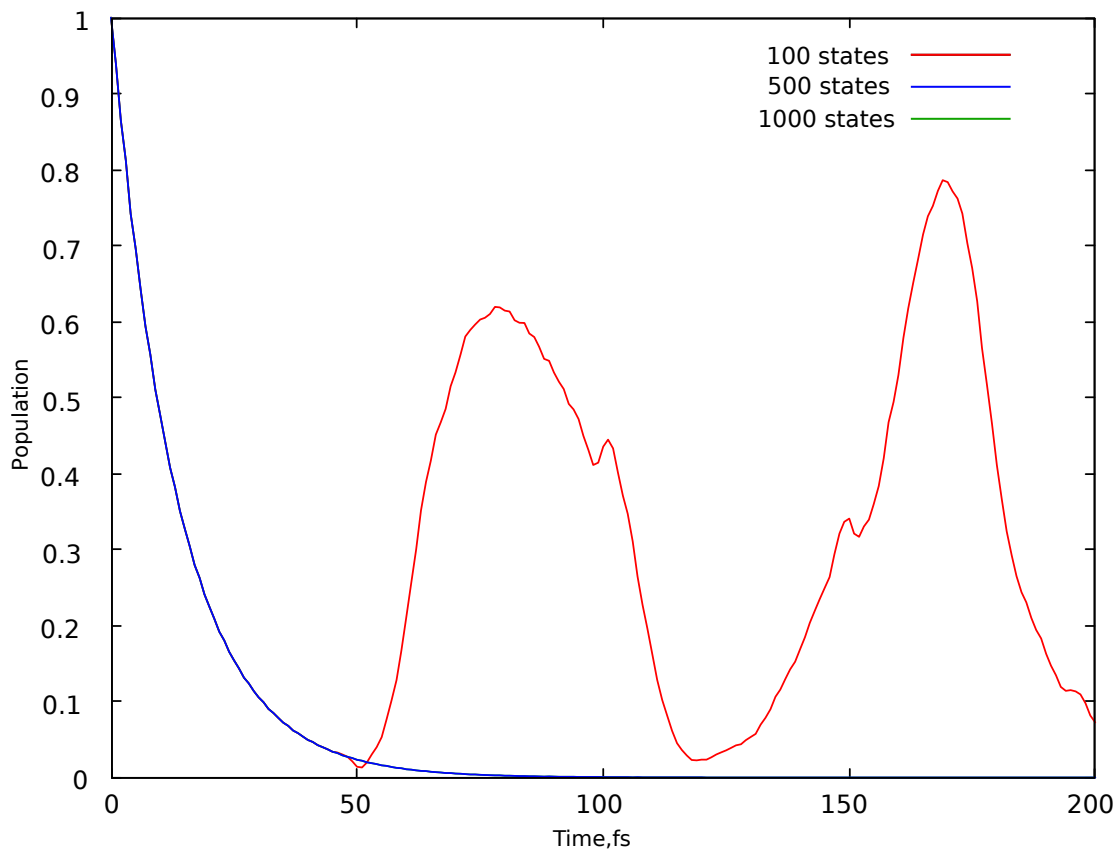


Figure 5.20: The diabatic population of the donor state of the C343-TiO₂ system, testing the effect of changing the number of states included in the acceptor continuum - showing 100, 500 and 1000.

down further into 1-dimensional SPFs.

The results of these propagations are shown in figure 5.24.

It can be seen from figure 5.24 that including vibronic coupling into the model does not affect the dynamics significantly. In fact, despite the prediction that the decay would be slower after the inclusion of vibronic coupling, the plot with 17 modes decays marginally quicker than the others. This complete contrast to the expected results called for further adaptations to the model.

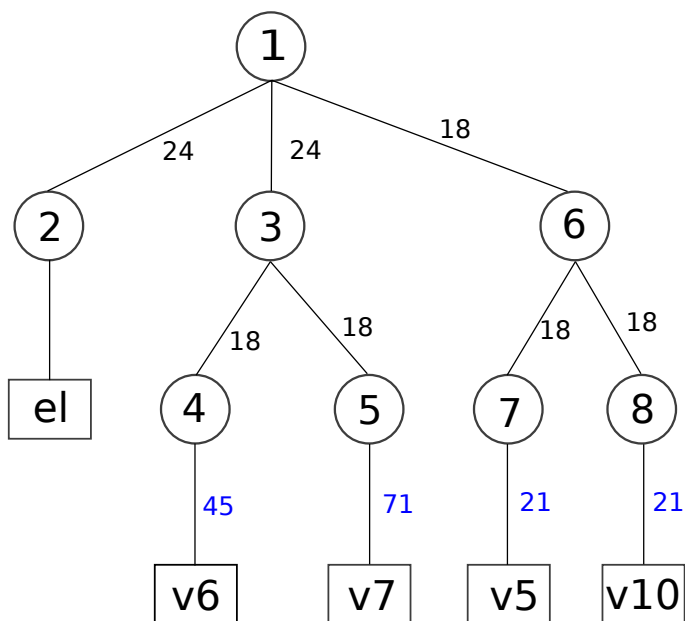


Figure 5.21: The ML-Tree diagram for 4D system, with the node number shown in the circles. The number of basis functions is shown in black, and the number of DVR grid points per DOF is shown in blue.

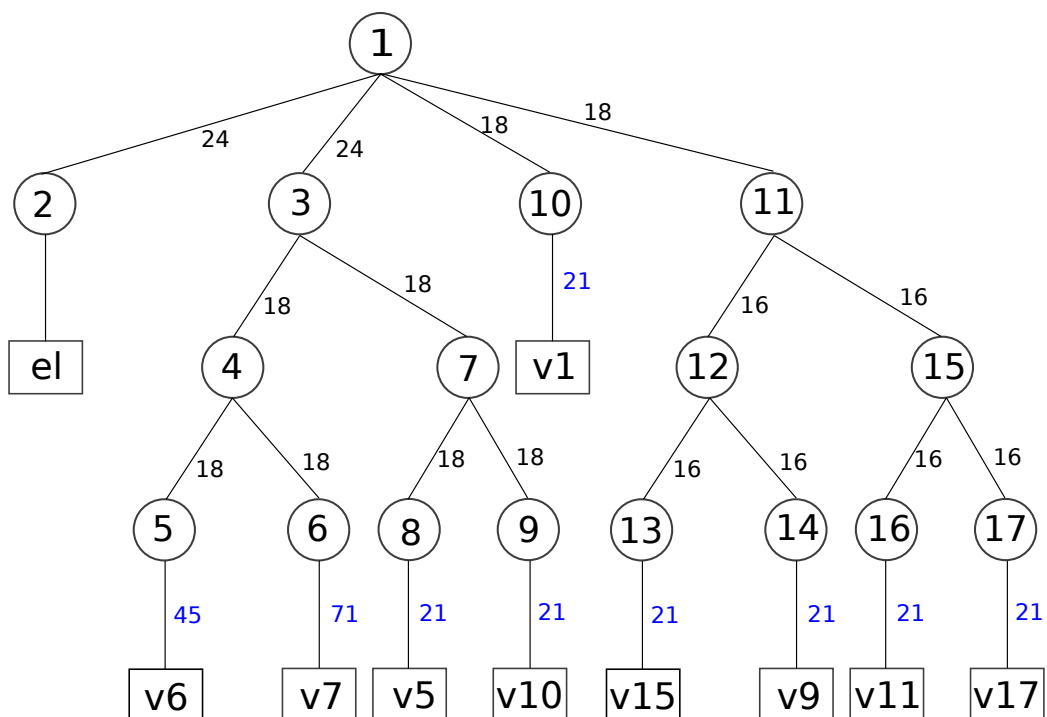


Figure 5.22: The ML-Tree diagram for 9D system, with the node number shown in the circles. The number of SPF basis functions is shown in black, and the number of DVR grid points per DOF is shown in blue.

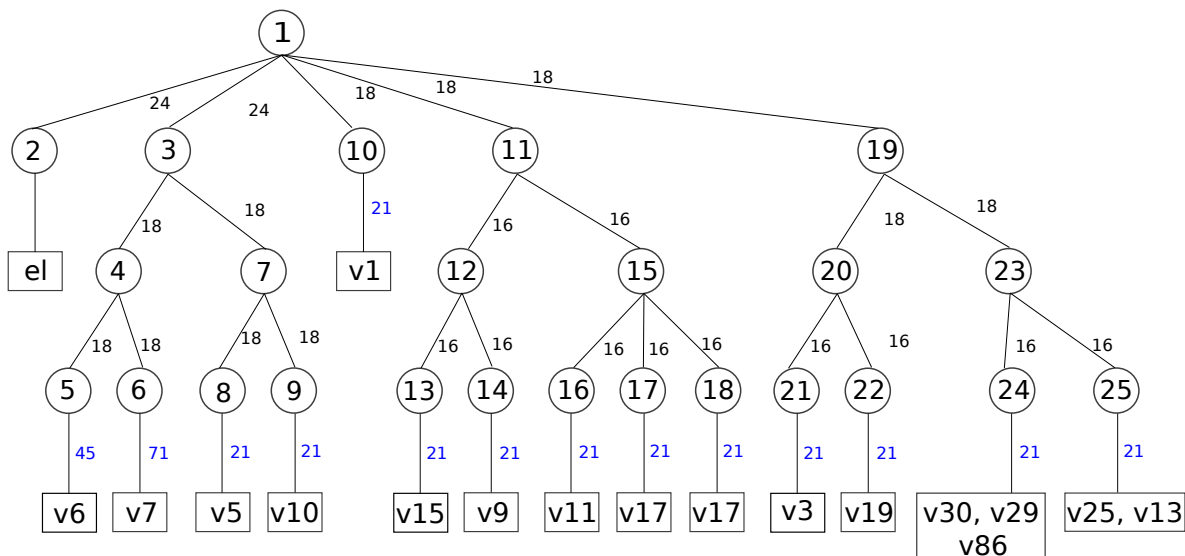


Figure 5.23: The ML-Tree diagram for 17D system, with the node number shown in the circles. The number of basis functions is shown in black, and the number of DVR grid points per DOF is shown in blue.

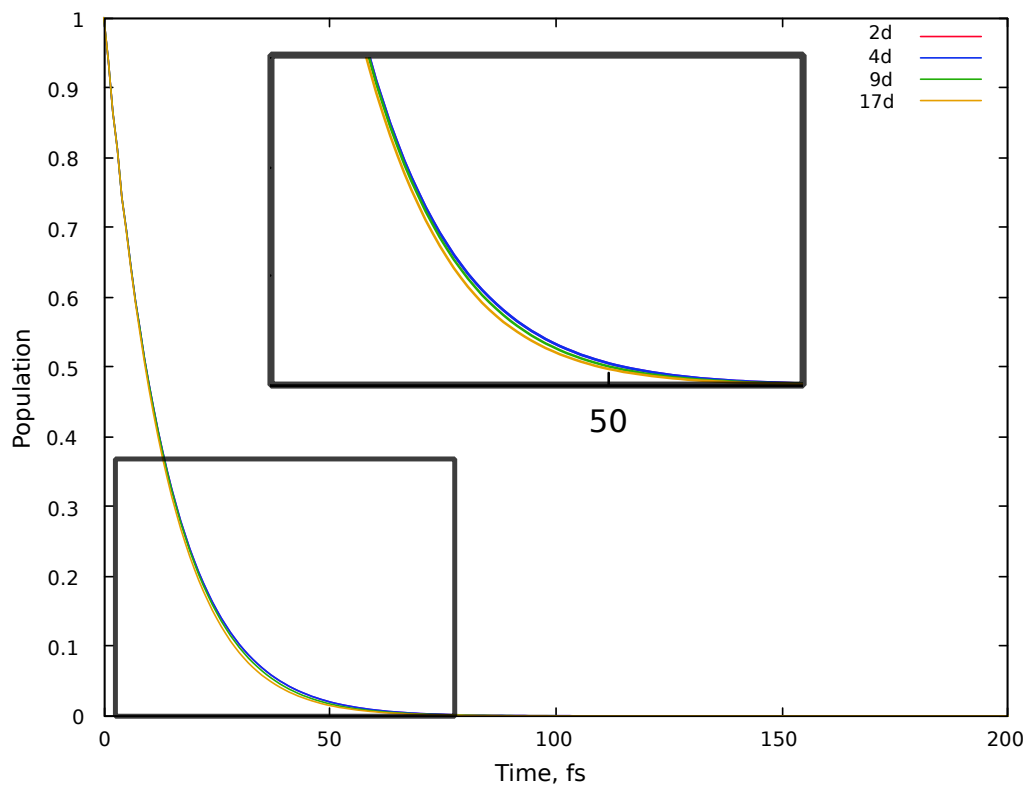


Figure 5.24: The diabatic state population of the donor state showing the decay of the donor state with 2, 4, 9 and 17 modes. The inset shows the magnification of the plot from 0 - 70 fs for clarity

5.9.4 The β' Parameter

So far, in this second approach to the dynamics, the β' parameter coupling the dye to the semiconductor has been static. It has been set to 0.2 eV. This is quite a strong value, and a factor that may be causing the lack of change of the dynamics. The transfer of population is so fast that nuclear motion is not quick enough to affect it. Also, the value of 0.2 eV has only been achieved by benchmarking it to previously reported results. In order to approach this value more analytically, one needs to consider how this parameter arises. As mentioned in section 5.6, the overlap between the donor orbital and acceptor orbital gives rise to this parameter. With this in consideration, it becomes apparent that this coupling parameter should be a dynamic coupling parameter, rather than the current static one. As the bonds which adsorb the dye to the semiconductor surface stretch and contract, so too will the orbital overlap between donor and acceptor change.

To determine what these vibrations are, and thus determine the dynamic coupling parameter value (which will now be termed λ), a vibrational analysis was performed on the small C-343-TiO₂ complex, consisting of a TiO₂ dimer. As described in the previous chapter, this off-diagonal λ coupling parameter is defined by,

$$\lambda_{\alpha}^{ij} = \frac{\partial}{\partial Q_{\alpha}} \langle \phi_j | H_{el} | \phi_i \rangle, \quad (5.21)$$

where this λ denotes the coupling between diabatic states ϕ_i and ϕ_j , for mode α .

The vibrations which most closely resemble the symmetric and asymmetric stretch of the bonds adsorbing the dye to the TiO₂ surface were identified. These are summarised in table 5.6.

These additional modes were added into the model, with the anti-symmetrical

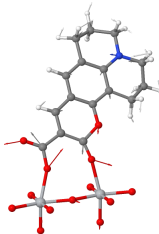
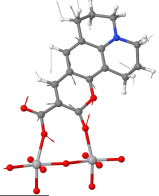
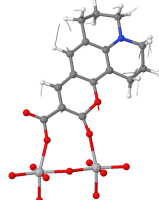
Mode	Stretch	Frequency (cm ⁻¹)	
48	anti-symmetrical	428	
58	anti-symmetrical	610	
72	symmetrical	895	

Table 5.6: The anti-symmetrical and symmetrical stretches of the C-343 - TiO₂ complex.

stretch on the off-diagonal coupling matrix site, and the symmetrical stretch as an on-diagonal tuning mode. The symmetrical mode, ν_s was approximated to 900 cm⁻¹, and the anti-symmetrical mode, ν_a , was an approximated average of the two identified modes at 500 cm⁻¹.

Using these frequencies to construct a pseudo-vibronic coupling Hamiltonian, the values of the λ parameter for the ν_a mode, and the κ values for the ν_s were tested. The κ^a and κ^d values were set to the same value initially, a value of ± 0.1 eV, in order to optimise λ independently. Testing a range of λ values, from 0.1 \rightarrow 0.5 eV, the dynamics of the donor state decay were plotted, figure 5.25.

From these results, and from comparing to other reported decay timescales [123, 124, 128], $\lambda = 0.4$ eV most closely simulates a decay on the correct time scale. Thus future calculations will use $\lambda = 0.4$ eV.

As the modes selected are pseudo-modes, as in not true vibronic modes of the dye, there are no calculated κ values associated with them. Therefore, the next step was to determine sensible $\kappa^{d/a}$ parameters. A range of both κ^d and κ^a values

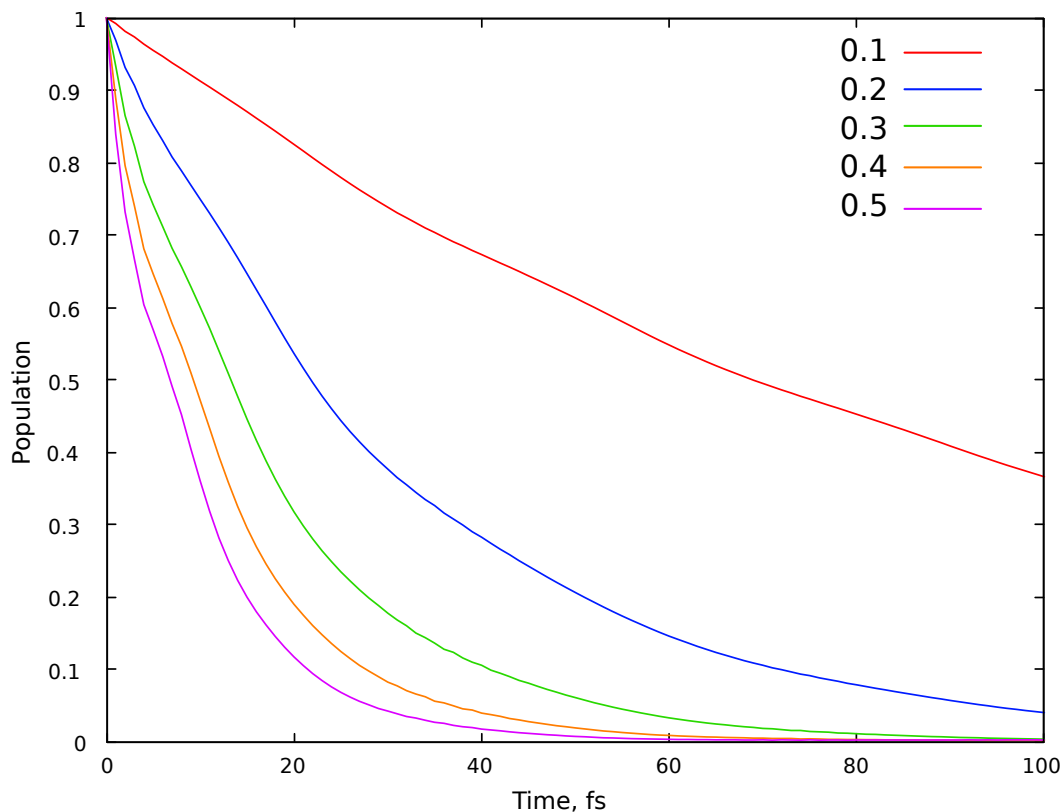


Figure 5.25: The diabatic state population of the donor state showing the decay of the donor state with a $\lambda = 0.1 \rightarrow 0.5$ eV, with a $\kappa^d = \kappa^a = \pm 0.1$ eV.

were tested, ranging from $-0.1 \rightarrow -0.5$ eV for κ^d and between $0.1 \rightarrow 0.5$ eV for κ^a . For the sake of clarity, not all 25 plots of these κ combinations will be included, only the ones of interest. The results of these are shown in figure 5.26.

Again, the κ parameters were narrowed down to which most closely resembled previously reported decay dynamics on this system, and the most optimal parameters were chosen. All of the plots in figure 5.26 replicate the ultrafast initial decay observed in reported data, followed by the quenching by the vibronic coupling. Setting $\kappa^d = -0.5$ eV (the blue and orange plots in figure 5.26), gives more complete donor state decay and was chosen as the optimal κ^d from the test calculations performed. The change in dynamics from changing κ^a from 0.4 eV to 0.5 eV was minimal, and so $\kappa^a = 0.4$ eV was chosen, to break the symmetry of the

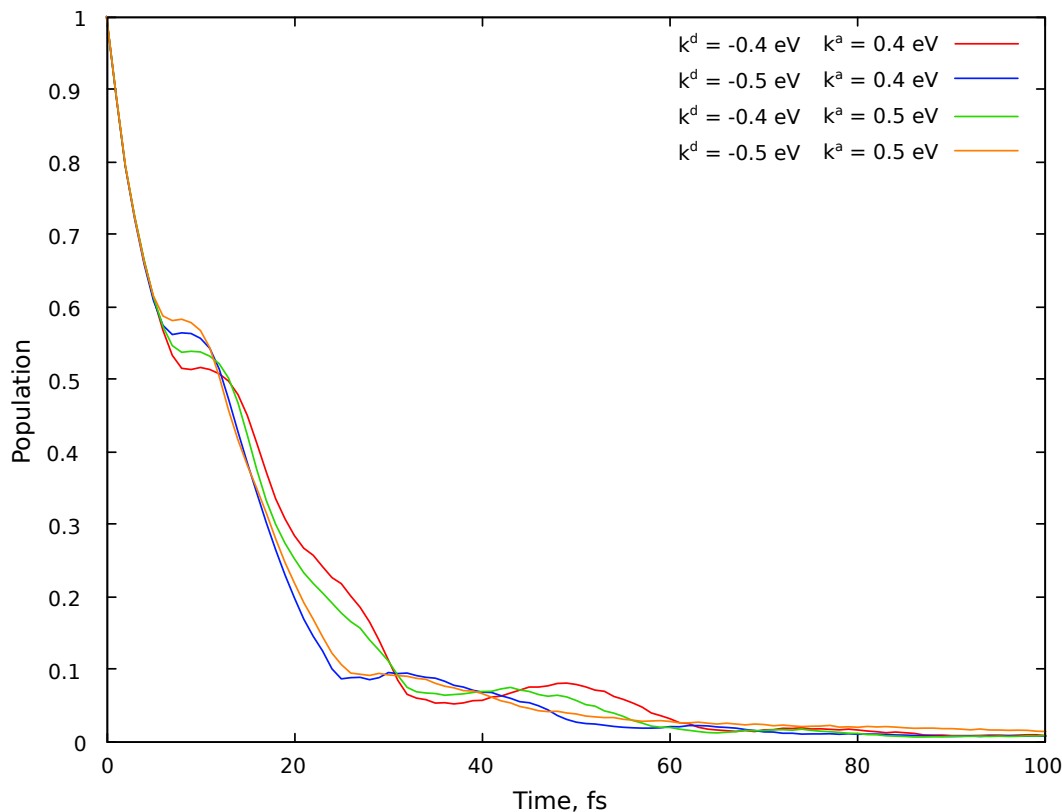


Figure 5.26: The diabatic state population of the donor state showing the effect on the decay of the donor state by altering the κ^d and κ^a parameters.

acceptor and donor states. Therefore, $\kappa^d = -0.5$ eV, and $\kappa^a = 0.4$ eV.

5.9.5 Extending the Model

The next step to further test this model was to add further vibronic coupling, and see the effect on the dynamics of the electron transfer. This was tested first by adding ν_6 and ν_7 , to predict and compare the dynamics in a 3-mode and 4-mode system. The results of this are shown in figure 5.27.

It can be seen from figure 5.27 that there is no significant change in dynamics by adding these extra modes. In order to further explore this issue, a test using 9 modes of vibronic coupling in the system was performed. This was to check that it was simply not an issue of not adding a sufficient number of modes to see a

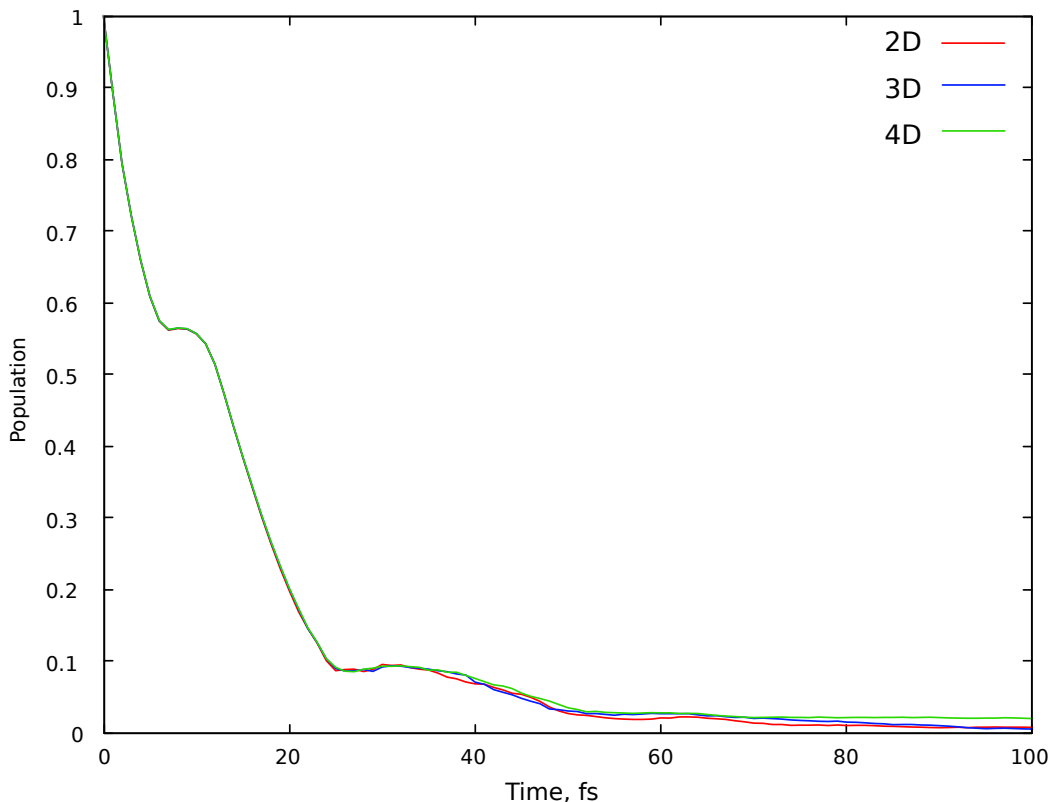


Figure 5.27: The diabatic state population of the donor state showing the effect off adding more vibronic coupling into the model, the 3D system consists of the 2 pseudo-modes of the anti-symmetric and symmetric stretches, and ν_6 . The 4D system has the additional ν_7 modes.

significant change. The results of this 9-modes system are shown in figure 5.28 compared against the 4D system. The ML-MCTDH layer structure for the 9D calculation was the same as the previous 9D calculations, shown as a ML-tree in figure 5.22.

Adding 9 modes of vibronic coupling into the Hamiltonian still has no significant effect on the dynamics of the system. The reasons for this are unclear, but could be due to the parameters of the model. Compared to the pseudo-modes, ν_a and ν_s , denoting the anti-symmetric and symmetric stretch respectively, the κ values of the modes in the system are very weak. This means that there is very little notable change upon the addition of these modes.

Another factor that was considered as to why there is no significant change in

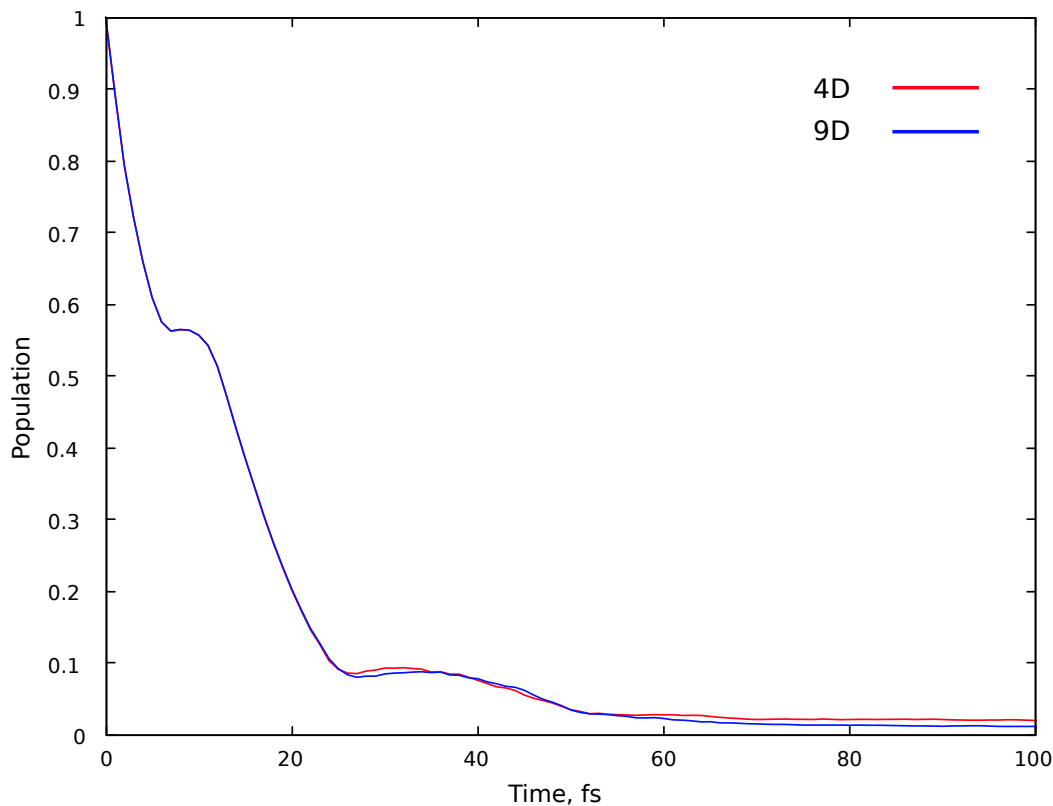


Figure 5.28: The diabatic state population of the donor state showing the effect off adding more vibronic coupling into the model, comparing the 4D and 9D system.

the dynamics is that the coupling between the acceptor states, β , is too strong, relative to other coupling parameters. It is currently set to 2 eV. It is possible that this strong coupling term quickly dissipates the wavepacket along the semiconductor acceptor states before the vibronic coupling terms have time to affect a change in the dynamics. Additional research on this model would look much more closely at all the parameters of the model, calculate the couplings via *ab initio*, and optimise each parameter analytically.

There are a couple of key next steps in which this model could be expanded if research were to continue. The first would be to extend the model to the 2D slab and 3D block, as discussed in section 5.9.2. This would give additional insight into how the semiconductor parameters, namely β , affects the dynamics of the donor state decay. By expanding on this knowledge, more insight could be gained as

to why there is minimal change upon addition of vibronic coupling in the current model.

The next key step in extending this model is to include temperature effects. As this system ultimately aims to simulate the quantum dynamics of a dye-sensitised solar cell, DSSC, the current model is not a fully realistic model. Thus far, all the calculations discussed in this thesis so far have been performed at 0 K. Whilst this is helpful to understand the pure quantum behaviour of the systems, this is not the real working temperature of solar cells. The normal working temperature of solar cells ranges from 283 - 343 K [137, 138], and the effect of temperature on DSSC is not as well studied as other types of solar cell. This means the results so far are varied, with some reports suggesting that efficiency actually improves with a temperature increase [139, 140, 141], which is in opposition to Silicon based solar cells which become less efficient as the temperature rises [142]. One interesting avenue in which temperature effects can be added into the model is by using density matrices. The potential of using density matrices on larger system will be discussed in the next chapter.

5.10 Summary

From looking at the results discussed in this chapter, it is clear that the new model employed is a suitable starting point to capture the donor state decay dynamics of the system. However, it also clear that there is additional research that is required to perfect the model. The lack of effect of vibrational motion on the dynamics of the system is unexpected. Whether this issue lies in the electronic structure of the dye molecule, i.e. the calculated κ parameters, in the dye-semiconductor term, λ , or in the semiconductor parameters determined by the solid state theory is unknown without further investigation.

Another possibility is that not only would including temperature effects in-

crease the reality of the model, but may actually be necessary in observing vibronic effects in the dynamics. Increasing the temperature of the system would introduce more energy into the system, possibly allowing the vibrational motion of the modes to have more of an effect on the dynamics. Further tests on optimising all the parameters in the system, as well as simulating the dynamics at temperatures > 0 K, would help narrow down where the problems lie within this model.

Chapter 6

Salicylaldimine

6.1 Introduction

The previous two chapters in this thesis have investigated the limits of both MCTDH, and ML-MCTDH. Whilst these methods have been successful in predicting charge transfer dynamics in different systems, thus far all systems have been represented as pure states. The wavepacket starts in a well-defined initial pure state and finishes in a pure state. While this holds true for closed-system dynamics at 0 Kelvin, what happens when the systems are open, or at finite temperatures? Understanding and predicting the dynamics of open systems is vital in understanding almost all chemical and biological processes, as no process occurring in nature is truly ever a closed system at 0 Kelvin. Recent studies have shown that temperature effects can play an important role in the quantum dynamics of a system [143, 144, 145]. Wavefunctions are no longer sufficient to describe these systems and density matrices must be used. Density matrices are able to describe thermalisation effects using an incoherent system of statistical mixtures, as detailed in chapter 3.6.

Although the main focus of my research has already been discussed in the previous chapter, in order to simulate the electron transfer process in a real-world environment, one must use density matrices. Solar cells, in which the electron transfer process takes place, clearly do not have working temperatures of 0 Kelvin.

They also occur in a redox medium. In fact, all the currently reported efficiencies of solar cells reported by the National Renewable Energy Laboratory are given under standard conditions, i.e 298 K [146]. Whilst this allows for an easy comparison of different solar cell systems, it is not a realistic way to report efficiencies, as the real working temperatures of solar cells can range from 283 - 343 K [147]. Although the current research into dye-sensitised solar cells, DSSCs, discussed in this thesis is still relatively new, there has been evidence to suggest that unlike in first generation silicon based solar cells, the DSSCs actually increase in efficiency with temperature [139, 140]. Therefore, investigating these systems at working temperatures is critically important. In order to properly simulate this process we need to use a density matrix.

Density matrices have been previously used with MCTDH, termed the ρ -MCTDH method, with success [108, 148, 149]. However, using the ML-MCTDH expansion with density operators has not yet been studied. The computational effort needed for the ML-MCTDH form of the density matrix, discussed in chapters 2 and 3, is that of the ML-MCTDH wavefunction squared. As shown in the previous chapter, the dye-semiconductor system is already at the limits of what the ML-MCTDH method can do, so therefore it is currently computationally infeasible to use density matrices. A smaller, well-known model system will be employed as an initial test of the method.

6.2 Salicylaldimine

Salicylaldimine exhibits a ground state intramolecular proton transfer. Using a pre-computed potential energy surface, PES, of this molecule, the reaction coordinate exhibits an asymmetrical double well. Figure 6.1 shows this potential surface along with the keto and enol tautomers of salicylaldimine .

This potential surface was computed by Polyak et al[150]. Using Hartree-Fock

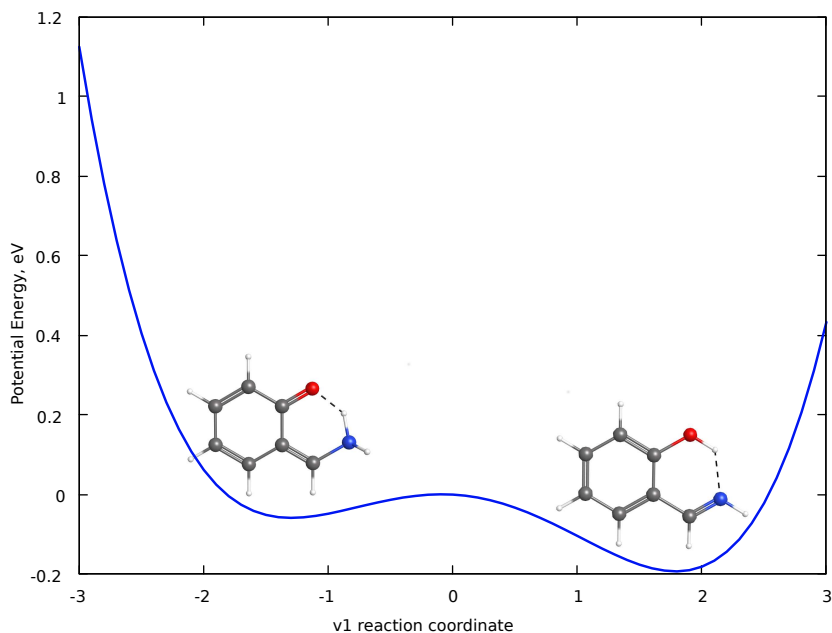


Figure 6.1: The ground state double well potential of the reaction coordinate for the proton transfer in salicylaldimine . The more stable tautomer occurs with the hydrogen on the nitrogen.

theory using a 6-31G* basis set, a set of *ab initio* points were calculated, followed by fitting these points to a polynomial using VCHam.

This asymmetrical double well can be thought of as the adiabatic representation of a 2 state system and therefore lends itself to another model system for a donor/acceptor system, as in the previous chapters. The energy barrier for conversion from the enol to the keto tautomer is 0.19 eV, and 0.06 eV for the reverse. Using Boltzmann's constant, the temperature required to overcome this energy barrier can be calculated,

$$E = (k_B T) * 6.24 \times 10^{18}, \quad (6.1)$$

where k_B is the Boltzmann constant, $1.38 \times 10^{-23} \text{ J K}^{-1}$, and 6.24×10^{18} is conversion factor for eV to J conversion. Converting the 0.19 eV energy barrier into Kelvin, this equates to an energy barrier of approximately 2200 K. It is clear that an external input of energy is required to induce this proton transfer. The less sta-

ble keto-minimum sits in a well with an energy barrier of 0.058 eV, which equates to 673 K.

6.3 Potential Surface

As mentioned in the previous section, the PES was fitted by Polyak et al[150]. In his paper, the 42 normal modes of salicylaldehyde were calculated, and the modes which contributed most significantly to the transition state to the minima transitions were isolated, selecting 13 modes. In this Hamiltonian, as described in chapter 4, the PES takes the form of a Taylor expansion of up to fourth order, where the mass-frequency scaled normal modes are expanded around the transition state geometry, Q_0 ,

$$\begin{aligned}
 V(Q) = V(Q_0) + \sum_{\alpha}^N \kappa_{\alpha} Q_{\alpha} + \frac{1}{2} \sum_{\alpha}^N \omega_{\alpha} Q_{\alpha}^2 + \frac{1}{2} \sum_{\alpha \neq \beta}^N \gamma_{\alpha\beta} Q_{\alpha} Q_{\beta} \\
 + \frac{1}{6} \sum_{\alpha\beta}^N \epsilon_{\alpha\beta} Q_{\alpha} Q_{\beta}^2 + \frac{1}{24} \sum_{\alpha\beta}^N (\iota_{\alpha\beta} Q_{\alpha}^2 Q_{\beta}^2 + \eta_{\alpha\beta} Q_{\alpha} Q_{\beta}^3),
 \end{aligned}
 \tag{6.2}$$

where the Q represents the normal mode coordinates, ω is the frequency and $\kappa, \gamma, \epsilon, \iota$ and η are the polynomial fitting parameters. The parameters of this fitting for the 13 normal modes can be found in the supplementary information for the cited paper. In order to determine which of the 13 modes were the most significant to this proton transfer process, the coupling parameters were calculated. As in chapter 4, this equates to $\frac{\kappa_i}{\omega_i}$, where κ_i is the linear expansion coefficient of mode i , with frequency ω_i . These coupling parameters are shown in table 6.1.

It was determined that the two most significant modes for the proton transfer were ν_1 and ν_{36} , which represent the proton transition mode and the in-plane perpendicular movement of the proton, respectively.

In order to determine the dynamics of the proton transfer, first a relaxation [151] was performed on salicylaldehyde to ensure that the system was in the lowest

Mode	ω (eV)	κ (eV)	Coupling parameter
1	0.18808	-0.01071	0.05694
5	0.05254	0.00008	0.00152
7	0.06644	0.00019	0.00286
9	0.07815	0.00029	0.00371
10	0.07928	-0.00010	0.00126
11	0.09815	-0.00008	0.00082
13	0.10501	0.00009	0.00086
16	0.12166	-0.00001	0.00001
22	0.15213	-0.00004	0.00026
23	0.15954	-0.00028	0.00176
24	0.16244	0.00006	0.00037
32	0.20607	0.00008	0.00039
36	0.26963	-0.00793	0.02941

Table 6.1: The coupling parameters for the 13 most significant modes for proton transfer in salicylaldimine

eigenstate. This process is discussed in upcoming section 6.4. To model the proton transfer dynamics the molecule must first be localised as one tautomer. To obtain a suitable wavefunction, it was thus necessary to approximate the initial state of the nuclear wavefunction as a harmonic oscillator which sits in the lower energy well in the PES along ν_1 . This was done by expanding a new quadratic equation around the PES minimum using the derivatives of the quartic double well.

The form of the PES for this ν_1 mode is of the quartic polynomial form,

$$V = \frac{1}{24}\epsilon q^4 + \frac{1}{6}\iota q^3 + \frac{1}{2}\gamma q^2 + \kappa q + \frac{1}{2}\omega q^2, \quad (6.3)$$

where the fitting parameters are listed in table 6.2, along with the frequency, ω .

Mode	ω (eV)	κ (eV)	γ (eV)	ι (eV)	ϵ (eV)
1	0.18808	-0.01071	-0.38006	-0.06540	0.48662

Table 6.2: The table of fitting parameters for the quartic polynomial for ν_1

This equations expands to,

$$V = 0.020275q^4 - 0.01090q^3 - 0.09599q^2 - 0.01707q. \quad (6.4)$$

Finding the first derivative allows the turning points, and thus the global minimum, to be determined. Setting this equation to 0, and solving for q allows the global minimum to be found, and the quadratic expansion around this point can be determined. This is as follows,

$$\frac{dV}{dq} = 0.08110q^3 - 0.03270q^2 - 0.19198q - 0.01707, \quad (6.5)$$

$$\begin{aligned} \text{when } \frac{dV}{dq} = 0; \quad q = & -1.29691 \\ & -0.09063 \\ & 1.79075 \end{aligned} \quad (6.6)$$

The global minimum is at $q=1.79075$. This can be confirmed by plotting the PES, shown in the previous section, figure 6.1. Finding the second derivative, and substituting $q=1.79075$ then gives the frequency of the new harmonic oscillator around that point,

$$\frac{d^2V}{dq^2} = 0.2433q^2 - 0.0654q - 0.19198, \quad (6.7)$$

$$\text{when } q = 1.79075; \quad \frac{d^2V}{dq^2} = 0.47362. \quad (6.8)$$

Therefore, the quadratic harmonic oscillator frequency, $\omega_0 = 0.47362$ eV. Although this calculated frequency is high when compared to the calculated frequencies of the system, as it is only used for the initial wavepacket relaxation, this is not a problem.

As we do not have any κ parameters to fit this curve, in order to determine the potential of the new quadratic curve the following equation was used,

$$V' = \frac{1}{2}\omega_0(q - q_0)^2 + V_0, \quad (6.9)$$

where q_0 is the new centre, and V_0 is the original potential at q_0 . This can be expanded in order to calculate the energy shift to so that the new curve sits in the

original potential energy well,

$$V' = \frac{1}{2}\omega_0 q^2 - \omega_0 q_0 q + \frac{1}{2}\omega_0 q_0^2 + V_0, \quad (6.10)$$

where the $\frac{1}{2}\omega_0 q_0^2 + V_0$ term is the energy shift. With $w_0 = 0.47362eV$, $q_0 = 1.79075$ and $V_0 = -0.19246eV$, the equation representing the harmonic oscillator can be simplified to,

$$V' = 0.2368q^2 - 0.8481q + 0.5669. \quad (6.11)$$

The approximated harmonic oscillator potential energy surface can be seen in figure 6.2.

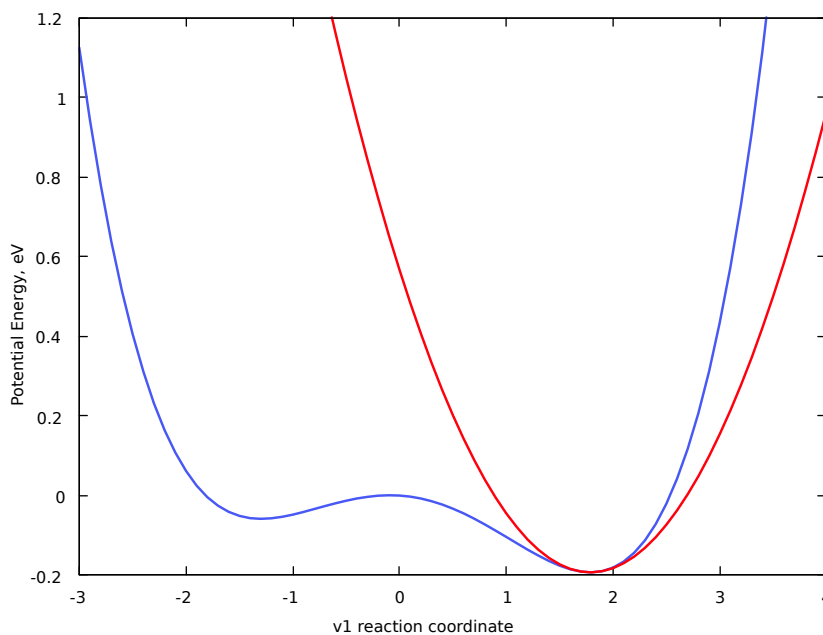


Figure 6.2: The initial state is approximated to be in a harmonic potential which lies in the global minimum of the quartic double well

It can be seen from figure 6.2 that the harmonic approximation holds well for the bottom of well, but as the reaction coordinate moves away from the energy minimum, the approximation becomes less applicable. However, as the harmonic approximation was only used to relax to the lowest eigenstate, i.e. the energy

minimum, it is a good approximation.

6.4 Proton transfer dynamics

The dynamics of all the following results were calculated using the Quantics[112] package. In order to observe the dynamics of the proton transfer, the expectation value of the step operator was plotted. The step function is a projector operating on a wavefunction which allows all parts outside the area of interest to be removed. In this example, a barrier is set at $q=0$, the saddle point of the double well potential. The wavepacket density to the right hand side of the barrier is determined by using the projection operator

$$\theta = |q\rangle\theta(q)\langle q| \quad (6.12)$$

where $\theta(q)$ is the Heaviside step function at the barrier. Here $\theta(q) = 0$ when $x < 0$, and $\theta(q) = 1$ when $q > 0$. The expectation value, P , of this operator is the integral of the wavepacket density from the barrier to the end of the grid, Q . This is the proportion of the system that has crossed to the keto configuration.

$$\begin{aligned} P(q) &= \langle \Psi | \theta | \Psi \rangle \\ &= \int_0^Q \Psi^2 dq \end{aligned} \quad (6.13)$$

The first task before any propagations can take place is the energy relaxation mentioned in the previous section. This relaxation method propagates a wavepacket in imaginary time and renormalised, equation 6.14

$$\Psi(\tau) = \frac{e^{-H\tau}\Psi(0)}{\|e^{-H\tau}\Psi(0)\|} \quad (6.14)$$

where $\tau = -it$. By expanding the wavefunction into a linear combination of eigenstates

$$\Psi = \sum_j c_j e^{-iE_j t} \phi_j \quad (6.15)$$

it can be seen that the eigenstates disappear as $t \rightarrow \infty$, leaving only the lowest eigenstate, i.e the ground state, remaining.

$$\Psi(\tau) = \sum_n c_n e^{-E_n \tau} \psi_n(0) \quad (6.16)$$

Once this relaxation to the ground state energy was calculated, the propagations could begin. These propagations were performed using a variety of methods, to both benchmark and test each approach.

The first method was the standard MCTDH propagation on a simple 2D salicylaldimine system, containing the ν_1 and ν_{36} significant modes. The advancement on this method in previous chapters is that now the thermalised MCTDH method was used, so that the dynamics could be simulated at a non-zero temperature. As mentioned in chapter 3, a thermalised system cannot be expressed as a single wavefunction, i.e a pure state, as the MCTDH method does. The idea of the thermalised MCTDH method is that the incoherent superposition of a thermalised state is described using a randomly generated wavefunction. These wavefunctions all begin at infinite temperature, i.e. equal populations of all configurations but with random phases. The wavefunctions are all then relaxed to the correct temperature, and the resulting set of wavefunctions are propagated in time. Thermalising the MCTDH wavefunction was achieved by setting the length of the relaxation, t_{final} , to

$$t_{final} = \frac{1}{2k_B T} \quad (6.17)$$

where k_B is the Boltzmann constant, and T is the desired temperature. The keyword "thermal = temperature,seed" in the input file of Quantics sets the temperature, T , in Kelvin, and also where the seed for the random number generator is set.

This random number generator sets the random Boltzmann weighted amplitudes of the initial MCTDH wavefunctions[102]. After propagating all the generated wavefunctions, by averaging out the different generated wavefunctions, the final dynamics of the system at that temperature can be determined.

The second method used on this simple 2D salicylaldehyde system was the MCTDH form of the density matrix, ρ -MCTDH. As mentioned previously, density matrices are able to account for all thermal effects as they can represent a system of mixed states. The ρ -MCTDH can be expressed as either the type I or type II formalism. Type I expands the wavefunction into SPDOs, akin to the standard MCTDH expansion. The computational scaling of the type I density matrix is in these SPDOs, and so this method is more efficient for larger systems, and more readily combined with the ML-MCTDH. The type II density matrix expands the wavefunction a step further into SPFs. The computational scaling for type II now lies in the expansion coefficients of the SPFs, and thus is more suitable for smaller systems. The two approaches, however, are equivalent and give identical results. For these reasons, the type II density MCTDH form of the density matrix, ρ -MCTDH⁽²⁾, was used for these 2D calculations.

As the system was simple enough, the final method used on this 2D system was an exact propagation of the density matrices, i.e. the full solution of the density matrix. This was to determine that the ρ -MCTDH⁽²⁾ was predicting the correct dynamics of the thermalised system, and the thermalised-MCTDH method was falling short and missing out some key interactions.

The next set of calculations focuses on a larger 4D system, using the ν_1 , ν_{36} , ν_{10} , and ν_{11} modes. The objective of these calculations were to prove that the ML-MCTDH form of the density matrix, ρ -ML-MCTDH, could be successfully implemented by us into the Quantics code and could produce identical results to ρ -MCTDH, but much more efficiently.

The final set of calculations tested the limits of what the ρ -ML-MCTDH method is capable of by applying it to a 8D and 13D system. For the reasons discussed above, these were performed using the type I formalism.

6.5 2D salicylaldimine Results

The first set of results, figure 6.3, show the dynamics of the 2D system using the thermalised-MCTDH method. Plotting the expectation of the step function against time allows the dynamics of the various methods to be compared. The Heaviside step function is a function that on this system is placed on the saddle point, at $q=0$ along the reaction coordinate. The expectation value of this function is 0 when the wavepacket is to the right hand side, and 1 when to the left hand side. Therefore, in this system it is a show of what proportion of the wavepacket has crossed the barrier.

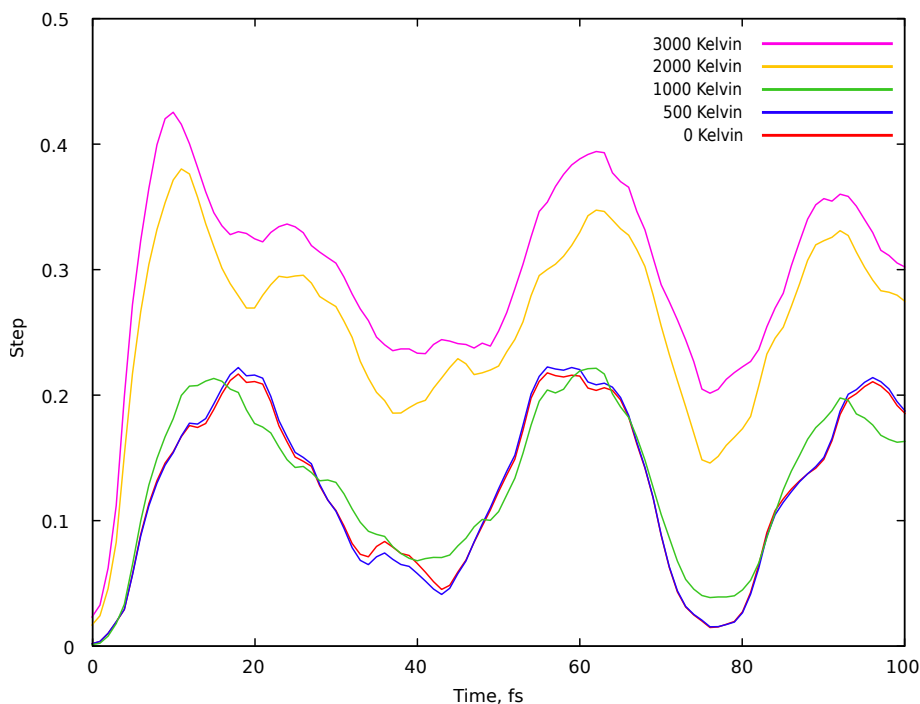


Figure 6.3: Using the thermalised-MCTDH method, the step function expectation value as a function of time for the 2D salicylaldimine system, including ν_1 and ν_{36} , for various temperatures ranging from 0 \rightarrow 3000 K.

At 0 Kelvin, the only movement of the system occurs through proton tunnelling, where part of the wavepacket crosses the barrier from the global enol-minimum into the less stable keto-minimum. Increasing the temperature from 0 \rightarrow 500 K \rightarrow 1000 K does not change the dynamics of the system significantly. The slight difference between the plots for 500 K and 1000 K could be attributed to the dynamics at 1000 K now having enough energy to overcome the lower activation energy barrier for the return keto \rightarrow enol tautomerisation. Therefore, the dynamics are no longer just the quantum proton tunnelling. The most significant change in dynamics occurs when the temperature increases from 1000 K \rightarrow 2000 K. The zero point energy, ZPE, of ν_1 can be calculated by the formula,

$$ZPE = \frac{1}{2} \sum_k \omega_k. \quad (6.18)$$

The ZPE of the system along the reaction coordinate is 0.094 eV, which means the energy barrier is now 0.098 eV. This is 1140 K. Therefore, the large change in dynamics occurring for this temperature can be explained. Although this system may not be a realistic system in the sense that this molecule will probably have dissociated at the high temperatures described, it serves only as a test system for the method.

As mentioned in the previous section, this method works by using random numbers to generate a set of initial wavefunctions. Taking the average of the expectation value of the step function at each time step of each propagation allowed the dynamics of the thermalised system to be determined. The number of propagations needed before convergence was reached is expressed in table 6.3. All the listed propagations were run using 16 SPFs in both the ν_1 and ν_{36} DOF, for all temperatures. The ν_1 modes is represented as a sine DVR, with 61 grid points, and the ν_{36} mode is represented as a harmonic oscillator using 21 grid points. Convergence was achieved with respect to the step plots, i.e. when the dynamics no longer significantly changed by including more propagations, convergence had

been reached.

Temperature (K)	Number of propagations needed
500	10
1000	21
2000	30
3000	30

Table 6.3: The number of propagations needed for the thermalised-MCTDH method to converge. The different propagations within each temperature each begin with a different seed

Whilst these results using the thermalised-MCTDH method are logical and show a correct trend, it was necessary to compare these results to the exact solution of the dynamics at the same temperatures. The results of the exact method are shown in figure 6.4.

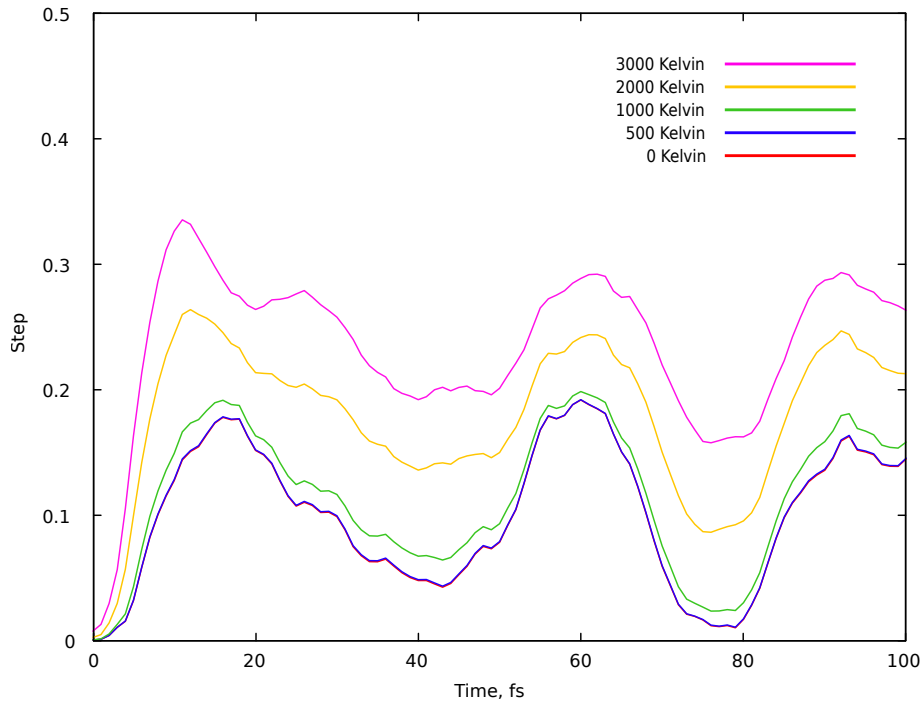


Figure 6.4: Using the exact method, the step function as a function of time for the 2D salicylaldimine system, including ν_1 and ν_{36} , for various temperatures ranging from 0 \rightarrow 3000 K.

While the overall trends for the dynamics as the temperature increases matches that of the previous thermalised-MCTDH method, the fine details of the dynamics

are different. This can be attributed to the approximate nature of the thermalised-MCTDH method. The thermalised-MCTDH method uses a set of independent wavefunctions to describe the system at a temperature > 0 K. Thermalised systems are an incoherent statistical mixture of states, but in the full density matrix picture the components of the incoherent superposition do interact, and cannot be exactly described using independent wavefunctions. Therefore, this method fails to account for this, and is only an approximation.

The ρ -MCTDH method can correctly account for the thermalised system, and by implementing this method the dynamics should be that of the exact calculations. The results for the ρ -MCTDH(II) method are shown in figure 6.5 and they do indeed agree with the exact results. The ρ -MCTDH(II) propagations on the 2D system were all run using 32 SPFs in the ν_1 DOF, and 16 SPFs in the ν_{36} DOF, for all temperatures. The ν_1 mode is represented as a sine DVR, with 61 grid points, and the ν_{36} mode is represented as a harmonic oscillator using 21 grid points.

From looking at these results it is clear that the ρ -MCTDH approach can accurately predict the dynamics of a thermalised salicylaldimine system, as can be seen by comparing the plots in figure 6.5 to that of figure 6.4, which are identical. The ρ -MCTDH replicates the results obtained by an exact calculation, whereas the thermalised-MCTDH approach fails at this. This failure arises from the independence of the wavefunctions generated from the thermalised MCTDH method, compared to the incoherent states in the density matrix incoherent mixture which are able to interfere with each other.

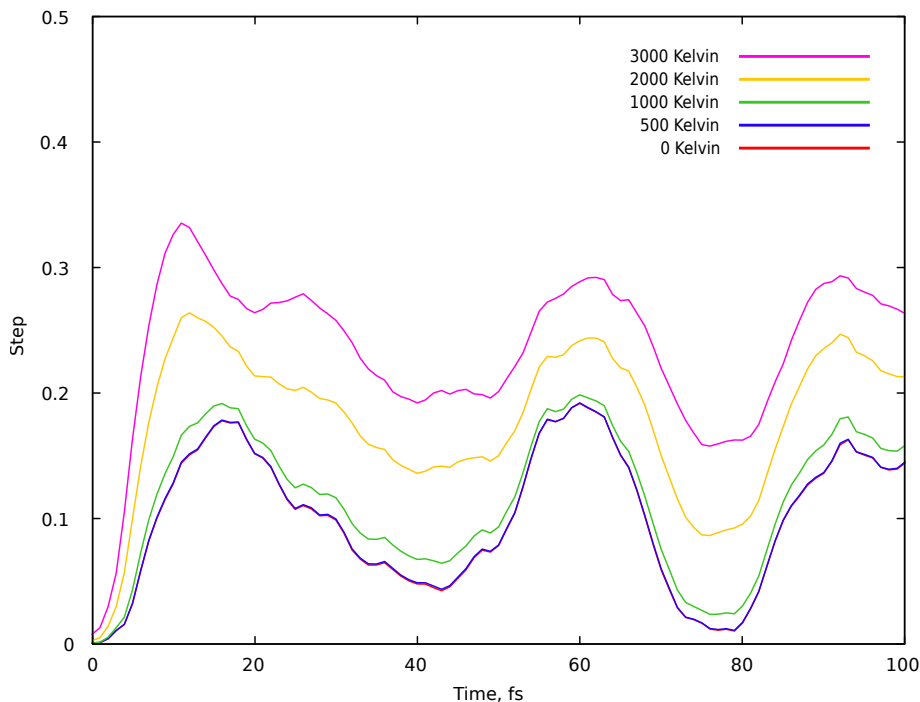


Figure 6.5: Using the ρ -MCTDH(II) method, the step function expectation value as a function of time for the 2D salicylaldimine system, including ν_1 and ν_{36} , for various temperatures ranging from 0 \rightarrow 3000 K.

6.6 4D salicylaldimine Results

This next set of results will show that the ML-MCTDH form of the density matrix, ρ -ML-MCTDH, can also be successfully used to predict the dynamics of the proton transfer in salicylaldimine. This 4D salicylaldimine system is really pushing the limits of the standard MCTDH density matrix approach, ρ -MCTDH, due to the computational effort discussed in chapter 3. Plotting the expectation value of the step function, as before, allows the dynamics of the system to be tracked.

Having shown in the previous results section that the ρ -MCTDH method at finite temperatures can give accurate and reliable results, this method will now act as a benchmark for the ρ -ML-MCTDH method. Using the ρ -ML-MCTDH(II) method for the 4D system allowed for the most efficient calculations.

The first plot, figure 6.6, shows the dynamics of the 4D salicylaldimine system

at temperatures ranging from $0 \rightarrow 3000$ K. This 4D system adds ν_{10} and ν_{11} to the existing ν_1 and ν_{36} modes, as these extra have been shown to be significant to the proton transfer process[150].

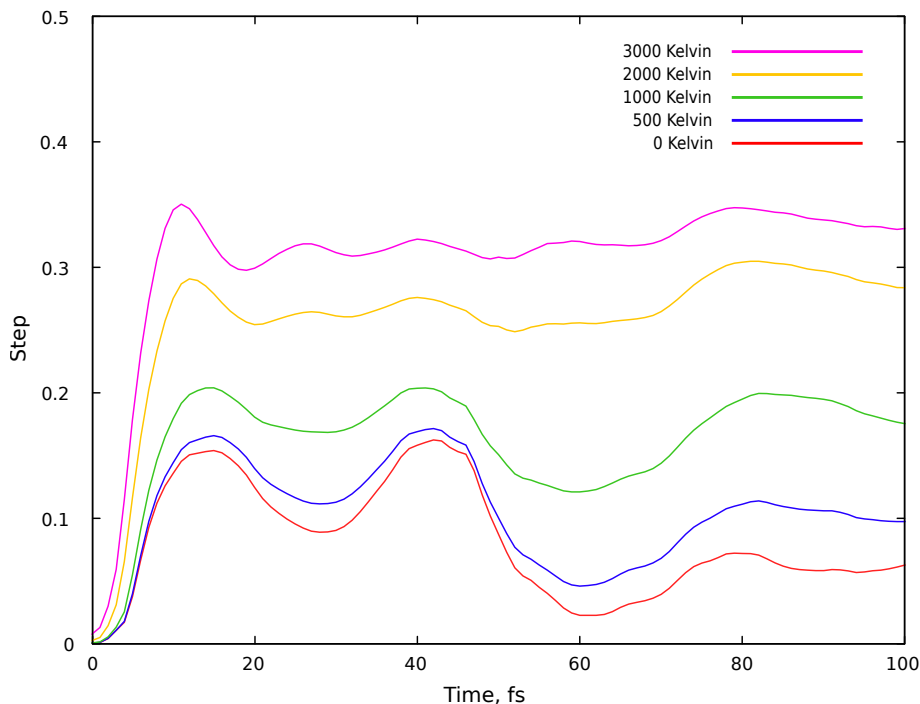


Figure 6.6: Using the ρ -MCTDH(II) method, the step function expectation value as a function of time for the 4D salicylaldimine system, for various temperatures ranging from $0 \rightarrow 3000$ K.

The results from the 2D salicylaldimine proved that this ρ -MCTDH method works, and that these results are reliable. The general trend of increased dynamics as temperature increases supports this. However, as mentioned, this method becomes quickly infeasible for large systems. Even for this relatively small 4D system, in order to converge these propagations using ρ -MCTDH(II), the computational effort was large. The timings and number of basis functions required to converge these calculations are shown in table 6.4.

As this 4D system is at the higher limits of what the ρ -MCTDH method can achieve, it was an optimally sized system to check the validity of the ρ -ML-MCTDH method, as the two methods can be readily compared.

Temperature (K)	Time (hours)	SPFs	
		$(\nu_1 + \nu_{36})$	$(\nu_{10} + \nu_{11})$
0	15.5	32	32
500	27.5	32	32
1000	157	42	52
2000	85	42	52
3000	46	42	52

Table 6.4: The number of SPFs needed to converge the 4D salicylaldimine ρ -MCTDH(II) calculations, along with the timings.

Using the same temperatures as used for the ρ -MCTDH calculations, the propagations were repeated using the ρ -ML-MCTDH(II) method. The ML-tree implemented for these calculations is shown in figure 6.8. The groupings of the modes were based on the coupling strengths, and grouping those of similar strength together.

The results of this are shown in figure 6.7.

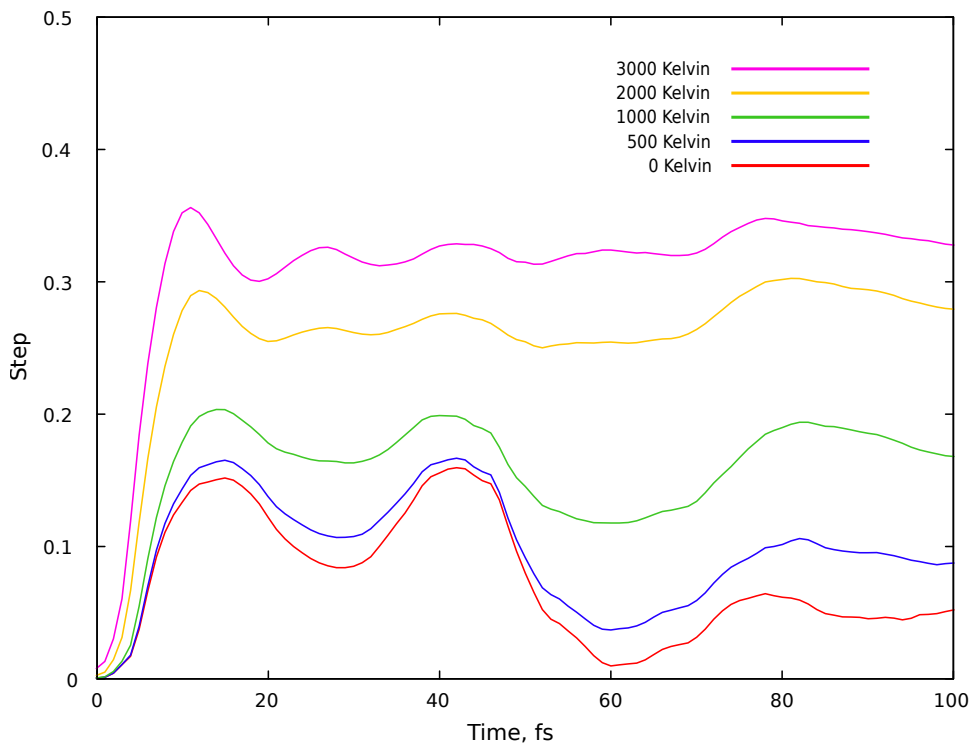


Figure 6.7: Using the ρ -ML-MCTDH(II) method, the step function expectation value as a function of time for the 4D salicylaldimine system, for various temperatures ranging from 0 \rightarrow 3000 K.

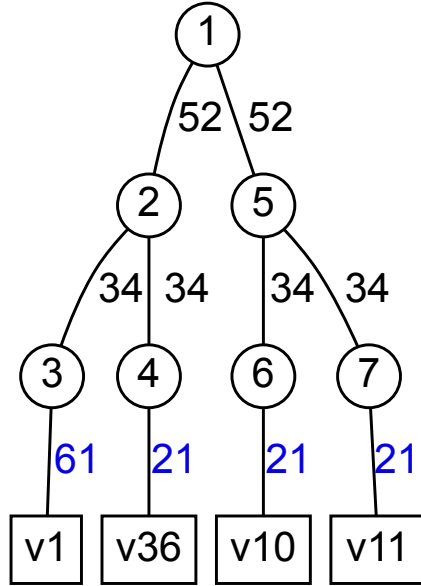


Figure 6.8: The ML-tree used to describe the nuclear wavefunction in the ρ -ML-MCTDH(II) method including 4 DOF. As an example, the number of SPFs in each layer is shown in black, with the number of primitive basis functions shown in blue were used in the 500 K propagation, but the number of SPFs required vary with temperature.

The plots of the expectation value of the step function clearly show that the dynamics calculated with the two different methods are equivalent. Therefore, the validity of the ρ -ML-MCTDH has been shown. A comparison of the timings of the methods is shown in table 6.5.

Temperature (K)	Time taken (hours)	
	ρ -MCTDH(II)	ρ -ML-MCTDH(II)
0	15.5	5
500	27.5	14
1000	157	12.5
2000	85	255
3000	46	444

Table 6.5: A comparison of the timings for the ρ -MCTDH(I) and ρ -ML-MCTDH(II) method for a 4D salicylaldimine system at various temperatures.

Using the ρ -ML-MCTDH method allows much larger systems to be treated than the standard ρ -MCTDH method could. It can be seen from table 6.5 that using the ρ -ML-MCTDH method does not automatically increase efficiency. Due to the additional equations of motion required to solve the wavefunction in the

multi-layer form, for these smaller systems it becomes more expensive to solve the wavefunction in this way. This is not specific to the ρ -ML-MCTDH method, but the ML-MCTDH method in general. Since the aim of these sets of results was not to prove the speed up of calculations, but to prove the validity of the ρ -ML-MCTDH method, this is not an issue here. The extreme inefficiencies of the ρ -ML-MCTDH in this specific case could possibly be due to the layering structure the wavefunction has been separated into not being fully optimised. The way the ML-tree is set up can greatly affect the efficiency of the ML calculations, for both density matrices and pure wavefunctions.

6.7 8D and 13D salicylaldimine Results

The next set of results will really push the limits of the ρ -ML-MCTDH method. Running calculations on the 8D and 13D salicylaldimine system will establish if it is possible to determine the dynamics of the proton transfer on a large system using this method. Using a density matrix on these larger systems is extremely computationally expensive, so if the ρ -ML-MCTDH method is able to simulate dynamics on systems of this size, it would be a very encouraging result for the future of this method.

The ML-tree structures of the 8D and 13D systems are shown in figures 6.9 and 6.10 respectively.

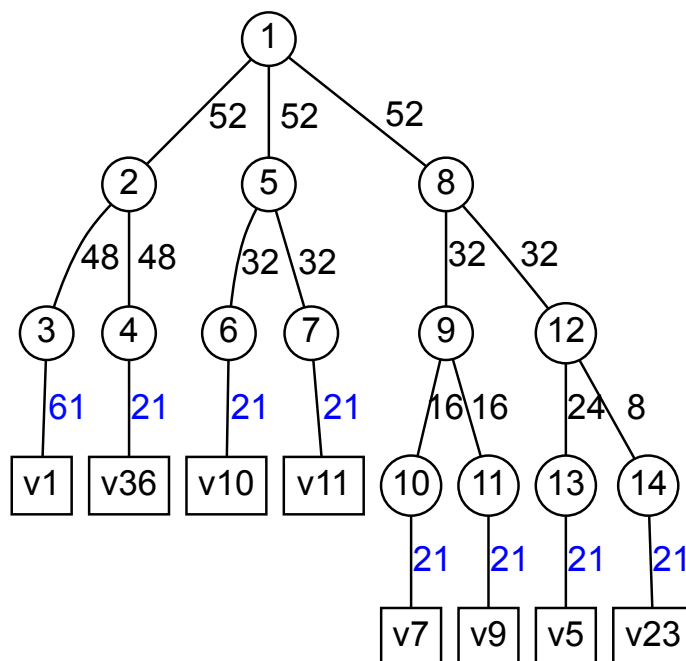


Figure 6.9: The ML-tree used to describe the nuclear wavefunction in both the ρ -ML-MCTDH(I) method including 8 DOF. As an example, the number of SPDOs in each layer is shown in black, with the number of primitive basis functions shown in blue were used in the 500 K propagation, but the number of SPDOs required vary with temperature.

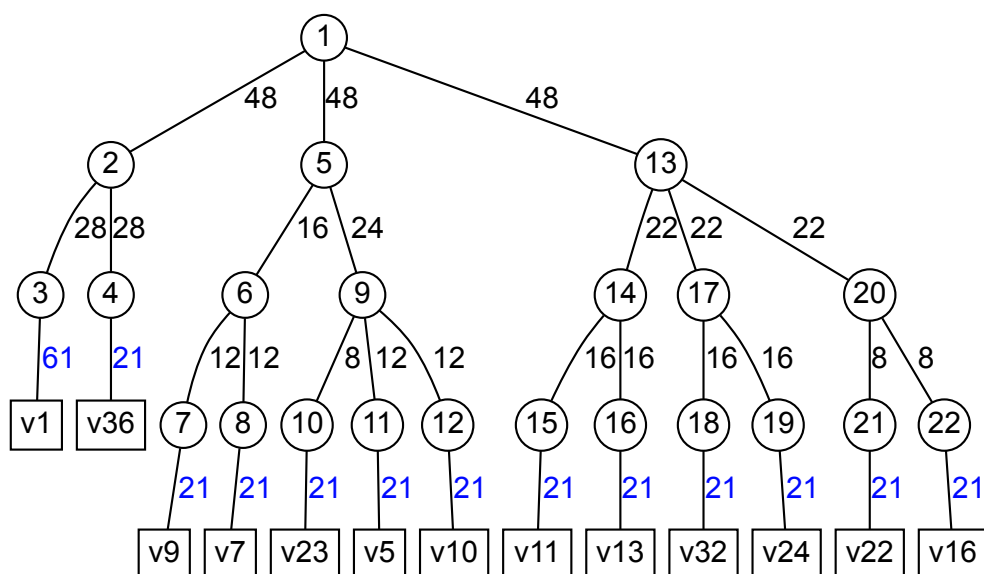


Figure 6.10: The ML-tree used to describe the nuclear wavefunction in both the ρ -ML-MCTDH(I) method including all available 13 DOF. As an example, the number of SPDOs in each layer is shown in black, with the number of primitive basis functions shown in blue were used in the 500 K propagation, but the number of SPDOs required vary with temperature.

As before, the groupings of the modes were based on grouping modes with similar coupling strengths.

The following plots, figures 6.11 and 6.12, show the expectations value of the step function for the 8D system and the 13D system, respectively.

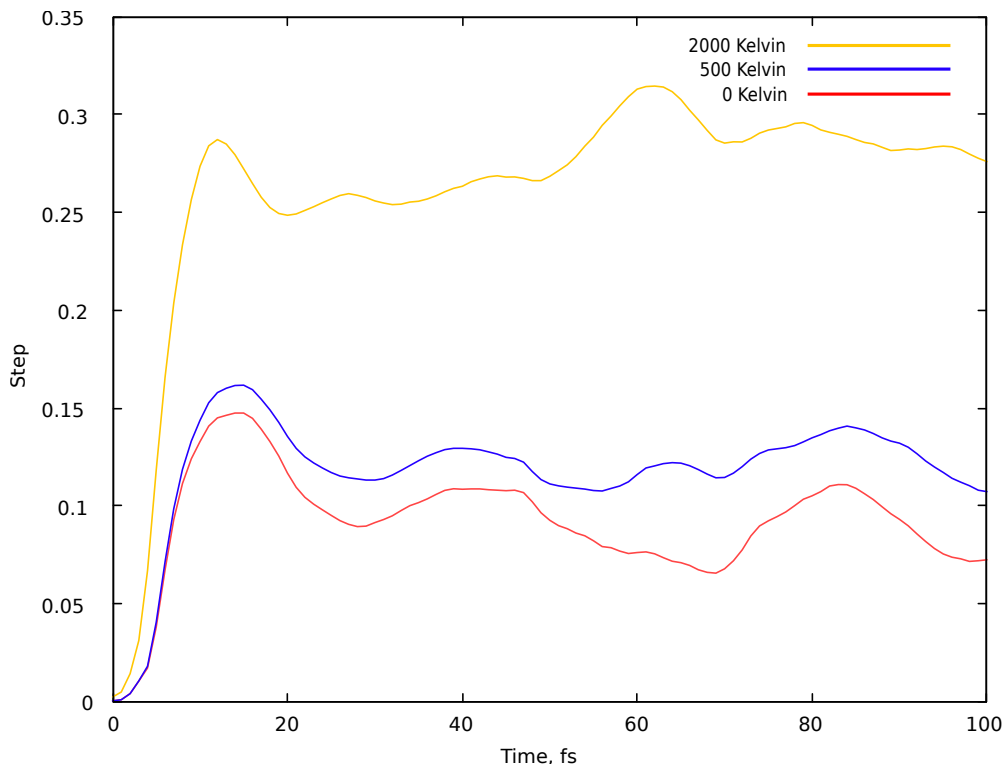


Figure 6.11: Using the ρ -ML-MCTDH(I) method, the step function as a function of time for the 8D salicylaldehyde system for temperatures 0, 500, and 2000 K.

These results show that the trend previously exhibited in the smaller systems is replicated here. There is, however, an obvious damping of the population oscillations in higher dimensional systems when compared to those plots for the 2D and 4D systems. In the smaller systems, there are oscillations in the population with a time period of roughly 40 fs, which are not present in the 8D and 15D plots. The large change in dynamics occurs when the temperature exceeds the energy barrier of the proton transfer, which is as expected. The computational expense to predict these dynamics using the standard density matrix ρ -MCTDH method would be huge, and be completely infeasible. However, by implementing

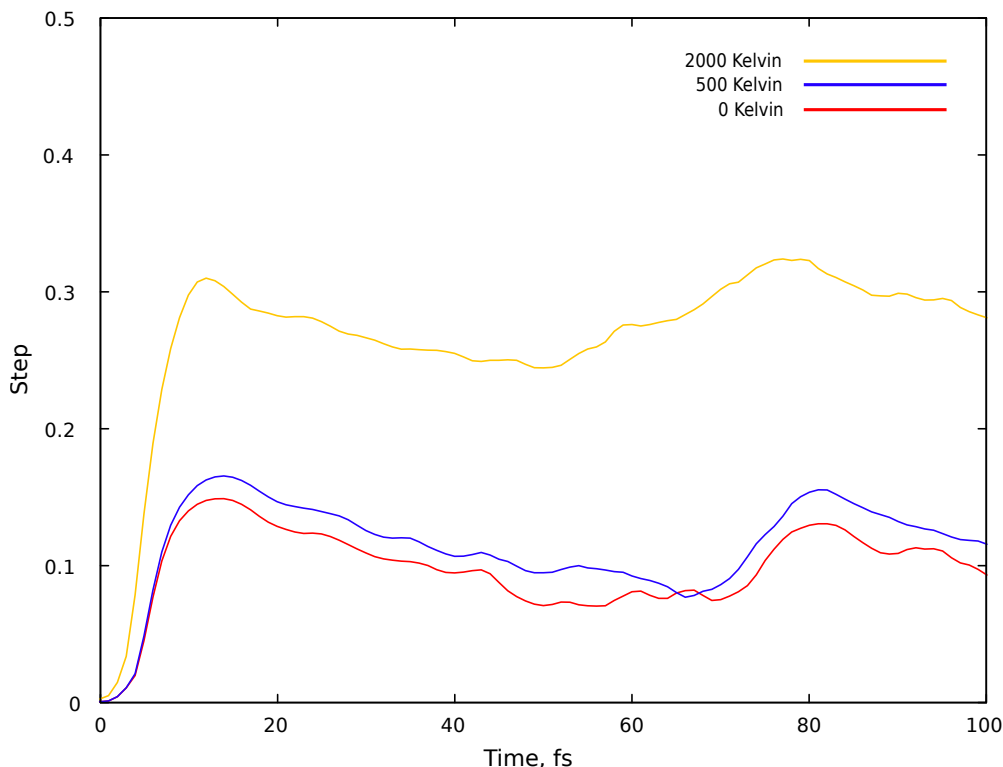


Figure 6.12: Using the ρ -ML-MCTDH(I) method, the step function as a function of time for the 13D salicylaldimine system for temperatures 0, 500, and 2000 K.

the ρ -ML-MCTDH method, these larger systems are opened up to investigation. The time taken to collect the data plotted in figures 6.11 and 6.12 are shown in table 6.6.

Size of System	Time Taken (hours)		
	0 K	500 K	2000 K
8D	28	60	53
13D	351	314	374

Table 6.6: A table showing the time taken to run the propagations for the 8D and 13D systems, at 0, 500, and 2000 K.

It can be clearly see from both this table, and table 6.5, that the time taken to propagate the system rising exponentially with the number of modes included in the dynamics. Even though, due to an incomplete basis set, the dynamics of the 13D system are not fully converged, it is clear that this method is feasible for a system as large as this.

6.8 Summary

Analysing all the dynamics collected for this chapter, it is very clear by looking at the results presented in section 6.5, that not only can the ρ -MCTDH accurately predict the dynamics of a proton transfer in the ground state system at finite temperatures, but it actually captures a lot of the fine detail of the dynamics lost by using the wavefunction approach of the thermalised-MCDTH method.

It is also clear that by looking at the results presented in sections 6.6 and 6.7 that by implementing the ML-MCTDH form of the density matrix, ρ -ML-MCTDH, the dynamics of previously inaccessible larger systems can be investigated. This approach of studying larger systems at temperatures above 0 Kelvin in this quantum manner is enormously under-reported, despite the vast scope of this method. Using this method not only allows these large systems to be treated, but the theory of the density matrix approach allows environmental effects to be included in the dynamics. This ability to predict accurate quantum dynamics on systems above 0 K, combined with solvent and/or environmental effects, has extremely wide applications. One such application of interest to this thesis could be using this ρ -ML-MCTDH method to study the dynamics of the electron transfer process on the previous dye-semiconductor system from chapter 5.

Chapter 7

Conclusions

The aim of this report was to outline the background, theory and methods as to how one can begin to solve the time-dependent Schrödinger equation (TDSE), with the aim of simulating a charge transfer process in a dye-semiconductor system, and to highlight the results obtained so far. The need to simulate the quantum dynamics of a charge transfer have been discussed in detail in chapter 2. It highlights the importance of an electron transfer being a key process in the conversion of solar to electrical energy in a dye-sensitised solar cell (DSSC). Only by fully understanding these key processes can one begin to design and develop more efficient and commercially viable solar cells.

In order to simulate the dynamics of a system, one firstly implements the Born-Oppenheimer approximation, (BOA), where the electronic motion and nuclear motion of the full wavefunction are separated. The electronic states are solved using *ab initio* methods, and are plotted along the coordinates of the system. The nuclear wavepacket then moves over these stationary electronic surfaces according to the TDSE. There are various ways in which the TDSE can be solved, described in chapter 3. This thesis has focused on 2 approaches, the multi-configuration time-dependent Hartree method (MCTDH) and the multi-layer multi-configuration time-dependent Hartree method (ML-MCTDH). This thesis set out to not only show that the electron transfer process can be simu-

lated, but a secondary motivation was to showcase the ability of the ML-MCTDH method. The results presented in this thesis have shown it to be a very useful tool in predicting the dynamics of the three systems discussed.

Firstly, in chapter 4, the Quantics program was used to run quantum dynamic simulations using both the MCTDH and ML-MCTDH methods on the ground state of radical cationic allene, a small system exhibiting a Jahn-Teller conical intersection. The molecule in this state undergoes a charge transfer along the molecule. This system was chosen as it provided a suitable precursor to studying a dye-semiconductor charge transfer, both a donor-acceptor state-type system. The potential energy surfaces along each mode were predicted, using both electron propagator theory, (EPT) and complete active space self consistent field theory, (CASSCF). Using the ML-MCTDH method, the dynamics of the charge transfer were predicted for the full 15-mode system and the photoelectron spectrum predicted. This resulted in a good agreement with the experimental spectrum for the dynamics run on the surfaces obtained through EPT, but the experimental results were much less accurately reproduced using the surfaces obtained via CASSCF. This project showed that the ML-MCTDH was a suitable method to predict charge transfer dynamics in donor-acceptor systems.

Simulating the charge transfer from a dye molecule into the conduction band of a semiconductor required an adapted model, discussed in chapter 5. The simple donor-acceptor system becomes more complex as now there are several acceptor states in the discretised conduction band. The molecules chosen were Coumarin-343 as the dye molecule, and a TiO_2 semiconductor due to the abundance of both experimental and theoretical data to benchmark the results against. The main issue that emerged in this project was how to account for the donor-acceptor coupling terms. The initial approach of an decay function to generate coupling terms, adapted from a series of papers on a similar study, turned out to not be an

appropriate model for these dynamics. This meant a new approach to the coupling was required, and a new model was implemented. With the new coupling approach between the donor and acceptor state being implemented into the Quantics code, the dynamics of the electron injection process were probed. When the vibronic coupling terms were not included, i.e. just the electronic dynamics, the system behaved as expected, exhibiting a smooth exponential donor state decay, on the 40 fs time scale. Using the ML-MCTDH method, the dynamics of the electron injection process were investigated including up to 17 degrees of freedom, DOF. The unexpected lack of change in dynamics after adding in the vibronic coupling led to further developments to this model. By probing the complex of the dye attached to the semiconductor surface, 2 pseudo vibronic modes were created for the system, representing the symmetrical and anti-symmetrical stretch of the adsorption bonds. This adaptation of the model has yet to provide conclusive results as to the validity of the model, but the results presented so far show this model to be an excellent starting point for these types of systems.

Following on from this work on the dye-semiconductor system, the quantum dynamics of a proton transfer in a donor-acceptor system at temperatures >0 Kelvin were simulated, discussed in chapter 6. This required the use of density matrices. By using the novel approach of using the ML-MCTDH formalism of the density matrix, the ground state proton transfer in the molecule Salicylaldehyde was simulated, including 13 DOF. This proton transfer has an energy barrier equating to roughly 1500 K. By plotting the expectation value of the step function as a function of time, the dynamics of the proton transfer was simulated at various temperatures, both above and below the energy barrier. The computational effort of using density matrices has previously limited the size of systems probed in this way, but by implementing the ML-MCTDH formalism of the density matrix, the method opens up to much larger systems. This exciting prospect of probing

the quantum dynamics of systems above 0 Kelvin has potential in many areas of research. The next route of research for this method is to apply it to the dye-semiconductor systems to see how temperature affects the dynamics of the key electron transfer step in determining the efficiency of DSSC.

Appendix A

Appendix

Table A.1: A table showing the calculated frequencies and κ values for Coumarin-343

Mode	Frequency (eV)	κ^d (eV)	κ^a (eV)
1	0.00334	0.00200	-0.01865
2	0.00502	-0.00211	-0.00128
3	0.00673	0.00168	-0.03146
4	0.01096	0.00746	-0.00318
5	0.01205	-0.00139	-0.00795
6	0.01579	0.05815	-0.00191
7	0.01723	0.00455	0.01599
8	0.01988	0.00544	-0.00523
9	0.02704	0.00688	-0.02578
10	0.02812	-0.00031	-0.02440
11	0.03362	0.02104	0.00385
12	0.03512	0.01916	-0.03995
13	0.03886	-0.00296	-0.00693
14	0.04072	0.00585	-0.01475
15	0.04332	0.01165	0.03223
16	0.04612	0.00601	-0.00208
17	0.05022	-0.03889	-0.00165
18	0.05121	0.00839	-0.01014
19	0.05412	0.00712	-0.01577
20	0.05629	0.01180	0.01463
21	0.05801	0.00773	-0.00154
22	0.05914	0.01648	0.03637
23	0.06616	-0.00621	-0.00549
24	0.06639	-0.00337	0.01324
25	0.06939	0.01730	-0.00778
26	0.07017	-0.00275	0.01893
27	0.07455	0.01428	0.01011

Continued on next page

Table A.1 – continued from previous page

Mode	Frequency (eV)	κ^d (eV)	κ^a (eV)
28	0.07687	-0.02569	-0.01751
29	0.07944	-0.03378	0.07570
30	0.08521	0.00339	0.00840
31	0.08691	0.01054	-0.00338
32	0.09050	-0.01945	-0.00371
33	0.09141	0.01648	0.00229
34	0.09657	0.01003	0.01379
35	0.09895	0.00569	0.00194
36	0.10141	-0.00078	0.00306
37	0.10721	0.01215	0.01659
38	0.10780	-0.00060	0.01153
39	0.10959	-0.00704	-0.01160
40	0.11118	-0.00293	0.02238
41	0.11244	-0.01818	0.01269
42	0.11298	-0.00115	0.06700
43	0.11383	-0.00188	0.00649
44	0.11728	0.01793	-0.05002
45	0.12245	-0.02708	-0.02928
46	0.12371	0.00126	-0.01292
47	0.12732	-0.00073	-0.00411
48	0.12958	-0.01303	-0.02069
49	0.13203	0.01362	0.04295
50	0.13343	0.03118	0.00459
51	0.13612	0.00254	-0.03222
52	0.13672	-0.01589	-0.01421
53	0.13798	0.00331	-0.02371
54	0.14537	-0.00501	-0.01281
55	0.14697	-0.03470	0.00026
56	0.14903	-0.01423	-0.00137
57	0.15027	-0.00986	-0.02934
58	0.15217	0.01326	0.00314
59	0.15274	-0.00680	0.02529
60	0.15471	0.00972	0.00414
61	0.15578	0.01826	0.00046
62	0.16117	-0.00853	-0.01498
63	0.16231	0.00377	-0.02954
64	0.16321	0.00097	-0.00235
65	0.16604	-0.00110	0.00523
66	0.16817	-0.02745	-0.02873
67	0.16878	-0.02445	0.00791
68	0.16926	-0.00615	-0.02446
69	0.17108	-0.00620	0.01950

Continued on next page

Table A.1 – continued from previous page

Mode	Frequency (eV)	κ^d (eV)	κ^a (eV)
70	0.17157	-0.00095	0.00647
71	0.17219	0.00269	0.01864
72	0.17225	-0.00863	-0.01277
73	0.17393	0.03782	-0.00609
74	0.18019	-0.01623	-0.00824
75	0.18249	-0.00532	0.00266
76	0.18402	0.00687	0.00452
77	0.18420	-0.00424	0.01207
78	0.18524	0.00532	0.01274
79	0.18525	0.00311	-0.01070
80	0.18699	-0.01219	0.00569
81	0.18715	-0.00002	0.00241
82	0.19202	0.01187	0.03439
83	0.19627	0.02068	-0.00195
84	0.20222	0.03802	-0.01749
85	0.20519	0.02633	0.00027
86	0.22078	-0.04414	0.00330
87	0.22933	-0.01984	-0.02539
88	0.36542	0.00620	0.00733
89	0.36635	-0.01253	0.00577
90	0.37184	0.00368	-0.00551
91	0.37306	0.00474	0.02617
92	0.37621	-0.00197	0.00905
93	0.37650	-0.00098	-0.00636
94	0.37899	0.00311	-0.00339
95	0.38003	0.00130	-0.00356
96	0.38017	0.00397	-0.04007
97	0.38183	-0.00194	0.00083
98	0.38188	-0.00395	0.01265
99	0.38263	-0.00141	-0.00738
100	0.39159	-0.00313	-0.00040
101	0.39620	0.01709	0.00413
102	0.46681	-0.00001	0.00865

Bibliography

- [1] J. Li, I. Kondov, H. Wang, and M. Thoss. Theoretical study of photoinduced electron-transfer processes in the dye-semiconductor system alizarin-TiO₂. *J. Phys. Chem. C*, 114:18481–18493, 2010.
- [2] M. Born and R. Oppenheimer. Zur quantentheorie der molekeln. *Ann. Phys.*, 84:457–484, 1927.
- [3] X. Li, J. C. Tully, H. Bernhard Schlegel, and M. J. Frisch. Ab initio ehrenfest dynamics. *J. Chem. Phys.*, 123:084106, 2005.
- [4] G. A. Worth and M. A. Robb. Applying direct molecular dynamics to non-adiabatic systems. *Adv. Chem. Phys.*, 124:355–432, 2002.
- [5] G. A. Worth and L. S. Cederbaum. Beyond Born-Oppenheimer: Conical intersections and their impact on molecular dynamics. *Ann. Rev. Phys. Chem.*, 55:127–158, 2004.
- [6] K. S. Zinchenko, F. Ardana-Lamas, I. Seidu, S. P. Neville, J. van der Veen, V. Utrio Lanfaloni, M. S. Schuurman, and H. J. Wörner. Sub-7-femtosecond conical-intersection dynamics probed at the carbon k-edge. *Science*, pages 489–494, 2021.
- [7] J. Von Neuman and E. Wingner. Concerning the behaviour of eigenvalues in adiabatic processes. *Z. Phys.*, 30:467–470, 1929.

Bibliography

- [8] G. Lindblad. On the generators of quantum dynamical semigroups. *Commun. Math. Phys.*, 48:119–130, 1976.
- [9] A. G. Redfield. The theory of relaxation processes. *Adv. Magn. Reson.*, 1:1–32, 1965.
- [10] A. O. Caldeira and A. J. Leggett. Quantum tunnelling in a dissipative system. *Ann. Phys.*, 149:374–456, 1983.
- [11] A. O. Caldeira and A. J. Leggett. Path integral approach to quantum brownian motion. *Physica*, 121 A:587–616, 1983.
- [12] M. Born and K. Huang. *The Dynamical Theory of Crystal Lattices*. Oxford University Press, Oxford, U.K., 1954.
- [13] B. F. E. Curchod and T.J. Martínez. Ab initio nonadiabatic quantum molecular dynamics. *Chem. Rev.*, 118:3305–3336, 2018.
- [14] R. L. Whetten, G. S. Ezra, and E. R. Grant. Molecular dynamics beyond the adiabatic approximation: New experiments and theory. *Ann. Rev. Phys. Chem.*, 36:277–320, 1985.
- [15] R. P. Feynman. Forces in molecules. *Phys. Rev.*, 56:340–343, 1939.
- [16] H. A. Jahn and E. Teller. Stability of polyatomic molecules in degenerate electronic states. i. orbital degeneracy. *Proc. R. Soc. A*, 161:220–235, 1937.
- [17] R. Englman. *The Jahn-Teller effect in molecules and crystals*. John Wiley and sons, New York, 1972.
- [18] I. B. Bersuker. *The Jahn-Teller effect and vibronic interactions in modern chemistry*. Plenum, New York, 1984.

Bibliography

- [19] T A Barckholtz and T A Miller. The calculation of spectroscopic Jahn-Teller parameters by ab initio methods. *J. Phys. Chem. A*, 103:2321–2336, 1999.
- [20] G. W. Richings and G. A. Worth. Multi-state non-adiabatic direct-dynamics on propagated diabatic potential energy surfaces. *Chem. Phys. Lett.*, 683:606–612, 2017.
- [21] M. Baer. Topological effects in molecular systems : an attempt towards a complete theory. *Chem. Phys.*, 259:123–147, 2000.
- [22] W Domcke, D R Yarkony, and H Köppel, editors. *Conical intersections: Electronic structure, dynamics and spectroscopy*. World Scientific, Singapore, 2004.
- [23] X. Zhu and D. R. Yarkony. Non-adiabaticity: the importance of conical intersections. *Mol. Phys.*, 114:1983–2013, 2016.
- [24] B. F. E. Curchod, U. Rothlisberger, and I. Tavernelli. Trajectory-based nonadiabatic dynamics with time-dependent density functional theory. *Chemphyschem*, 14:1314–1340, 2013.
- [25] D. R. Yarkony. Current issues in non-adiabatic chemistry. *J. Phys. Chem.*, 100:18612–18628, 1996.
- [26] D. R. Yarkony. Diabolical conical intersections. *Rev. Mod. Phys.*, 68:985–1013, 1996.
- [27] F. Bernardi, M. Olivucci, and M. A. Robb. Potential energy surface crossings in organic photochemistry. *Chem. Soc. Rev.*, 25:321–328, 1996.
- [28] T. J. Martínez. Seaming is believing. *Nature*, 412:467, 2010.
- [29] K.B. Lipkowitz, T.R. Cundari, and D.B. Boyd. *Reviews in Computational Chemistry*. Reviews in Computational Chemistry. Wiley, 2007.

Bibliography

- [30] P. Mondal, D. Opalka, L.V. Poluyanov, and Domcke. W. Ab initio study of dynamical $e \otimes e$ jahn-teller and spin-orbit coupling effects in the transition-metal trifluorides TiF₃, CrF₃, and NiF₃. *J. Chem. Phys.*, 136:084308, 2012.
- [31] I. B. Bersuker. Modern aspects of the Jahn-Teller effect theory and applications to molecular problems. *Chem. Rev.*, 101:1067–1114, 2001.
- [32] H. Koppel. Examples of jahn-teller coupling effects in molecular spectroscopy and internal conversion dynamics. *Z. Phys. Chem.*, 200:3–10, 1997.
- [33] S. Mahapatra, G. A. Worth, H.-D. Meyer, L. S. Cederbaum, and H. Köppel. The $\tilde{a}^2e/\tilde{b}^2b_2$ photoelectron bands of allene beyond the linear coupling scheme: An *ab initio* dynamical study including all fifteen vibrational modes. *J. Phys. Chem. A*, 105:5567–5576, 2001.
- [34] G. A. Worth and L. S. Cederbaum. Electron transfer along a conjugated chain: The allene radical cation. *Chem. Phys. Lett.*, 348:477–482, 2001.
- [35] C. Woywod and W. Domcke. Theoretical study of the photoelectron spectrum of allene. *Chem. Phys.*, 162:349–358, 1992.
- [36] A. Markmann, G. A. Worth, S. Mahapatra, H.-D. Meyer, H. Köppel, and L. S. Cederbaum. Simulation of a complex spectrum: Interplay of five electronic states and 21 vibrational degrees of freedom in C₅H₄⁺. *J. Chem. Phys.*, 123:204310–204319, 2005.
- [37] C. S. Goldenstein, R. M. Spearrin, J. B. Jeffries, and R. K. Hanson. Infrared laser-absorption sensing for combustion gases. *Prog. Energy Combust. Sci.*, 60:132–176, 2017.
- [38] H. J. Möller. Semiconductors for solar cell applications. *Prog. Mater Sci.*, 35:205–418, 1991.

Bibliography

- [39] W. Shockley and H. J. Queisser. Detailed balance limit of efficiency of p-n junction solar cells. *J. Appl. Phys.*, 32:510–519, 1961.
- [40] S. Rühle. Tabulated values of the shockley–queisser limit for single junction solar cells. *Sol. Energy*, 130:139–147, 2016.
- [41] M. T. Kibria, A. Ahammed, Sony S. M., F. Hossain, and S. U. Islam. A review and comparative studies on different generation solar cells technology. In *Proceedings of 5th International Conference on Environmental Aspects of Bangladesh [ICEAB 2014]*, page 51, 2014.
- [42] K. Ranabhat, L. Patrikeev, A. Antal’evna-Revina, K. Andrianov, Lapshinsky. V., and E. Sofronova. An introduction to solar cell technology. *Journal of Applied Engineering Science*, 14:481–491, 2016.
- [43] B. O’Regan and M. Grätzel. A low-cost, high-efficiency solar cell based on dye-sensitized colloidal tio_2 films. *Nature*, 335:737, 1991.
- [44] M. Grätzel. Dye-sensitized solar cells. *J. Photochem. Photobiol., C*, 4:145–153, 2003.
- [45] P. Gao, D. Konrad, S. Aghazada, and M. K. Nazeeruddin. Molecular engineering of functional materials for energy and opto-electronic applications. *[CHIMIA] International Journal for Chemistry*, 69:253–263, 2015.
- [46] K. Sharma, V. Sharma, and S. S. Sharma. Dye-sensitized solar cells: Fundamentals and current status. *Nanoscale Res. Lett.*, 13:381, 2018.
- [47] M. A. Green, Y. Hishikawa, E. D. Dunlop, D. H. Levi, J. Hohl-Ebinger, and A. W. Y. Ho-Baillie. Solar cell efficiency tables (version 52). *Prog. Photovoltaics Res. Appl.*, 26:427–436, 2018.

Bibliography

- [48] H. J. Snaith. Estimating the maximum attainable efficiency in dye-sensitized solar cells. *Adv. Funct. Mater.*, 20:13–19, 2010.
- [49] W. Kohn and N. Rostoker. Solution of the schrodinger equation in periodic lattices with an application to metallic lithium. *Phys. Rev.*, 94:1111, 1954.
- [50] N. J. Zabusky. Solitons and bound states of the time-independent schrodinger equation. *Phys. Rev.*, 168:124, 1968.
- [51] J. H. Shirley. Solution of the schrodinger equation with a hamiltonian periodic in time. *Phys. Rev.*, 138:979, 1965.
- [52] E. J. Heller. Time-dependent approach to semiclassical dynamics. *J. Chem. Phys.*, 62:1544–1555, 1975.
- [53] D. R. Hartree and W. Hartree. Self-consistent field, with exchange, for beryllium. *Proc. R. Soc. London A - Math Phys. Sci.*, 150:9–33, 1935.
- [54] D. R. Hartree. The Wave Mechanics of an Atom with a non-Coulomb Central Field. Part II. Some Results and Discussion. *Math. Proc. Cam. Phil. Soc.*, 24:111–132, 1928.
- [55] B. O. Roos. The complete active space self consistent field method and its application to electronic structure calculations. *Adv. Chem. Phys.*, 87:399–466, 1987.
- [56] P. Hohenberg and W. Kohn. Inhomogeneous electron gas. *Phys. Rev. B*, 136:864–871, 1964.
- [57] D. O. Harris, G. G. Engerholm, G. W. Gwinn, and W. D. Gwinn. Calculation of matrix elements for one-dimensional quantum-mechanical problems and the application to anharmonic oscillators. *J. Chem. Phys.*, 43:1515–1517, 1965.

Bibliography

- [58] G. W. Richings and S. Habershon. Direct quantum dynamics using grid-based wave function propagation and machine-learned potential energy surfaces. *Journal of chemical theory and computation : JCTC.*, 13:4012–4024, 2017.
- [59] R. S. Mulliken. Electronic structures of polyatomic molecules and valence VI. On the method of molecular orbitals. *J. Chem. Phys.*, 3:375–378, 1935.
- [60] W. Kohn and L. J. Sham. Self-consistent equations including exchange and correlation effects. *Phys. Rev. A*, 140:1133–1138, 1965.
- [61] D. R. Hartree. The wave mechanics of an atom with a non-coulomb central field part iv further results relating to terms of the optical spectrum. *Proc. Cambridge Philos. Soc.*, 25:310–314, 1929.
- [62] C. C. J. Roothaan. New developments in molecular orbital theory. *Rev. Mod. Phys.*, 23:69–89, 1951.
- [63] D. Cremer. Moller–plesset perturbation theory: from small molecule methods to methods for thousands of atoms. *WIREs Comput Mol Sci*, 1:509–530, 2011.
- [64] D. Roca-Sanjuán, F. Aquilante, and R. Lindh. Multiconfiguration second-order perturbation theory approach to strong electron correlation in chemistry and photochemistry. *Wiley Interdiscip. Rev. Comput. Mol. Sci.*, 2:585–603, 2012.
- [65] T. Koopmans. Über die zuordnung von wellenfunktionen und eigenwerten zu den einzelnen elektronen eines atoms. *Physica*, 1:104–113, 1934.
- [66] J. V. Ortiz. Electron propagator theory: an approach to prediction and interpretation in quantum chemistry. *WIRE: Comput. Mol. Sci.*, pages 123–142, 2013.

Bibliography

- [67] G.F. Martins and B. J. C. Cabral. Electron propagator theory approach to the electron binding energies of a prototypical photo-switch molecular system: Azobenzene. *J. Phys. Chem. A*, pages 2091–2099, 2019. PMID: 30779578.
- [68] L. S. Cederbaum. One-body green’s function for atoms and molecules: theory and application. *J. Phys. B. Atom. Molec. Phys.*, 8:290–303, 1975.
- [69] A. Baiardi, L. Paoloni, V. Barone, V. G. Zakrzewski, and J. V. Ortiz. Assessment of electron propagator methods for the simulation of vibrationally resolved valence and core photoionization spectra. *J. Chem. Theory Comput.*, pages 3120–3135, 2017. PMID: 28521087.
- [70] E. McCullough and R. E. Wyatt. Quantum dynamics of the collinear (H, H₂) reaction. *J. Chem. Phys.*, 51:1253–1254, 1969.
- [71] D Kosloff and R Kosloff. A Fourier-method solution for the time-dependent Schrödinger equation as a tool in molecular dynamics. *J. Comp. Phys.*, 52:35, 1983.
- [72] S. K. Min, F. Agostini, I. Tavernelli, and E. K. U. Gross. Ab initio nonadiabatic dynamics with coupled trajectories: A rigorous approach to quantum (de)coherence. *J. Phys. Chem. Lett.*, 8:3048–3055, 2017.
- [73] B. F. E. Curchod, F. Agostini, and E. K. U. Gross. An exact factorization perspective on quantum interferences in nonadiabatic dynamics. *J. Chem. Phys.*, page 034103, 2016.
- [74] R. P. Feynman and A. R. Hibbs. *Quantum Mechanics and Path Integrals*. McGraw-Hill, New York, 1965.
- [75] P. Ehrenfest. Bemerkung über die angenäherte gültigkeit der klassischen mechanik innerhalb der quantenmechanik. *Z. Phys.*, 45:455, 1927.

Bibliography

- [76] D. Mendive-Tapia, M. Vacher, M. J. Bearpark, and M. A. Robb. Coupled electron-nuclear dynamics: charge migration and charge transfer initiated near a conical intersection. *J. Chem. Phys.*, 139:44110, 2013.
- [77] D. V. Makhov, C. Symonds, S. Fernandez-Alberti, and D. V. Shalashilin. Ab initio quantum direct dynamics simulations of ultrafast photochemistry with multiconfigurational ehrenfest approach. *Chem. Phys.*, 493:200–218, 2017.
- [78] T. Ma, M. Bonfanti, P. Eisenbrandt, R. Martinazzo, and I. Burghardt. Multi-configurational ehrenfest simulations of ultrafast nonadiabatic dynamics in a charge-transfer complex. *J. Chem. Phys.*, 149:244107, 2018.
- [79] J. C. Tully and R. K. Preston. Trajectory surface approach to nonadiabatic molecular collisions: The reaction of $\text{h}^+ + \text{d}_2$. *J. Chem. Phys.*, 55:562–572, 1971.
- [80] J. Spencer, F. Gajdos, and J. Blumberger. FOB-SH: Fragment orbital-based surface hopping for charge carrier transport in organic and biological molecules and materials. *J. Chem. Phys.*, 145:064102, 2016.
- [81] J. C. Tully. Molecular dynamics with electronic transitions. *J. Chem. Phys.*, 93:1061–1071, 1990.
- [82] S. Ghosh, S. Giannini, K. Lively, and J. Blumberger. Nonadiabatic dynamics with quantum nuclei: simulating charge transfer with ring polymer surface hopping. *Faraday Discuss.*, 221:501–525, 2020.
- [83] F. R. Salsbury Jr. Molecular dynamics simulations of protein dynamics and their relevance to drug discovery. *Curr. Opin. Pharmacol.*, 10:738–744, 2010.
- [84] S. Thallmair, J. P. P. Zauleck, and R. de Vivie-Riedle. Quantum dynamics in an explicit solvent environment: A photochemical bond cleavage treated

Bibliography

- with a combined QD/MD approach. *J. Chem. Theory Comput.*, 11:1987–1995, 2015.
- [85] M. S. Topaler, T. C. Allison, D. W. Schwenke, and D. G. Truhlar. What is the best semiclassical method for photochemical dynamics of systems with conical intersections? *J. Chem. Phys.*, 109:3321–3345, 1998.
- [86] A. Liniov, V. Volokitin, I. Meyerov, M. Ivanchenko, and S. Denisov. Increasing performance of the quantum trajectory method by grouping trajectories. In Vladimir Voevodin and Sergey Sobolev, editors, *Supercomputing*, pages 136–150, Cham, 2017. Springer International Publishing.
- [87] R. Kosloff. Time-dependent quantum-mechanical methods for molecular dynamics. *J. Phys. Chem.*, 92:2087–2100, 1988.
- [88] G. W. Richings and S. Habershon. MCTDH on-the-fly: Efficient grid-based quantum dynamics without pre-computed potential energy surfaces. *J. Chem. Phys.*, 148:134116, 2018.
- [89] R. Kosloff. Propagation methods for quantum molecular dynamics. *Annu. Rev. Phys. Chem.*, 45:145–178, 1994.
- [90] J. Frenkel. *Wave Mechanics*. Clarendon Press, Oxford, U.K., 1934.
- [91] H.-D. Meyer, F. Gatti, and G. A. Worth. *Multidimensional Quantum Dynamics: MCTDH Theory and Applications*. Wiley-VCH, Weinheim, Germany, 2009.
- [92] S. jin, C. Sparber, and Z. Zhu. On the classical limit of a time-dependent self-consistent field system analysis and computation. *Kinetic and Related Models*, 10:263–298, 2017.

Bibliography

- [93] M. H. Beck, A. Jäckle, G. A. Worth, and H.-D. Meyer. The multiconfiguration time-dependent Hartree method: A highly efficient algorithm for propagating wavepackets. *Phys. Rep.*, 324:1–105, 2000.
- [94] N. Makri and W. H. Miller. Time-dependent self-consistent (TDSCF) approximation for a reaction coordinate coupled to a harmonic bath: Single and multiconfiguration treatments. *J. Chem. Phys.*, 87:5781, 1987.
- [95] H.-D. Meyer, U. Manthe, and L. S. Cederbaum. The multi-configurational time-dependent Hartree approach. *Chem. Phys. Lett.*, 165:73–78, 1990.
- [96] G. A. Worth, H. D. Meyer, and L. S. Cederbaum. Relaxation of a system with a conical intersection coupled to a bath: A benchmark 24-dimensional wave packet study treating the environment explicitly. *J. Chem. Phys.*, 109:3518–3529, 1998.
- [97] U. Manthe. A multilayer multiconfigurational time-dependent hartree approach for quantum dynamics on general potential energy surfaces. *J. Chem. Phys.*, 128:164116, 2008.
- [98] H. Wang and M. Thoss. Multilayer formulation of the multiconfiguration time-dependent hartree theory. *J. Chem. Phys.*, 119:1289–1299, 2003.
- [99] O. Vendrell and H.-D. Meyer. Multilayer multiconfiguration time-dependent hartree method: implementation and applications to a henon-heiles hamiltonian and to pyrazine. *J. Chem. Phys.*, 134:44135, 2011.
- [100] . Wang and H. D. Meyer. Importance of appropriately regularizing the ml-mctdh equations of motion. *J Phys Chem A*, 2021.
- [101] H. Wang and H.-D. Meyer. On regularizing the ML-MCTDH equations of motion. *J. Chem. Phys.*, 149:044119–11, 2018.

Bibliography

- [102] D. Mendive-Tapia, T. Firmino, H.-D. Meyer, and F. Gatti. Towards a systematic convergence of multi-layer (ML) multi-configuration time-dependent hartree nuclear wavefunctions: The ML-spawning algorithm. *Chem. Phys.*, 482:113–123, 2017.
- [103] Q. Meng and H.-D. Meyer. A multilayer MCTDH study on the full dimensional vibronic dynamics of naphthalene and anthracene cations. *J. Chem. Phys.*, 138:14312–14313, 2013.
- [104] H. D. Meyer and H. Wang. On regularizing the MCTDH equations of motion. *J. Chem. Phys.*, 148:124105, 2018.
- [105] G. A. Worth, M. A. Robb, and I. Burghardt. A novel algorithm for non-adiabatic direct dynamics using variational gaussian wavepackets. *Faraday Discuss.*, 127:307–323, 2004.
- [106] M. Nest and H.-D. Meyer. Dissipative quantum dynamics of anharmonic oscillators with the multiconfiguration time-dependent hartree method. *J. Chem. Phys.*, 119:24–33, 2003.
- [107] A. Raab, I. Burghardt, and H.-D. Meyer. The multiconfiguration time-dependent Hartree method generalized to the propagation of density operators. *J. Chem. Phys.*, 111:8759–8772, 1999.
- [108] A. Raab and H.-D. Meyer. Multiconfigurational expansions of density operators: equations of motion and their properties. *Theor. Chem. Acc.*, 104:358–369, 2000.
- [109] G. Christopoulou, A. Freibert, and G. A. Worth. Improved algorithm for the direct dynamics variational multi-configurational gaussian method. *J. Chem. Phys.*, 154:124127, 2021.

Bibliography

- [110] A. J. Jenkins and M. A. Robb. The damped ehrenfest (d-eh) method: Application to non-adiabatic reaction paths. *Comput. Theor. Chem.*, pages 53–61, 2019.
- [111] P. Baltzer, B. Wannberg, M. Lundqvist, L. Karlsson, D. M. P. Holland, M. A. MacDonald, and W. von Niessen. An experimental and theoretical study of the valence shell photoelectron spectrum of allene. *Chem. Phys.*, 196:551–567, 1995.
- [112] G. A. Worth, K. Giri, G. W. Richings, M. H. Beck, A. Jäckle, and H.-D. Meyer. Quantics package, version 1.1, 2015.
- [113] H. Wang. Multilayer multiconfiguration time-dependent hartree theory. *J. Phys. Chem. A*, 119:7951–7965, 2015.
- [114] M. P. Taylor and G. A. Worth. Vibronic coupling model to calculate the photoelectron spectrum of phenol. *Chem. Phys.*, 515:719–727, 2018.
- [115] M. Assmann, H. Köppel, and S. Matsika. Photoelectron spectrum and dynamics of the uracil cation. *J. Phys. Chem. A*, 119:866–875, 2015.
- [116] C. Cattarius, G. A. Worth, H.-D. Meyer, and L. S. Cederbaum. All mode dynamics at the conical intersection of an octa-atomic molecules: Multiconfiguration time-dependent Hartree (MCTDH) investigation on the butatriene cation. *J. Chem. Phys.*, 115:2088–2100, 2001.
- [117] R. N. Sampaio, Ludovic L., and G. J. J. Meyer. A charge-separated state that lives for almost a second at a conductive metal oxide interface. *Angew. Chem. Int. Ed.*, 57:15390–15394, 2018.
- [118] F.A. Black, C.J. Wood, S. Ngwerume, G.H. Summers, I.P. Clark, M. Towrie, J.E. Camp, and E. A. Gibson. Charge-transfer dynamics at the dye-

Bibliography

- semiconductor interface of photocathodes for solar energy applications. *Faraday Discuss*, 198:449–461, 2017.
- [119] T. V. Pho, M. V. Sheridan, Z. A. Morseth, B. D. Sherman, T. J. Meyer, J. M. Papanikolas, K. S. Schanze, and J. R. Reynolds. Efficient light-driven oxidation of alcohols using an organic chromophore-catalyst assembly anchored to TiO_2 . *ACS Appl. Mater. Interfaces*, 8:9125–9133, 2016.
- [120] R. Huber, J. E. Moser, M. Grätzel, and J. Wachtveitl. Real-time observation of photoinduced adiabatic electron transfer in strongly coupled dye/semiconductor colloidal systems with a 6 fs time constant. *J. Phys. Chem. B*, 106:6494–6499, 2002.
- [121] F. Zimmermann, C. Willig, S. Ramakrishna, B. Burfeindt, B. Pettinger, R. Eichberger, and W. Storck. Experimental fingerprints of vibrational wavepacket motion during ultrafast heterogeneous electron transfer. *J. Phys. Chem. B*, 105:9245–9253, 2001.
- [122] M. Thoss, I. Kondov, and H. Wang. Theoretical study of ultrafast heterogeneous electron transfer reactions at dye–semiconductor interfaces. *Chem. Phys.*, 304:169–181, 2004.
- [123] I. Kondov, M. Thoss, and H. Wang. Theoretical study of ultrafast heterogeneous electron transfer reactions at dye-semiconductor interfaces: Coumarin 343 at titanium oxide. *J. Phys. Chem. A*, 110:1364–1374, 2006.
- [124] I. Kondov, M. Cizek, C. Benesch, H. Wang, and M. Thoss. Quantum dynamics of photoinduced electron transfer reactions in dye-semiconductor systems: Description and application to coumarin 343-TiO₂. *J. Phys. Chem. C*, 111:11970–11981, 2007.

Bibliography

- [125] M. J. Frisch, G. W. Trucks, H. B. Schlegel, G. E. Scuseria, M. A. Robb, J. R. Cheeseman, G. Scalmani, V. Barone, G. A. Petersson, H. Nakatsuji, X. Li, M. Caricato, A. Marenich, J. Bloino, B. G. Janesko, R. Gomperts, B. Mennucci, H. P. Hratchian, J. V. Ortiz, A. F. Izmaylov, J. L. Sonnenberg, D. Williams-Young, F. Ding, F. Lipparini, F. Egidi, J. Goings, B. Peng, A. Petrone, T. Henderson, D. Ranasinghe, V. G. Zakrzewski, J. Gao, N. Rega, G. Zheng, W. Liang, M. Hada, M. Ehara, K. Toyota, R. Fukuda, J. Hasegawa, M. Ishida, T. Nakajima, Y. Honda, O. Kitao, H. Nakai, T. Vreven, K. Throssell, J. A. Montgomery Jr., J. E. Peralta, F. Ogliaro, M. Bearpark, J. J. Heyd, E. Brothers, K. N. Kudin, V. N. Staroverov, T. Keith, R. Kobayashi, J. Normand, K. Raghavachari, A. Rendell, J. C. Burant, S. S. Iyengar, J. Tomasi, M. Cossi, J. M. Millam, M. Klene, C. Adamo, R. Cammi, J. W. Ochterski, R. L. Martin, K. Morokuma, O. Farkas, J. B. Foresman, , and D. J. Fox. Gaussian 09, revision a.02, 2009.
- [126] D. M. Newns. Self-consistent model of hydrogen chemisorption. *Phys. Rev.*, 178:1123–1135, 1969.
- [127] W. Wu, Z. Cao, and Y. Zhao. Theoretical studies on absorption, emission, and resonance raman spectra of coumarin 343 isomers. *J. Chem. Phys.*, 136:114305, 2012.
- [128] I. Kondov, H. Wang, and M. Thoss. Computational study of titanium (iv) complexes with organic chromophores. *Int. J. Quantum Chem.*, 106:1291–1303, 2006.
- [129] X. Gong, A. Selloni, M. Batzill, and U. Diebold. Steps on anatase tio₂(101). *Nat. Mater.*, 5:665–670, 2006.

Bibliography

- [130] Y. Cai and Y. P. Feng. Review on charge transfer and chemical activity of TiO_2 : Mechanism and applications. *Prog Surf Sci*, 91:183–202, 2016.
- [131] Enrico Berardo. *Modelling the Excited State Properties of TiO_2 Nanoparticles*. PhD thesis, 2015.
- [132] L. Kavan, M. Graetzel, S. E. Gilbert, C. Klemenz, and H. J. Scheel. Electrochemical and photoelectrochemical investigation of single-crystal anatase. *Journal of the American Chemical Society*, 118:6716–6723, 1996.
- [133] C. J. Howard, T. M. Sabine, and F. Dickson. Structural and thermal parameters for rutile and anatase. *Acta. Cryst.*, pages 462–468, 1991.
- [134] K. Hara, T. Sato, R. Katoh, A. Furube, Y. Ohga, A. Shinpo, S. Suga, K. Sayama, H. Sugihara, and H. Arakawa. Molecular design of coumarin dyes for efficient dye-sensitized solar cells. *J. Phys. Chem. B*, 107:597–606, 2003.
- [135] L. L. Jiang, W. L. Liu, Y. F. Song, X. He, Y. Wang, H. L. Wu, and Y. Q. Yang. Solvent effects on spectral property and dipole moment of the lowest excited state of coumarin 343 dye. *Chin. J. Chem. Phys.*, pages 577–584, 2012.
- [136] A. Petersson, M. Ratner, and H. O. Karlsson. Injection time in the metaloxide-molecule interface calculated within the tight-binding model. *J. Phys. Chem. B*, 104:8498–8502, 2000.
- [137] S. R. Raga and F. Fabregat-Santiago. Temperature effects in dye-sensitized solar cells. *Phys. Chem. Chem. Phys.*, 15:2328–2336, 2013.
- [138] J. J. Gallardo, J. Navas, R. Alcántara, C. Fernández-Lorenzo, T. Aguilar, and J. Martín-Calleja. On-line thermal dependence study of the main solar

Bibliography

- cell electrical photoconversion parameters using low thermal emission lamps. *Rev. Sci. Instrum.*, 83:063105, 2012.
- [139] S. Bose, V. Soni, and K. R. Genwa. Recent advances and future prospects for dye sensitized solar cells: A review. *IJSRP*, 5:1, 2015.
- [140] A. Hagfeldt, G. Cappel, U. B. and Boschloo, L Sun, L. Kloo, H. Pettersson, and E. A. Gibson. Chapter id-1 - dye-sensitized photoelectrochemical cells. In Augustin McEvoy, Luis Castañer, and Tom Markvart, editors, *Solar Cells (Second Edition)*, pages 385 – 441. Elsevier, second edition edition, 2013.
- [141] A. Bousselham, F. H. Alharbi, and N. Tabet. Computational analysis of temperature effects on solar cell efficiency. *J. Comp. Electronics*, 16:776–786, 2017.
- [142] L. Zhu, A. P. Raman, and S. Fan. Radiative cooling of solar absorbers using a visibly transparent photonic crystal thermal blackbody. *Proc. Natl. Acad. Sci.*, 112:12282–12287, 2015.
- [143] J. P. Bergfield, M. A. Ratner, C. A. Stafford, and M. Di Ventra. Tunable quantum temperature oscillations in graphene nanostructures. *Phys. Rev. B*, page 125407, 2015.
- [144] J. Dutta, S. Mandal, S. Adhikari, P. Spiering, J. Meyer, and M. F. Somers. Effect of surface temperature on quantum dynamics of h₂ on cu(111) using a chemically accurate potential energy surface. *J. Chem. Phys.*, page 104103, 2021.
- [145] L. Hernández de la Peña and P. G. Kusalik. Temperature dependence of quantum effects in liquid water. *J. Am. Chem. Soc.*, pages 5246–5251, 2005.
- [146] U. Jovanovic, I. Jovanovic, and D. Mancic. Overview of temperature sensors

Bibliography

- for temperature measurement of pv modules. Institute of Electrical and Electronics Engineers Inc., 2018.
- [147] J. Galbán, I. Sanz-Vicente, E. Ortega, M. del Barrio, and S. de Marcos. Reagentless fluorescent biosensors based on proteins for continuous monitoring systems. *Anal. Bioanal. Chem.*, 402:3039–3054, 2012.
- [148] D. Picconi and I. Burghardt. Open system dynamics using gaussian-based multiconfigurational time-dependent hartree wavefunctions: Application to environment-modulated tunneling. *J. Chem. Phys.*, 150:224106–15, 2019.
- [149] A. Raab and H.-D. Meyer. A numerical study on the performance of the multiconfiguration time-dependent Hartree method for density operators. *J. Chem. Phys.*, 112:10718–10729, 2000.
- [150] I. Polyak, C. S. M. Allan, and G. A. Worth. A complete description of tunnelling using direct quantum dynamics simulation: Salicylaldimine proton transfer. *J. Chem. Phys.*, 143:84121, 2015.
- [151] R. Kosloff and H. Tal-Ezer. A direct relaxation method for calculating eigenfunctions and eigenvalues of the Schrödinger equation on a grid. *Chem. Phys. Lett.*, 127:223–230, 1986.